SPECTROSCOPIC INVESTIGATIONS OF ELECTRON TRANSFER PROCESSES AT SEMICONDUCTOR INTERFACES

Robin R. Knauf

A dissertation submitted to the faculty of the University of North Carolina at Chapel Hill in partial fulfillment of the requirements for the degree of Doctor of Philosophy in the Department of Chemistry.

Chapel Hill
2016

Approved by:

John Papanikolas

Jillian Dempsey

Andrew Moran

Gerald Meyer

Cynthia Schauer

ABSTRACT

Robin R. Knauf: Spectroscopic Investigations of Electron Transfer Processes at Semiconductor Interfaces
(Under the direction of Jillian L. Dempsey)

Clean and renewable energy sources are essential to meet the worlds growing energy demands. Consequently, there has been a large scientific focus on designing inexpensive and efficient solar energy devices. Dye-sensitized solar cells, which couple light absorbing molecules to low cost metal oxides, show promise as cost effective alternatives to traditional silicon solar cells; furthermore, dye-sensitized photoelectrosynthesis cells provide a means for storing solar energy in the form of chemical bonds. The rates of the electron transfer process that occur in these devices ultimately dictate their efficiencies. Understanding the factors that govern these electron transfer processes will guide rational device design. This dissertation aims to answer the following questions: What are the mechanisms by which these interfacial electron transfer processes occur, and does the rate or mechanism change with metal oxide used? Can new emerging materials, specifically semiconductor quantum dots, be incorporated as efficient chromophores in these devices?

By comparing the electron transfer rates in SnO_2-chromophore and TiO_2-chromophore systems, it was determined that the rates of back electron transfer in these systems are influenced by the identity of localized trap states within the metal oxide, how these states are populated, and the specific pathways by which back electron transfer can proceed. Recombination mechanisms were also examined for SnO_2/TiO_2 core shell systems,

as these architectures have shown increased performance in solar energy devices. It was determined that electron recombination in these systems occurs via two mechanisms, tunneling and direct recombination from localized shell trap states. The contribution from each mechanism is dependent on the TiO_2 shell thickness.

Semiconductor quantum dots were also investigated as possible chromophores for solar energy devices. Common methods of incorporating quantum dots into device architectures require exchanging native ligands for functionalized ligands that couple the quantum dots to the desired substrate. However the mechanisms of these ligand exchange processes are not well understood. These ligand exchange reactions were studied using NMR, absorbance, and photoluminescence spectroscopies. Carboxylic acid exchanges were found to occur in equilibrium, with a K_{eq}=0.83. Phosphonic acid and thiol ligand exchanges were found to be irreversible, and alter the inorganic core of the quantum dots.

ACKNOWLEDGEMENTS

There have been many people who have helped me and encouraged me throughout my life, and without them I wouldn't be where I am today. First I would like to thank my mom, Marcia Knauf. Thank you for all of your unconditional love and support in all of my life's endeavors. You have sacrificed so much so that I could have so many opportunities while growing up, and I don't think I could every thank you enough for everything you've done. I would also like to thank my sister, Kersten Simon. We have been through a lot together, and you have always been an amazing role model and support system for me.

Next I must thank my Advisor, Dr. Jillian Dempsey. She is one of the most intelligent, dedicated, and compassionate scientists I know. Thank you for all the mentorship you have provided me, I would not be the scientist I am without your guidance. I have learned so much from you over the past 5 years, and it has been a true pleasure to be a part of your lab. I could not have made it throughout my graduate studies without your encouragement, enthusiasm, and insight.

I owe much gratitude to the other members of the Dempsey group. I had the pleasure of helping build up the lab with Thomas Eisenhart, Eric Rountree, and Brian McCarthy. You have all taught me a lot about not only about science, but also sports, politics, and life in general. Thank you to Dan, Noemie, Chris, and Katherine for being great lab mates to work with. Also thank you to Kate Pitman and Matt Kita in the Miller lab for your insightful discussions about life and inorganic chemistry.

I must also thank the many scientists who provided mentorship and collaboration within the Energy Frontier Research Center. Thank you to Dr. Kyle Brennaman who helped teach me transient absorption spectroscopy, and was always willing to help me with my research. Thank you to Professors Jerry Meyer, Thomas Meyer, John Papanikolas, and Andrew Moran for not only serving on serving on my graduate committee, but also for listening to all my EFRC presentations, and providing insightful feedback on my research. Your mentorship has been invaluable.

I want to thank all of the amazing friends that I have made during my time at UNC. To Sarah, Joe, Mark, Jack, Marci, and David, thank you for helping me keep my sanity during graduate school and for helping me grow as a person,

Finally, I would like to thank my fiancé, Dr. Keegan Kelly. I cannot imagine how I would have made it through the last 4 years without you. Thank you for reminding me to take things one step at a time when I am stressed out. Thank you for taking care of BP when I was working late in lab. Thank you for pushing me to accomplish thing I never thought I could. Thank you for believing in me when I didn't believe in myself. Thank you for making me slow down, and enjoy our years in graduate school. Most of all, thank you for your unconditional love and support.

TABLE OF CONTENTS

LIST OF TABLES

LIST OF FIGURES

LIST OF ABBREVIATIONS AND SYMBOLS

E_{00}	0-0 energy gap
bpy	2,2′-bipyridine
Abs	Absorbance
Å	Angstrom
ALD	Atomic layer deposition
BET	Back electron transfer
k_B	Boltzmann constant
CdSe	Cadmium selenide
C	Celsius
cm	Centimeter
ΔH	Change in enthalpy
ΔS	Change in entropy
CCD	Charge-coupled device
δ	Chemical shift
CB	Conduction band
E_{CB}	Conduction band energy
CV	Cyclic voltammogram
DOS	Density of states
DCM	Dichloromethane
DOSY	Diffusion-ordered NMR spectroscopy
-ΔG°	Diving force
DDT	Dodecanethiol

r	Donor-acceptor distance
DSPEC	Dye-sensitized photoelectrosynthesis cell
DSSC	Dye-sensitized solar cell
e^-	Electron
k_{ET}	Electron transfer rate contant
eV	Electron volts
H_{AB}	Electronic coupling
K_{eq}	Equilibrium constant
eq	Equivalent
λ_{ex}	Excitation wavelength
Fc	Ferrocene
FTO	Fluorine-doped tin oxide
$E^{\circ\prime}$	Formal potential
FWHM	Full-width at half max
ΔG	Gibbs free energy
g	Gram
$E_{1/2}$	Half wave potential
Hz	Hertz
ITO	Indium-doped tin oxide
$h\nu$	Irradiation
K	Kelvin
kV	kilovolt
τ	Lifetime

λ_{max}	Maximum absorbance wavelength
MHz	Megahertz
MO_X	Metal oxide
MLCT	Metal-to-ligand charge transfer
μm	Micrometer
μM	Micromolar
μs	Microsecond
mJ	Millijoules
mg	Milligram
mL	Milliliter
mm	Millimeter
mM	Millimolar
mmol	Millimole
mOD	Millioptical density
mV	Millivolts
M	Molar
MEG	Multi-exciton generation
NC	Nanocrystal
nm	Nanometer
ns	Nanosecond
Nd:YAG	Neodymium doped yttrium aluminum garnet
NHE	Normal hydrogen electrode
NMR	Nuclear magnetic resonance

NOESY	Nuclear Overhauser effect spectroscopy
λ_{obs}	Observation wavelength
Ω	Ohm
OA	Oleic acid
OCP	Open circuit potential
OD	Optical density
OPO	Optical parametric oscillator
ppm	Parts per million
PL	Photoluminescence
PMT	Photomulitplier tube
PS	Photosensitizer
PV	Photovoltaic
h	Planck's constant
pXRD	Powder X-ray diffraction
H^+	Proton
QD	Quantum dot
QDSSC	Quantum dot sensitized solar cell
λ	Reorganization energy
$RuCH_2P$	$[Ru(bpy)_2(4,4'\text{-}(CH_2PO_3H_2)_2bpy)]^{2+}$
RuP	$[Ru(bpy)_2(4,4'\text{-}(PO_3H_2)_2bpy)]^{2+}$
s	Second
SILAR	Successive ionic layer deposition
Γ	Surface coverage

TCO	Transparent conductive oxide
T	Temperature
TW	Terawatt
t	Time
$\tau_{1/2}$	Time for 1/2 signal decay
TA	Transient absorption
TEM	Transmission Electron Microscopy
UV-Vis	Ultraviolet-visible
UDPA	Undec-10-en-1-ylphosphonic
UDT	Undec-10-ene-1-thiol
UDA	Undec-10-enoic acid
VB	Valence band
V	Volt
W	Watt
λ	Wavelength
w/v	Weight/volume
XPS	X-ray photoelectron spectroscopy
β	Tunneling decay constant

CHAPTER 1. Introduction

1.1. Motivation for developing solar energy technologies

Coal, petroleum, and other fossil fuels are currently leading sources of electric power generation worldwide, which raises economical, environmental, and sustainability concerns.[1–3] The combustion of these fossil fuels releases carbon dioxide, a greenhouse gas that plays a role in global warming, and the acidification of ocean water.[4–7] In 2013 alone the burning of fossil fuels released 5.405×10^{12} kg of carbon dioxide into Earth's atmosphere.[1] Additionally global energy consumption rates are increasing; from 15 TW in 2005 to a projected 27.6 TW in 2050.[3] In order to meet these rising global energy demands, and prevent environmental crises like global warming, adopting renewable, carbon-neutral fuel sources is required.

The most viable solution to this energy crisis is sunlight, with 89,000 TW of energy reaching the earth from the sun annualy[3]. Solar energy devices have made great improvements in the last decades, with sunlight-electricity efficiencies of 44% being achieved for multi-junction cells.[8] Nonetheless, less that 1 percent of the United States' energy consumption comes from solar technologies.[1] This is because there are inherent obstacles of utilizing solar energy that have not yet been overcome. The suns energy is both diffuse, and intermittent, reducing its extractable energy potential.[3] In order for large-scale implementation of solar energy as a renewable energy resource, solar energy technologies must have maximum efficiencies, inexpensive production from earth abundant materials, and be coupled to an energy storage mechanism.

One solution to address the issue of energy storage is the production of solar fuels; using energy from sunlight to produce hydrogen or reduced hydrocarbons from water and carbon dioxide.[2,9,10] A proof of concept for this practice has been well established by nature, through the process of photosynthesis, where sunlight and water are converted to oxygen and sugars. However, in nature complex enzymes have evolved over millions of years to carry out photosynthesis, and the solar energy conversion efficiency of biomass is only 1%.[9,11–14] In order to mimic natural photosynthesis without the use of the complex enzymes, the fundamental processes such as light harvesting, charge separation, and water oxidation, must be isolated and understood.

Because these fuel-forming reactions in both natural and artificial systems proceed via sequential electron transfer steps, characterizing the dynamics of these electron transfer steps is an essential step to producing functional and efficient devices. Additionally, analogous electron transfer processes dictate the efficiency of currently utilized solar-to-electricity devices such as solar cells. Having a fundamental understanding of the factors that govern these electron transfer processes will allow for rational device design that will maximize the efficiencies of both solar cell and solar fuels systems.

1.2. Dye-Sensitized Solar Cells

Currently, the most common solar energy technologies are photovoltaic (PV) devices, which utilize solar energy to produce electricity. The most commercially familiar solar cells are those made from crystalline silicon. This is because the efficiency, lifetime, and production cost of these cells is the most economical compared to other solar cell technologies.[15] However, despite improvement in the efficiencies of these devices, the high

cost to produce crystalline silicon along with the calculated lifetimes of these devices makes these technologies unable to compete with the energy prices of fossil fuels.[1,16]

As a result, many new areas of research have emerged in an attempt to develop other cheaper solar energy technologies, including thin-film technologies, organic PVs, as well as dye-sensitized solar cells. While many of these technologies currently have lower efficiencies than the traditional crystalline silicon solar cells, their low production costs may be able to compensate for large-scale use.[17,18] Additionally, they have become increasingly more efficient over the past few decades, and further research to improve the efficiencies of these devices may finally allow for solar technologies to economically compete with other energy sources.[19]

Dye-sensitized solar cells (DSSCs) are of particular interest because or their low production costs and light absorption tuneability.[20–27] DSSCs are comprised of a photoelectrode, where a light-absorbing molecule is adsorbed to a mesoporous metal oxide, a counter electrode, and a liquid electrolyte, which contains a redox mediator. One advantage of DSSCs is that the light absorption and charge separation processes are separated, which allows for the independent optimization of each of these processes. Different photosensitizers can be employed to absorb the maximum amount of solar radiation, while the semiconductor metal oxide can be altered to optimize the charge separation and extraction.

The most common type of DSSCs are n-type DSSCs, which consist of a photoanode and a dark cathode. A schematic representation of an n-type DSSC is shown in Figure 1.1. In these devices, light absorption by the photosensitizer (PS) is followed by excited-state electron injection into the acceptor states of the semiconductor. Once the electron is residing in the semiconductor, it can either transport through the material to the transparent

conductive oxide (TCO) back contact, or undergo detrimental back electron transfer (BET). Ideally the rate of electron transport through the semiconductor should be faster than the rate of back electron transfer to maximize the efficiency of the device. The electrons that are successfully transported to the TCO back contact flow to the counter electrode. This flow of electrons is what produces the electrical current that can be used in from these devices. Once at the counter electrode, the electrons reduce the electron mediator that is present in the electrolyte solution. This reduced mediator can diffuse in solution and reduce the oxidized photosensitizer, completing the circuit for the device. It is worth noting the BET can also occur between the electron in the conduction band of the semiconductor and the oxidized form of the redox mediator, creating another pathway for deactivation.

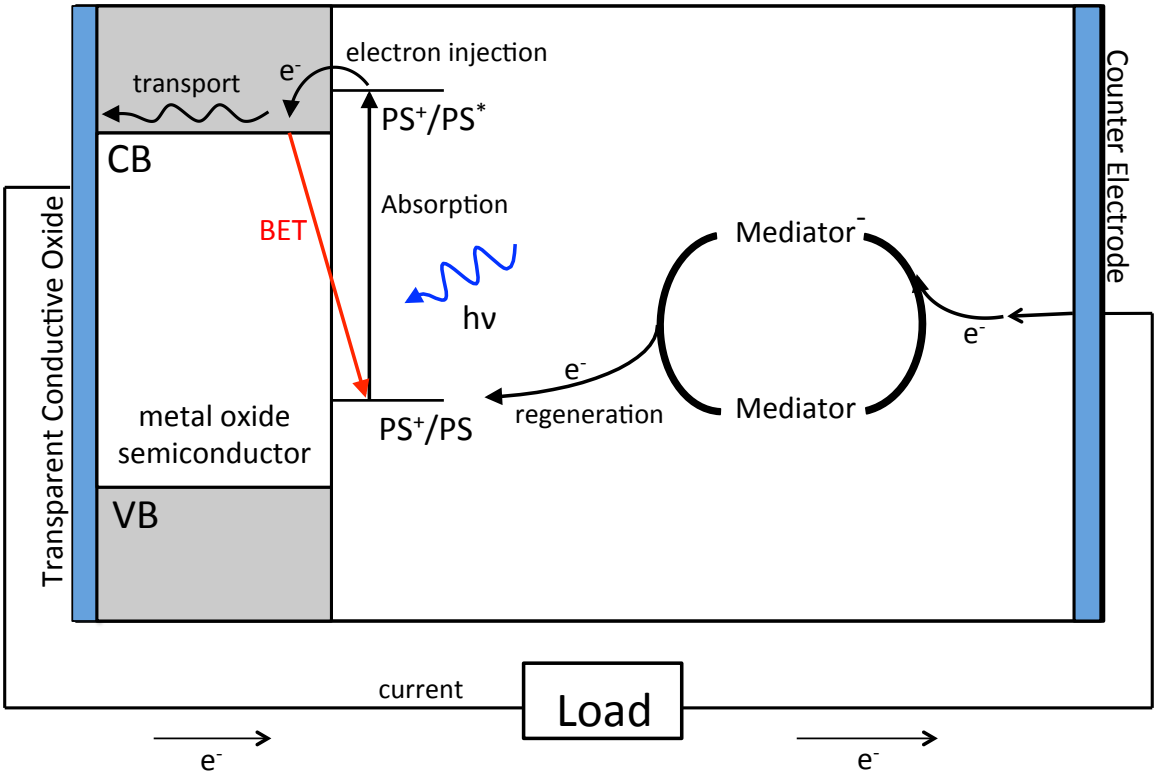

Figure 1.1 Simplified schematic representation of an n-type DSSC. PS is a generic photosensitizer.

Traditionally, DSSCs have used ruthenium-based photosensitizers for light absorption, which raises problems in terms of cost efficiency, stability, and tunability. Ruthenium-based photosensitizers are expensive, prone to degradation after multiple oxidation/reduction cycles, and have limited visible absorption tunability. As such, part of DSSC research has focused on developing robust, inexpensive photosensitizers with absorption profiles that span the entire solar spectrum. Alternative photosensitizers that have gained popularity include organic dyes, such as porphyrins,[28–32] as well as semiconductor quantum dots.[22,33–36] Quantum dots (QDs) have gained a lot of popularity as photosensitizers in DSSCs because they are inexpensive, easy to synthesize, and are robust towards oxidation and reduction.[33,34,37,38] Additionally, they have very high extinction coefficients (up to 10^6 $M^{-1}cm^{-1}$), size dependent absorption profiles, and the potential to produce multiple electron equivalents with a single photon, known as multi-exciton generation (MEG).[33,39–43]

Quantum dot sensitized solar cells (QDSSCs) operate in a similar fashion to DSSC, but one of the challenges is finding compatible electrolyte mediators for these systems. Mediators that show high performance in DSSCs, such as I^-/I_3^-, cannot be used with semiconductor quantum dots because of their corrosive nature. Therefore, sulfide/polysulfide electrolytes are generally used in conjunction with Cu_2S-based counter electrodes.[33,44] Another difference challenge for QDSSCs is incorporating QD sensitizers with strong coupling to the metal oxide for efficient electron injection. In DSSCs that use molecular photosensitizers, the photosensitizer is usually modified to contain a surface anchoring group that can covalently bind to the metal oxide surface.[10,28,31,45–48] This allows for monolayer coverage of the photosensitizer on the mesoporous metal oxide film. However using QDs as

a photosensitizer poses a unique challenge, as functionalizing these nanocrystals can be challenging.

In order to sensitize metal oxide films with QDs, physisorption of QDs onto TiO_2 film is commonly employed, but native ligands act as insulating barriers for charge transfer, impacting efficiencies of devices.[33,34] Another route that has been pursued for incorporating QD sensitizers into QDSSCs is direct growth of QDs onto the TiO_2 substrates through successive ionic layer adsorption and reaction (SILAR).[36,49] While this SILAR method exhibits higher loading of the QD layer than direct adsorption of presynthesized QDS, the chemical identity of these nanostructures is not well understood. Additionally the increased coupling in these systems leads to faster recombination rates, requiring blocking layers to be introduced to increase efficiencies.[49]

Other efforts have been made to incorporation QD synthesized via tradiation solution-based syntheses. As synthesized, these colloidal QDs are composed of an inorganic nanocrystalline core, and an aliphatic organic ligand shell which stabilizes the QDs in organic solvents. In order to incorporate colloidal QDs into many of their applications, including DSSCs, this ligand framework must be modified. Thus, procedures have been developed to exchange these for other coordinating ligands that may vary in the surface anchoring group and ligand identity. [34,35,50–70] For example, bifunctional ligands containing thiol and carboxylic acid functionalities are commonly used to anchor QDs to metal oxide surfaces.[71–77] First the metal oxide is exposed to the bifunctional ligand and the carboxylic acid moiety preferentially binds to the metal oxide surface. Then, QDs are introduced and the thiol moiety replaces native QD ligands, anchoring the QDs to the metal oxide. Alky chains are most commonly used, but phenyl bridges have also been examined to help mediate

charge transfer between the QD and metal oxide.[76] In another study a dye molecule, squaraine, acted as both a linker molecule and an electron relay. The dye was modified with carboxylic and thiol moieties and metal oxide-QD linkage was performed as described above. In this system the QD absorbs light and undergoes energy transfer with the dye, which then injects an electron into the TiO_2.[78]

Although these ligand exchange processes are commonly employed, the mechanisms and principles that govern these reactions are not explicitly understood.[79] Furthermore, the extent of these ligand exchange reactions must be controlled if a selective functionalization of the nanocrystal is desired. **Chapter 2** of this dissertation will examine these ligand exchange reactions in detail, and explore the factors than govern these processes.

1.3. Dye-Sensitized Photoelectrosynthesis Cells

As mentioned above, one of the major shortcomings of current solar energy technologies is the lack of energy storage capability. As such, research efforts in the production of solar fuels has emerged.[2,9,10] Dye-sensitized photoelectrosythesis cells (DSPECs) have been proposed as one approach for solar fuel production, which builds off the successful design of the DSSC.[10,80–85] First a light-harvesting molecule is anchored to a low cost metal oxide, then, upon light absorption, the molecule is able to transfer an electron to the semiconductor metal oxide. In a DSSC these electrons flow to a counter electrode, providing a current that can be used to drive a load, however the goal of a DSPEC is to harvest this energy and store it in the form of chemical bonds. A schematic for a DSPEC is shown in Figure 1.2.

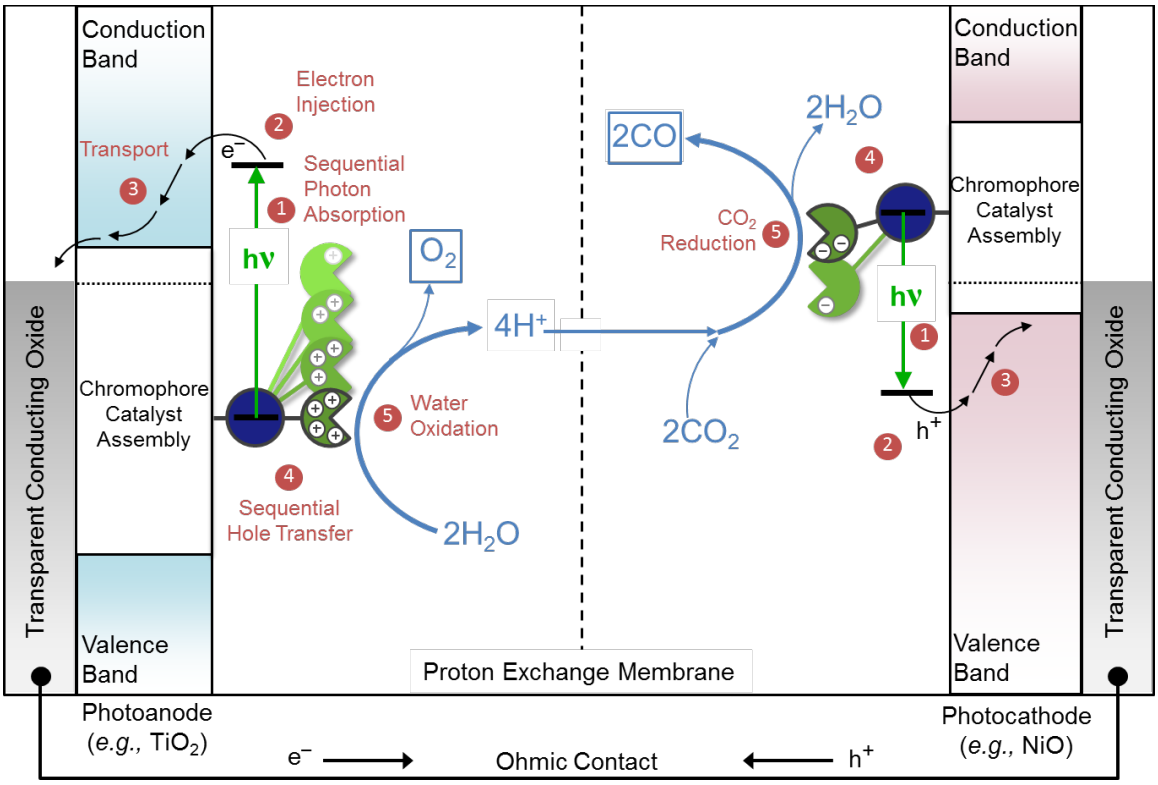

Figure 1.2. Schematic of a DSPEC for water oxidation and CO_2 reduction. (Figure credit John M. Papanikolas and James F. Cahoon)

In a tandem DSPEC, as shown above, both electrodes function as photoelectrodes. On the photoanode side of the device, a photosensitizer absorbs light and injects an electron into the conduction band of an n-type semiconductor metal oxide. On the photocathode side, a separate photosensitizer absorbs light and injects an electron vacancy, or hole, into the valence band of a p-type metal oxide. The electrons and holes that remain after these light absorption and injection process occur are transferred to molecular catalysts to do two complementary processes, water oxidation (oxygen generation) and carbon dioxide or proton reduction. At the photoanode, 4 hole equivalents are used by a catalyst to oxidize water into protons (H^+) and oxygen (O_2). At the photocathode, the electron equivalents are used by a different catalyst to either reduce CO_2 to reduced carbon containing products or to reduce

protons to hydrogen gas. Although this device architecture is proposed often in the literature, there have been limited reports of successful DSPECS, where devices suffer from low efficiencies, limited stabilities, and require a bias, or a small energy input to function.[84,86–90]

There are many challenges associated with producing a functional and efficient DSPEC. To enable water splitting, four oxidizing equivalents must be transferred from the photosensitizer to the water oxidation catalyst. These four equivalents need to be driven by four sequential single-photon excitations and injection processes. This is often limited as electrons in the metal oxide can recombine with the oxidized chromophore or the oxidized catalyst without going through the catalytic cycle, wasting the photon that generated the charge separated state. This back electron transfer process regenerates the original (and inactive) state of the assembly. Similar detrimental recombination events occur on the photocathode side of the device as well. Understanding the mechanisms by which photon-wasting charge recombination occurs will help in optimizing materials and conditions for efficient DSPECs.

Some research in the DSPEC field involves indiscriminately altering device parameters in hopes to maximize efficiency. However, fundamental studies to characterize the electron transfer processes that occur in these devices are necessary to guide rational device design. **Chapters 3, 4**, and **5** of this dissertation focus on studying the mechanisms of interfacial charge recombination processes that occur in these solar energy devices.

1.4. Charge Recombination Mechanisms in Semiconductor-Chromophore Systems

There have been extensive research efforts in characterizing and understanding charge recombination dynamics at semiconductor-chromophore interfaces. TiO_2 is one of the most commonly studied semiconductors due to its low production costs, and its semitransparent

properties as a thin film. Ruthenium polypyridyl complexes are also commonly studied chromophores due to their strong absorption in the visible region of light, in addition to their potent excited-state reduction potentials which provide a free energy gradient between their excited states and the conduction band of TiO_2, promoting efficient charge injection.[21,45,46,91]

If electron transfer in these systems follows Marcus theory for electron transfer, the rate will be dictated by various parameters including the driving force ($-\Delta G°$), reorganization energy (λ), and the electronic coupling of the donor and acceptor (H_{AB}). The impact each of these parameters has on the rate of electron transfer is depicted in the Marcus equation (Equation 1.1).[92]

The driving force is the difference in energy between the excited state oxidation potential of the chromophore and the acceptor states of the metal oxide. This can be altered by changing the chemical composition of the system (changing the chromophore or metal oxide used), but also by altering the environment. For example, changing the pH of the surrounding environment causes the acceptor states of metal oxides to more positive potentials with decreasing pH.[93] By changing chemical composition and environment in a systematic manner we can characterize interfacial electron transfer within the framework of Marcus theory or determine if other factors govern this electron transfer process.

There have been conflicting results for studies conducted examining the effects of driving force on the rate of back electron transfer in ruthenium-metal oxide assemblies. G. J. Meyer and coworkers have shown back electron transfer to be independent of driving force.[94,95] A

$$k_{ET} = \sqrt{\frac{4\pi^3}{h^2 \lambda k_B T}}\, H_{AB}^2 \exp\left\{-\frac{(\Delta G^\circ + \lambda)^2}{4\lambda k_B T}\right\} \qquad (1.1)$$

variety of rhenium, osmium, and ruthenium complexes were attached to TiO_2 and the same rate for back electron was observed fitting the data to a sum of second order kinetic processes, despite a 960 mV difference in the driving forces. Additionally the rate of back electron transfer is also unaffected by the identity of the metal (rhenium, ruthenium, or osmium) and the number of carboxylic acid groups. This is further supported by a study from Durrant and coworkers where similar recombination rates from TiO_2 we observed for both porphyrin and ruthenium based sensitizers.[32] This suggests that the observed recombination is rate limited by the electron trapping and detrapping processes that occur in the TiO_2. This trapping/detrapping mechanism for BET is consistent with additional studies that show that recombination in these systems is very sensitive to applied potentials to the TiO_2 electrode.[81,96–100]

On the contrary, others have shown back electron transfer in these systems is consistent with Marcus inverted behavior, that is, slower BET rates are observed when the driving force is increased.[97,101] Lewis et al. have reported Marcus inverted region back electron transfer for a series of ruthenium and osmium dyes linked to the surface of TiO_2. They have shown that as the driving force increases 660 mV, the rate of back electron transfer decreases by a factor of 300.[97] Hupp and coworkers have also reported Marcus inverted regime behavior for ruthenium tris(polypyridine) complexes electrostatically bound to the surface of colloidal SnO_2 in aqueous solutions.[101]

Another study has shown that these recombination kinetics are invariant of driving force, but do depend on separation between the metal oxide and the chromophore.[102] Here they state that the recombination from TiO_2 to ruthenium chromophores lies in an intermediate regime between electron transport-limited and interfacial electron transfer limited. An

elegant study by Brigham and Meyer expands on this and shows that when the number of electrons residing in the TiO_2 is small (under positive bias), diffusion/trap limited recombination ensues. However, when the density of electrons in the TiO_2 is large (under negative bas), interfacial electron transfer is rate limiting.[103]

These apparent inconsistencies in the literature may be due to differences in kinetic modeling methods as well as the inherent heterogeneity of metal oxide semiconductors. Meyer noted in his studies that recombination kinetics were more sensitive to the materials processing conditions and sample history than to the identity of the sensitizer.[94] Additionally, Lewis stated that differences in the kinetics of sensitized semiconductor systems may, in part, result from the different modes of coupling to the metal oxide that arise from the variety of sensitizers used, as well as from differences in the trap density and surface properties of the TiO_2 that is used for various studies.[97]

In an aim to rectify these discrepancies and understand these BET dynamics in aqueous conditions, **Chapter 3** of this dissertation will discuss studies that were conducted comparing electron recombination dynamics for metal oxide-chromophore systems using both TiO_2 and SnO_2. The difference in acceptor state potentials for these two semiconductors allows the influence of driving force on back electron transfer to be examined. In addition, varying other Marcus parameters, such as electronic coupling, allows the principles that govern charge recombination in these systems to be tested. Here, back electron transfer rates for both of the semiconductor-chromophore systems used are correlated with the distribution, identity, and occupation of localized trap states within the nanocrystalline metal oxide films. Recombination is influenced by the identity of metal oxide localized trap states populated and the specific pathways by which BET can proceed.

1.5. SnO_2 as a Photoanode Alternative to TiO_2

In the context of a DSPEC, SnO_2 is of interest as an alternative photoanode material to TiO_2. This is because the charge carrier mobility of SnO_2 is 2-3 orders of magnitude greater than TiO_2, allowing for faster charge extraction upon excited-state injection into the semiconductor.[104–106] Additionally, the conduction band potential of SnO_2 is 0.4 V positive of TiO_2,[83,107,108] making SnO_2 compatible with chromophores that are weaker excited state reductants and, in turn, stronger ground state oxidants capable of driving water oxidation catalysis.[28,29] However there have been numerous studies of the electron transfer dynamics of chromophore-catalyst systems on TiO_2, but very few on SnO_2.[109–114] **Chaper 4** of this dissertation examines the interfacial electron transfer processes of porphyrin chromophores synthetically designed with an excited state oxidation potential capable of injecting an electron into SnO_2, but not TiO_2. The electron transfer dynamics of a chromophore-catalyst assembly synthesized via a layer-by-layer technique are also examined.

Although SnO_2 is a desirable photoanode material for DSPEC devices, there are some drawbacks to using SnO_2. The main drawback, as highlighted in **Chapter 3** is the faster charge recombination observed for SnO_2 than TiO_2. There has been a lot of research done developing different strategies to slow down BET.[25,30,31,47,48,115–126] One of these strategies is the use of a core/shell photoelectrode.[84,120,122,126,127] Core/shell structures, where the conduction band potential of the shell is more negative than that of the core, allow for energetically favorable electron injection into the core material, while providing a significant barrier for BET from core-localized electrons. Utilizing a SnO_2/TiO_2 core shell material as a photoanode would allow the higher carrier mobility of SnO_2 to be exploited, while slowing the rate of detrimental back electron transfer. As such, when these core/shell architectures

have been incorporated into devices increased efficiencies are observed.[47,120,124] Although increased device performance is observed, the mechanism by which this recombination occurs remains unclear. Without an understanding of how recombination occurs in these systems, optimal device parameters for variables such as shell thickness, barrier height, and annealing conditions remain unknown. **Chapter 5** of this dissertation examines the recombination dynamics for sensitized SnO_2/TiO_2 photoanodes. This study examines the effects of shell thickness and annealing on the rate of recombination in these systems. Two competing mechanisms of back electron transfer are identified in these systems; tunneling of core-localized electrons, and direct recombination with shell-localized electrons. The contributions of each of these mechanisms is determined for various TiO_2 shell thicknesses.

CHAPTER 2. Quantifying Ligand Exchange Reactions at CdSe Nanocrystal Surfaces

2.1. Introduction

Research in the field of semiconductor quantum dots has exploded since the discovery of their quantum size effects in 1983.[41] Their size tuneable optical properties have been exploited for applications ranging from photovoltaic cells to solid-state lighting.[33,128] As synthesized, colloidal QDs are composed of an inorganic semiconductor core and an organic ligand shell. These ligands, generally long chain fatty acids, aid in the growth and stabilization of the QDs, solubilize the QDs in organic solvents, and passivate undercoordinated surface atoms of the QD. However, these native ligands are not ideal for many QD applications, and can be exchanged for other coordinating ligands which may vary in the surface anchoring group, chain length, and chain identity. Ligand exchanges are commonly performed to incorporate functional groups that alter QD solubility, introduce electron transfer partners, or integrate biological receptors.[34,35,50–70] The extent of these ligand exchange reactions must be controlled if a limited number of functionalized ligands per nanocrystal is desired.

Although ligand exchange reactions are commonly employed, the mechanisms and principles that govern these processes are not explicitly understood.[79] Many studies have been conducted monitoring the surface chemistry of quantum dots using photoluminescence spectroscopy, ^{1}H nuclear magnetic resonance (NMR) spectroscopy, as well as diffusion-ordered NMR spectroscopy (DOSY), nuclear Overhauser effect spectroscopy (NOESY), and ^{31}P NMR spectroscopy.[54,56,70,129–144] Among the studies focused on oleate-capped metal

chalcogenide nanocrystals, Hens and coworkers have employed these NMR methods to examine the details of various ligand exchange reactions. Through these experiments, they determined that phosphonic acids displace oleic acid (OA) with a 1:1 stoichiometry,[132] and that the self-exchange of oleic acid/oleate at the surface of CdSe QDs involves a proton exchange.[134] In a related approach, Cammidge and Bochmann used ^{1}H NMR to qualitatively study the relative binding strengths of ligands containing carboxylic acid, phosphonic acid, and thiol surface anchoring groups.[137] Additionally, Owen and coworkers have demonstrated the use of ^{1}H NMR to quantify the amount of Z-type $M(O_2CR)_2$ displacement from metal chalcogenide nanocrystals upon addition of L-type exchange ligands.[136]

However, many of these studies are qualitative in nature, and the quantitative studies generally rely on the ^{1}H NMR signature of OA, which sheds light only on the behavior of the native ligands and leaves the behavior of the incoming exchange ligands open to interpretation. Without a handle to monitor the state of the 'exchange ligand,' there is no way to quantify the ratio in which these ligands exchange, determine whether they first occupy open surface sites before exchanging, and distinguish between a surface equilibrium versus an irreversible displacement. Additionally, the use of NMR techniques alone does not distinguish between exchange reactions that occur between ligands versus those that involve labile Z-type surface ligands containing metal atoms. In order to exploit these ligand exchange reactions for controlled nanocrystal (NC) functionalization, a more thorough understanding of the NC surface chemistry is required.

In response, we have employed carboxylic acid, phosphonic acid, and thiol-terminated ligands containing a terminal alkene group in order to quantitatively monitor ligand exchange reactions at CdSe quantum dot surfaces via ^{1}H NMR (Figure 2.1). The

vinylic protons of these ligands and the alkenyl protons of the native oleic acid ligands provide distinct NMR handles for the free and surface-bound populations of both ligands in solution. Quantification of these unique ^{1}H NMR resonances provides new and valuable information about the exchange mechanism and reversibility of common ligand exchange reactions. Further, complementary absorbance and photoluminescence experiments indicate whether surface metal atoms are disrupted in the exchange reaction.

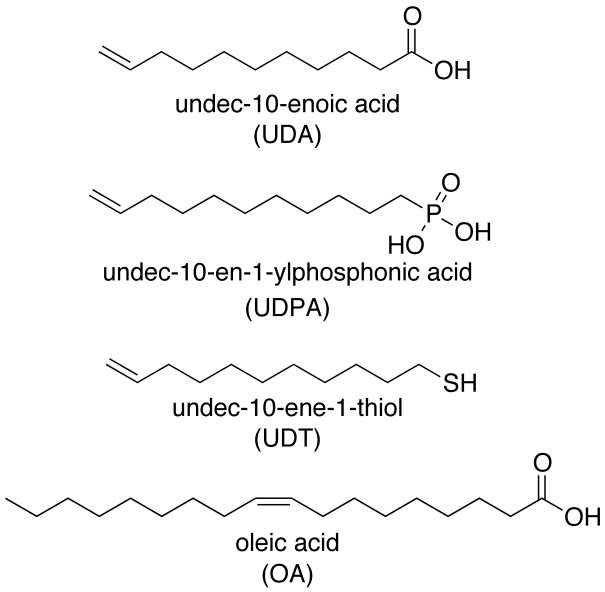

Figure 2.1: Names and structures of the ligands used in this study.

2.2. Experimental

2.2.1. General Considerations.

Standard glovebox and vacuum line techniques were utilized to maintain an inert atmosphere during synthesis of compounds and NCs, unless otherwise noted. ^{1}H and ^{31}P NMR spectra were recorded using 400, 500, or 600 MHz Bruker NMR spectrometers.[145] NMR spectra are reported at 25 °C unless otherwise stated. Chloroform-*d* and toluene-d_8 were purchased from Cambridge Isotopes Laboratories and were used without further

purification. All other reagents were commercially available and used without further purification.

2.2.2. Absorbance Measurements

Absorbance measurements were recorded using a Cary 60 UV-vis absorbance spectrophotometer.

2.2.3. Steady-State Emission.

Photoluminescence spectra were acquired with a PTI QuantaMaster 4SE-NIR emission spectrometer equipped with a housed, 75 W Xenon light source and Hamamatsu R928P PMT biased at 1100 V (1 nm step size, 2 nm bandwidth). Samples were excited at 425 nm, with a 430 nm long-pass optical filter placed before the detector. Emission intensities at each wavelength were corrected for system spectral response.

2.2.4. Time Resolved Emission.

Time-resolved emission dynamics were monitored with an Edinburgh FLS920 spectrometer, using the time-correlated single-photon counting capability (1024 channels; 1 ns per channel) with each data set collecting a set number of counts. Excitation was provided by an Edinburgh EPL-445 picosecond pulsed diode laser (444.2 nm, 80 ps FWHM) operated at 50 MHz.

2.2.5. CdSe QD Synthesis.

CdSe quantum dots were synthesized and purified following the procedure of Chambrier et al.[137] In a 50 mL 3-neck round bottom flask, 300 mg (2.33 mmol) CdO (Sigma Aldrich, ≥99.99%) was added to 2.0 mL (6.3 mmol) of oleic acid (Fisher Scientific, 90%) and 20 mL of octadecene (Sigma Aldrich, 90%). The mixture was degassed by placing the

flask under vacuum for 20 minutes. The reaction flask was then placed under N_2 and heated to 280 °C with a heating mantle until the solution became clear, indicating the *in situ* formation of $Cd(oleate)_2$. The solution was cooled to 120 °C, and 100 mg (1.27 mmol) of Se powder (Sigma Aldrich, 100 mesh, 99.5%) was added under a N_2 stream. The solution was stirred vigorously while the temperature was raised to 240 °C. The reaction solution changed from colorless to yellow to orange, indicating QD nucleation and growth. The flask was removed from the heating mantle after approximately 2 minutes, then 40 mL of toluene was added to the reaction flask to quench nanocrystal growth. The reaction solution was separated into 8 test tubes, and 5 mL of acetone was added to every 7.5 mL of reaction solution. This ratio of toluene to acetone was found to solubilize the QDs but promote the precipitation of excess $Cd(oleate)_2$. After sitting for 5 minutes, the test tubes were centrifuged to produce a white pellet and an orange supernatant. This step was found to be crucial in obtaining QDs with ^1H NMR spectra free from excess oleic acid/$Cd(oleate)_2$. The orange supernatant containing the QDs was decanted from the white $Cd(oleate)_2$ pellet. The supernatant was again distributed among test tubes, and methanol was added to achieve a 1:1 ratio of methanol to QD supernatant. Upon centrifugation the solution separated into a thick orange oil and a clear supernatant. The supernatant was discarded, and toluene was added to each test tube to redisperse the oil, then methanol was added to precipitate the QDs (1:1 toluene:methanol). After centrifugation, the supernatant was discarded, and the QDs were redispersed in DCM (7mL), and flocculated with ethanol (7mL). This DCM/ethanol purification step was repeated 5 times and a pellet was formed upon centrifugation. Lastly, acetone (~7mL) was added to the QD pellet and the tube sonicated until the pellet was dispersed. The solution was centrifuged, and the acetone decanted. This process was repeated

5 times to obtain a fine powder. This step has shown to be crucial to remove excess octadecene from the QDs, and provide a pristine NMR-quality sample.[134] The final sample was dried to yield a fine powder, and was stored as a solid. The ^{1}H NMR spectrum in toluene-d_8 is shown in Figure 2.2. The absorbance and photoluminescence spectra of the QDs in toluene are shown in Figure 2.3. The size of the quantum dots was determined from the wavelength of the E_{1S} absorption maximum as outlined by Jasieniak and coworkers.[146] The QDs used throughout this study ranged from 2.8 to 2.9 nm.

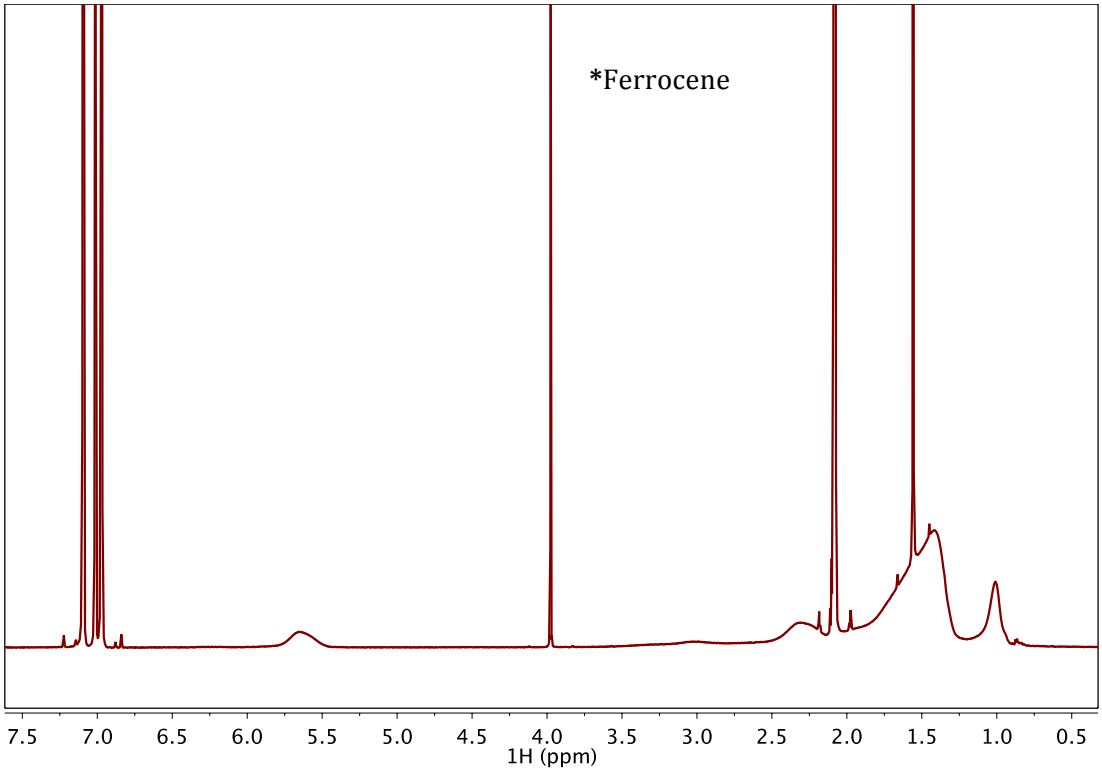

Figure 2.2: 600 MHz ^{1}H NMR spectrum of CdSe QDs in toluene-d_8. Peaks at 7.09, 7.01, 6.97, and 2.08 ppm correspond to residual toluene solvent signals. The singlet peak at 3.98 ppm corresponds to the ferrocene standard. The singlet at 1.56 ppm is due to residual water in the NMR solvent.

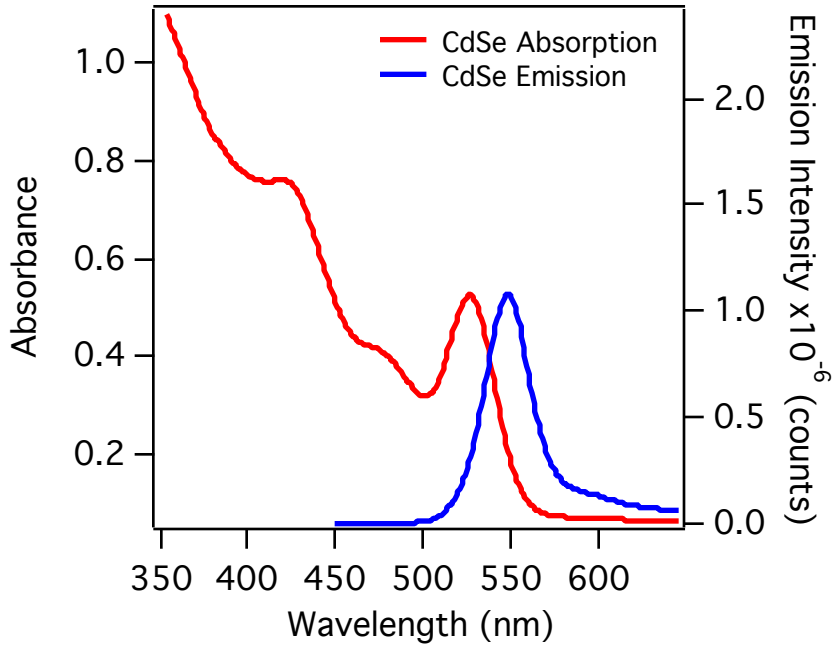

Figure 2.3: Absorbance and photoluminescence spectra of CdSe QDs in toluene after purification. Emission spectrum collected at 425 nm excitation.

2.2.6. Synthesis of undec-10-en-1-ylphosphonic acid.

Synthesis of undec-10-en-1-ylphosphonic acid was carried out via literature procedures.[147,148] In a 25 mL Schlenk flask, 2 mL (9.12 mmol) 11-bromo-1-undecene and 2 mL (11.7 mmol) triethyl phosphite were heated to reflux, neat, at 150° for 36 hours under atmosphere. The reaction was cooled and excess triethyl phosphite was removed under vacuum. Under a N_2 atmosphere, 10 mL of dichloromethane was added to the product, followed by dropwise addition of 3.47 mL (26.3 mmol) bromotrimethylsilane. The reaction was stirred overnight, after which the solvent and excess bromotrimethylsilane were removed under vacuum. 10 mL of water and 10 mL of acetone were added and the reaction was stirred for 1 hour. The solvent was removed and the product was recrystallized from hot pentane five times. 1.108 g of the pure product was obtained (52% yield). ^{1}H NMR (600 MHz,

$CDCl_3$) δ (ppm): 7.63 (2H, br s) 5.81 (1H, ddt, J=16.9 Hz, 10.2 Hz, 6.7 Hz), 4.99 (1H, dq, J=16.9 Hz, 1.8 Hz), 4.93 (1H, ddt, J=10.2 Hz, 2.3 Hz, 1.3 Hz), 2.04 (2H, ddt, J=14.8 Hz, 6.87 Hz, 1.4 Hz), 1.74 (2H, m), 1.60 (2H, m), 1.37 (2H, m), 1.27 (8H, m). ^{31}P NMR (600 MHz, $CDCl_3$) δ (ppm): 37.61.

2.2.7. Synthesis of S-(undec-10-en-1-yl) ethanethioate.

Undec-10-ene-1-thiol was synthesized via literature procedures.[149,150] 1.71 g (15 mmol) potassium thioacetate was added to 15 mL of 95% ethanol in a pear flask, sonicated until fine, and then sparged with N_2 for 20 minutes. This solution was then added to a previously sparged solution of 3.5 mL (16 mmol) 11-bromo-1-undecene in 15 mL ethanol (95%) in a Schlenk flask. The resulting solution was heated to reflux under N_2 for 19 hours. The solution turned brown over time and white precipitate slowly formed (KBr). The reaction mixture was diluted with 50 mL water and extracted with 3x50 mL pentane. The organic fractions were combined and concentrated via rotary evaporation. The resulting crude product was purified via column chromatography over silica gel using a gradient pentane to 4:1 pentane:diethyl ether eluent to give S-(undec-10-en-1-yl) ethanethioate. Yield 2.5 mL (83%). ^{1}H NMR (400 MHz, $CDCl_3$) δ (ppm): 5.81 (1H, ddt, J=17.0 Hz, 10.1 Hz, 6.7 Hz), 4.99 (1H, dq, J=17.2 Hz, 1.8 Hz), 4.92 (1H, ddt, J=10.1 Hz, 2.3 Hz, 1.2 Hz), 2.86 (2H, t, J=7.3 Hz), 2.32 (3H, s), 2.03 (2H, ddt, J=14.8 Hz, 6.87 Hz, 1.4 Hz), 1.55 (2H, qn J=7.8 Hz), 1.35 (4H, m), 1.27 (8H, m).

2.2.8. Synthesis of undec-10-ene-1-thiol.

A Schlenk flask containing 10 mL dry diethyl ether and 400 mg (10.5 mmol) $LiAlH_4$ was placed under N_2 and cooled to 0° C. 1.37 g (6.0 mmol) S-(undec-10-en-1-yl) ethanethioate was added dropwise with stirring. The solution was warmed to room

temperature and stirred for 45 minutes. The reaction was quenched with slow addition of 6 mL 1.0 M HCl. The reaction mixture was filtered through a glass frit and washed with diethyl ether. The organic layer was separated, dried with Na_2SO_4, and had solvent removed via rotary evaporation. Evaporation yielded the neat undec-10-ene-1-thiol (1.08 g, 97%) which was immediately stored in the freezer to prevent disulfide formation. ^{1}H NMR (400 MHz, $CDCl_3$) δ (ppm): 5.81 (1H, ddt, J=17.0, 10.2, 6.7 Hz), 4.99 (1 H, dq, J=17.2, 1.7 Hz), 4.93 (1H, ddt, J=10.2, 2.3, 1.2 Hz, 1H), 2.52 (2H, q, J=7.5 Hz), 2.04 (2H, ddt, J=14.8 Hz, 6.87 Hz, 1.4 Hz), 1.60 (2H, qn, J=7.3 Hz), 1.37 (m, 4H), 1.35 (1H, t, J=7.8 Hz), 1.23 (8H, m).

2.2.9. Sample Preparation for ^{1}H NMR Titrations.

Samples were prepared by first dissolving dried quantum dots in toluene-d_8 to make a stock solution. Then an aliquot was removed and diluted with toluene, and the concentration of the stock solution was determined from the absorbance spectrum using published extinction coefficients.[146] 100 μM samples of QDs were prepared in toluene-d_8 from this stock solution for ^{1}H NMR titrations. Ferrocene (0.2 μmol) was added to each NMR sample as an internal standard for determining the concentration of OA and the exchange ligands. Exchange ligands were titrated (5-20 equivalents per aliquot depending on the ligand) into the samples. After each addition, a ^{1}H NMR spectrum was recorded (600 MHz). For these measurements, 8 scans were recorded with a relaxation time (d_1) of 30 s. Spectra were referenced to the residual methyl solvent peak in the toluene-d_8 and were processed using MestraNova software. The multipeak fitting function in MestraNova was used to integrate the vinyl and alkenyl peaks in the ^{1}H NMR to determine the concentrations of bound and free OA and exchange ligand as discussed in detail below.

2.3. Results and Discussion

2.3.1. Synthesis and Purification of CdSe QDs

Zinc-blende CdSe QDs (2.8 nm diameter) capped with oleic acid were synthesized and purified following the procedure of Chambrier et al.[137] Sequential precipitations employing methanol and ethanol as antisolvents, followed by sonication in acetone were found necessary in order to obtain QD samples free from residual OA and octadecene.

To examine the evolution of the nanocrystal surface during sequential purification and precipitation steps, absorbance and photoluminescence (PL) spectra were recorded throughout the purification process (Figure 2.4, Figure 2.5). Other purification methods reported in the literature are known to lead to ligand loss and impact the PL of QDs.[136,140,144,151–156] After addition of acetone to the toluene-quenched reaction solution (3:2 toluene:acetone) to precipitate excess $Cd(oleate)_2$ starting material, no changes in the absorbance spectrum are observed. Subsequent precipitation/centrifugation steps employing methanol as an antisolvent lead to hypsochromic shifts (ca. 5 nm total) of all the absorbance features. Subsequent dispersion in dichloromethane followed by precipitation/centrifugation with ethanol leads to negligible absorbance shifts. The observed blue shift of the excitonic absorption peaks suggests a decrease in the size of the QDs, presumably due to removal of $Cd(oleate)_2$ from the QD surface. Additionally, there is a slight flattening of the $1S_e \leftarrow 2S_{h3/2}$ transition (λ = 480 nm). The absorbance changes are accompanied by quenching of the PL; the PL is quenched by 41% with the first methanol wash, though subsequent precipitation steps do not significantly affect the PL quantum yield (Figure 2.5A). By contrast, the PL lifetime is only slightly quenched during the purification process (Figure 2.5B).

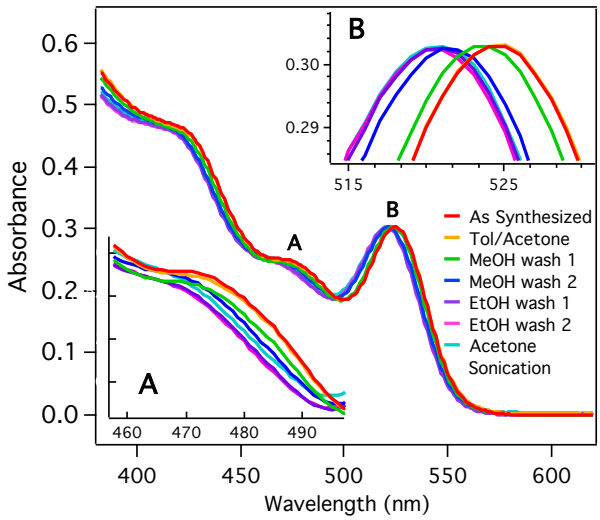

Figure 2.4: Absorbance spectrum of 2.1 μM CdSe QDs in toluene after various purification steps. Inset A: The $1S_e \leftarrow 2S_{h3/2}$ transition shows very slight flattening over the course of purification. Inset B: The 1st excitonic peak undergoes a hypsochromic shift with increased purification steps.

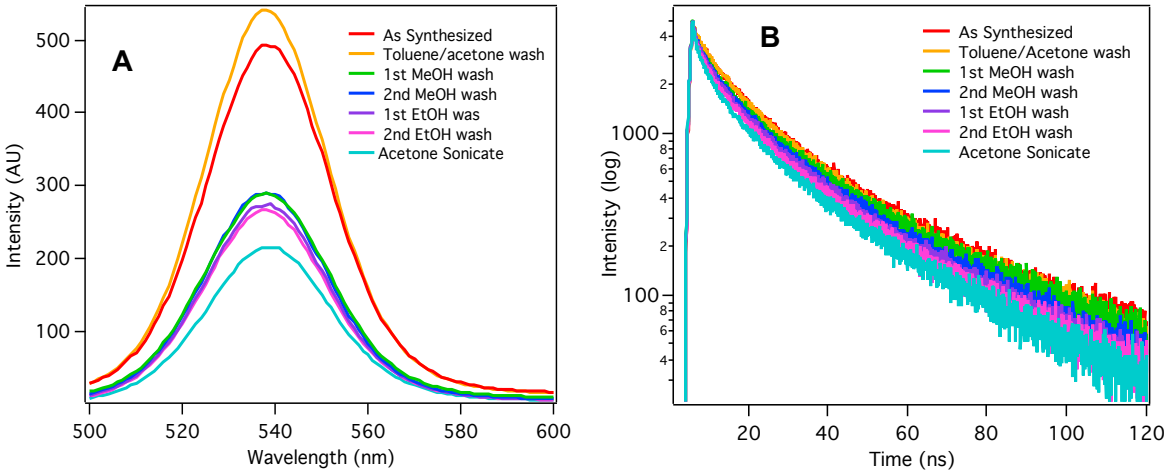

Figure 2.5: A) Steady-state photoluminescence spectrum of 2.1 μM CdSe QDs in toluene after various purification steps (425 nm excitation). **B)** Time-resolved photoluminescence spectrum of 2.1 μM CdSe QDs at 540nm in toluene after various purification steps (444 nm excitation).

These changes observed in the QD absorbance and PL are consistent with previously reported effects of purification on NC ligand density. Methanol has commonly been reported to remove surface bound ligands when used in purification.[144,151,152] Hens and coworkers have suggested that ligand loss occurs via protonation of the native carboxylic acid ligands

by methanol, followed by dissociation, whereas ligand loss is not observed for aprotic antisolvents like acetonitrile.[154] Alternatively, Owen and coworkers report that alcohols, like other L-type ligands, promote the displacement of $Cd(oleate)_2$ Z-type ligands from QD surfaces.[136] The decrease in PL quantum yield as well as the hypsochromic shift of the absorbance spectrum we observe upon purification are consistent with those observations reported for CdSe NCs in which $Cd(oleate)_2$ is intentionally displaced from the NC surface in an L-type promoted Z-type displacement reaction.[136,157] Of note, the effects of purification are likely sensitive to the NC synthesis and crystal structure.

Surface ligand densities were determined by integration of the alkenyl resonance of OA in the ^{1}H NMR spectrum versus a ferrocene standard of known concentration (Figure 2.6). Based on the concentration of QDs in solution, the QDs used in this study have 35-37 OA ligands per NC (2.8 to 2.9 nm diameter respectively), which corresponds to a surface OA ligand density of 1.4 OA/nm^2. This falls on the lower end of what has been reported previously for carboxylic acid-terminated ligands (1.8 – 4.6 OA/nm^2).[134,137] This likely arises from the displacement of the $Cd(oleate)_2$ ligand shell upon purification.[136] The surface density obtained is also sensitive to the extinction coefficient used for determining the concentration of the QDs, as determined from the absorption spectra. Extinction coefficients determined via the method of Yu et al. and Jasieniak et al. yield ligand densities of 0.9 OA/nm^2 and 1.6 OA/nm^2 respectively,[40,146] while the size independent extinction coefficients from Leatherdale et al. and Čapek et al. consistently result in calculated ligand densities of 1.4 OA/nm^2.[42,43]

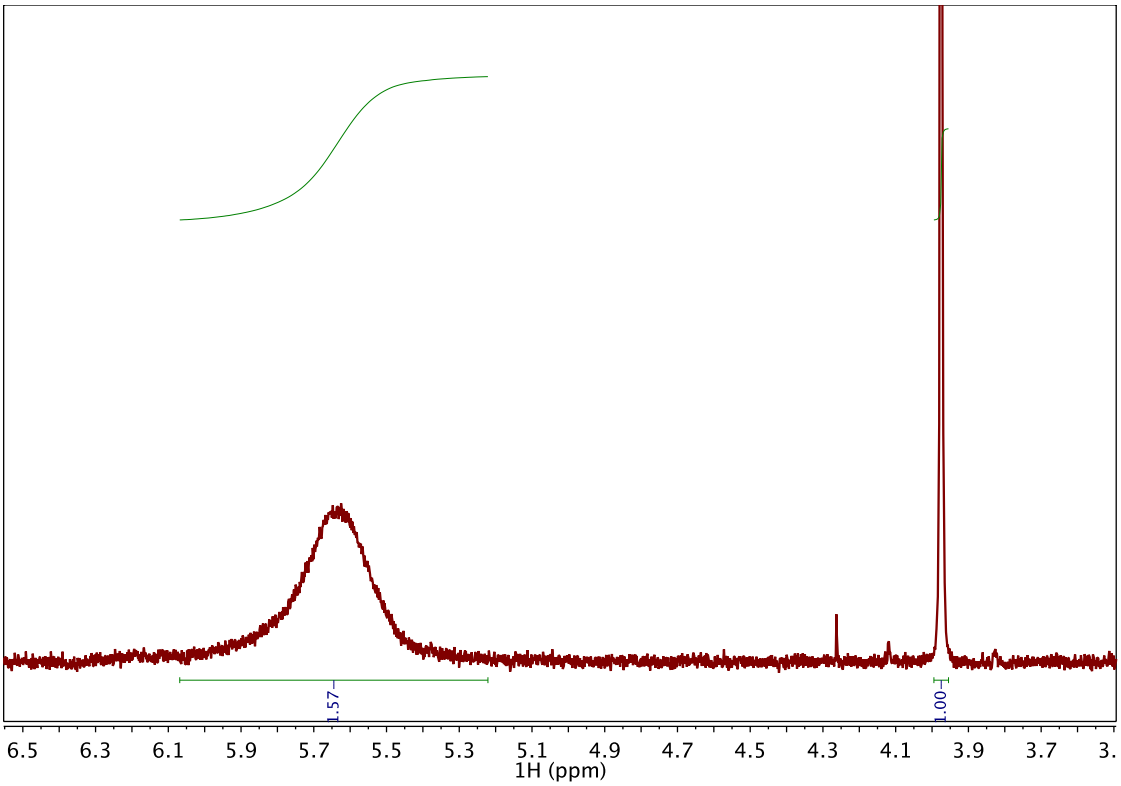

Figure 2.6: 600 MHz ^{1}H NMR spectrum of 111 µM CdSe QDs (5.64 ppm) and 493 µM ferrocene (3.97 ppm) in toluene-d_8. A ligand density of 1.4 OA/nm^2 is determined from the integrals of these peaks.

2.3.2. Quantification of Surface Ligands via ^{1}H NMR

The nanocrystals employed in this study are coordinated exclusively by oleic acid. The ^{1}H NMR spectrum of the purified QDs contains a diagnostic feature for the alkenyl protons of the oleic acid at ca. δ 5.65 ppm (Figure 2.2). Upfield regions of QD ^{1}H NMR spectra are commonly muddled as long chain ligands contain large number of aliphatic protons. In addition, signals for coordinated ligands are broadened due to inhomogeneity of the chemical environments and the restricted relaxation of the protons arising from coordination to the large nanocrystal. In comparison, the alkene region of these spectra is very clear and the alkene proton peak for oleic acid is diagnostic for determining ligand surface coordination. In chlorinated solvents like $CDCl_3$ and CD_2Cl_2 this alkenyl peak is

broad for surface-bound ligands; when the ligand is displaced from the surface, the signal sharpens and displays a clear splitting pattern, but the absence of a distinct shift upon dissociation makes deconvoluting bound and free resonances difficult.[137] However, in deuterated aromatic solvents like toluene-d_8 and benzene-d_6, the signals for bound and free oleic acid peaks can readily be resolved as they exhibit distinct chemical shifts.[134,136] In toluene-d_8 the chemical shift of the alkenyl protons on OA changes from 5.64 ppm when bound to 5.46 ppm when free. As such, this peak can be utilized as a spectroscopic handle to quantify the concentrations of bound and free oleic acid in a sample (Figure 2.6).

In order to obtain a deeper understanding of the surface chemistry of CdSe QDs, we have explored exchange reactions with a family of ligands that contain both a common X-type QD surface anchoring group (carboxylic acids, phosphonic acids, and thiols) and a terminal alkene. These ligands provide a ^{1}H NMR handle to quantify both the free and surface-bound forms of this "exchange" ligand, analogous to the OA signature. Unlike previous studies,[54,56,129–138] this approach allows both the native and exchange ligand to be quantified, enabling measurement of the surface equilibrium and ligand exchange ratios.

2.3.3. Ligand Exchange with Carboxylic Acid-terminated Ligands

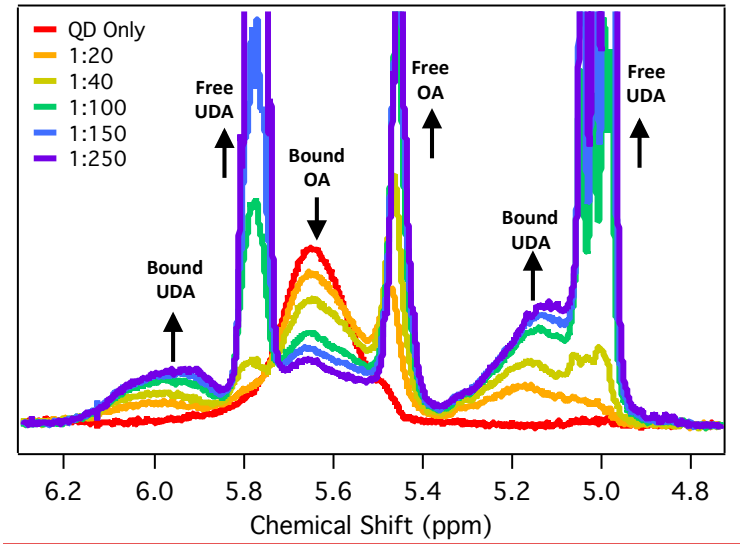

Figure 2.7: ^{1}H NMR spectrum of 100 µM CdSe QDs titrated with undec-10-enoic acid (UDA) in toluene-d_8 (600 MHz). Legend indicates the QD:UDA ratio in solution.

Upon the addition of undec-10-enoic acid (UDA) to the OA-capped CdSe NCs, both states of OA (5.64 ppm bound, 5.46 ppm free) and UDA (5.96 ppm and 5.15 ppm bound, 5.78 ppm and 5.01 ppm free) are observed in the alkenyl region of the ^{1}H NMR spectrum (Figure 2.7). Like OA, the vinylic protons of UDA have diagnostic features in the alkenyl region and the bound and free forms of this ligand can readily be distinguished by their chemical shifts, broadness and splitting patterns. As UDA is titrated into the solution, the concentration of free OA and bound UDA steadily increases, providing evidence that a surface equilibrium exists for these carboxylic acid-terminated ligands (Equation 2.1). From this equilibrium, the equilibrium constant K_{eq} can be determined (Equation 2.2).

$$QD\text{–}Oleate^{-} + XH \leftrightarrow Oleic\ Acid + QD\text{–}X^{-} \tag{2.1}$$

$$K_{eq} = \frac{[OA]_F[X^-]_B}{[Oleate^-]_B[XH]_F} \tag{2.2}$$

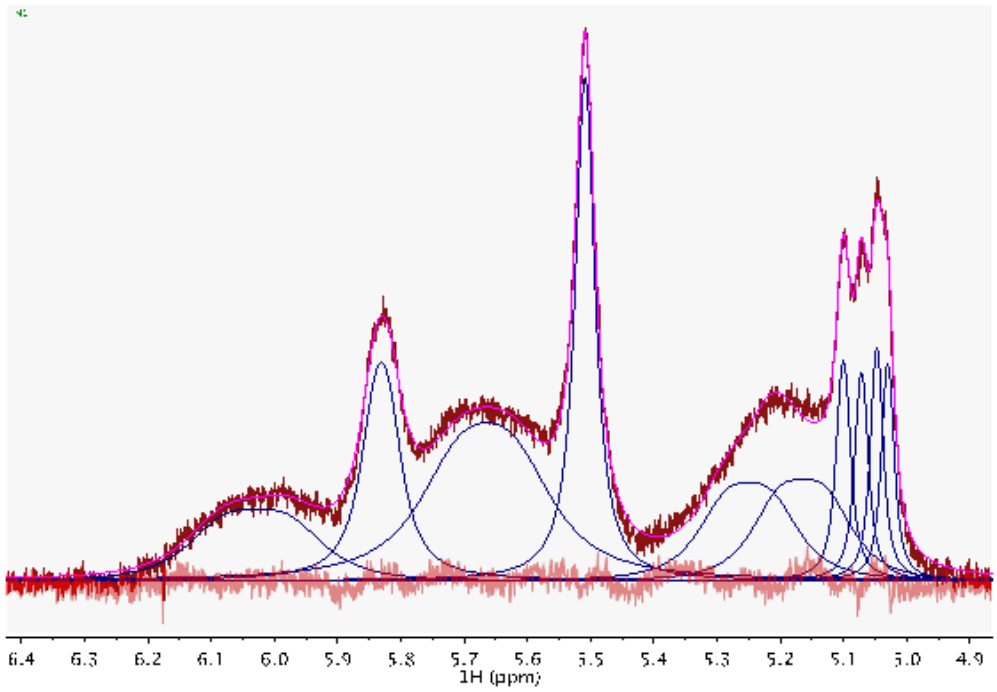

Figure 2.8: Multi-peak fitting of the 600 MHz ^{1}H NMR spectrum of CdSe QDs and UDA in toluene-d_8. The maroon trace is the sample NMR spectrum, the magenta trace is the fit, and the red trace is the fit residual.

Integration of the bound oleate ($[Oleate^{-}]_B$), free oleic acid ($[OA]_F$), bound UDA ($[X^{-}]_B$), and free UDA ($[XH]_F$) signals against a ferrocene standard allows the concentrations of these four species to be experimentally determined (Figure 2.8). Analysis of each spectrum obtained over the course of the titration yields an average K_{eq} of 0.84 (Table 2.1). The linear relationship of $[OA]_F[L^{-}]_B$ vs. $[Oleate^{-}]_B[LH]_F$ (Figure 2.9) gives a similar equilibrium constant (K_{eq} = 0.82) resulting in an average K_{eq} = 0.83. Notably, upon dilution of the endpoint sample, no changes to the relative integrations of the bound and free ligand signals are observed (Figure 2.10). Further, the ratio of $[OA]_F$ to $[UDA]_B$ is 0.98:1, indicating that UDA does not initially bind to free sites on the QD surface before displacing the native ligands (Table 2.1).

Table 2.1: K_{eq} and ligand exchange ratio obtained for different additions of UDA to a sample of CdSe QDs. The standard deviation for K_{eq} is 0.05.

[UDA] added (M)	K_{eq}	$[OA]_F$:$[UDA]_B$
0.002	0.82	1.1:1
0.003	0.89	0.87:1
0.004	0.77	1.03:1
0.006	0.78	0.92:1
0.01	0.83	0.96:1
0.012	0.88	0.92:1
0.015	0.88	1.1:1
0.025	0.89	1.02:1
Diluted to 0.008	0.86	0.89:1
OA added (0.01M)	0.80	—
Average	**0.84**	**0.98:1**

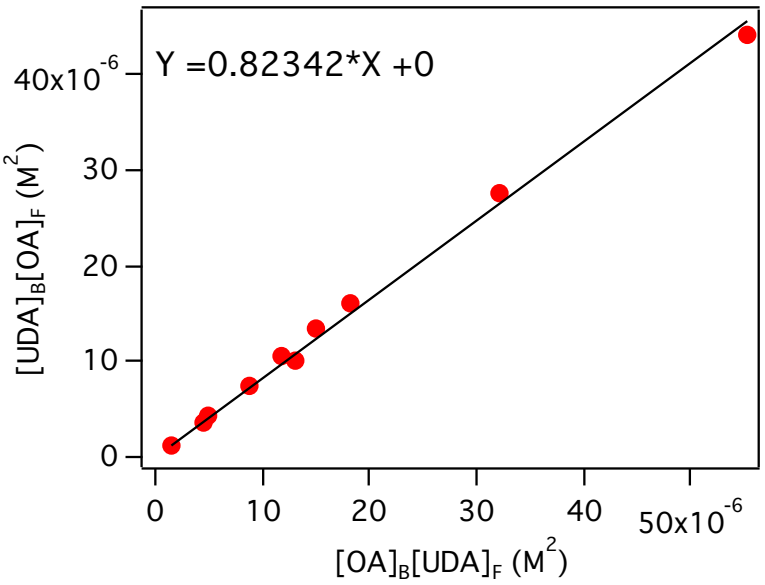

Figure 2.9: Plot of $[OA]_F[UDA]_B$ vs. $[OA]_B[UDA]_F$. The slope of this plot can be used to determine an average K_{eq} for the ligand exchange between OA and UDA.

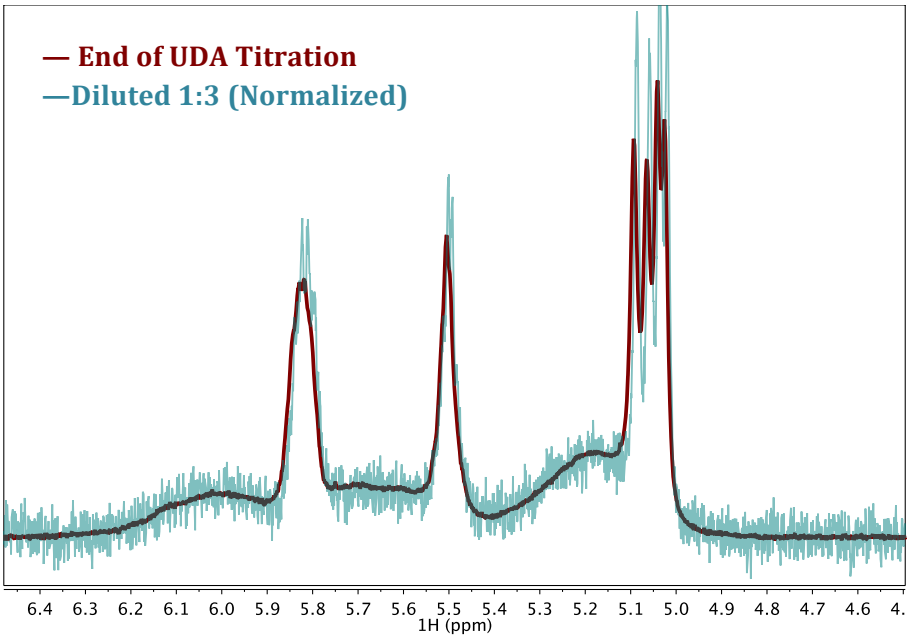

Figure 2.10: 600 MHz ^{1}H NMR spectrum of 100 μM CdSe QDs and 0.012 M UDA in toluene-d_8 before (maroon) and after (teal, normalized) dilution by a factor of 3.

Addition of OA at the endpoint of the titration leads to an increase in the bound OA signal along with a decrease in the bound UDA signal, demonstrating the reversibility of this equilibrium (K_{eq} = 0.8, Figure 2.11). We attempted to run this exchange reaction in the reverse direction, but unfortunately we were unable to cleanly isolate the UDA-capped NCs; the necessary purification steps resulted in loss of solubility in toluene. The change in solubility is likely due to the shorter chain length of UDA in comparison to OA.

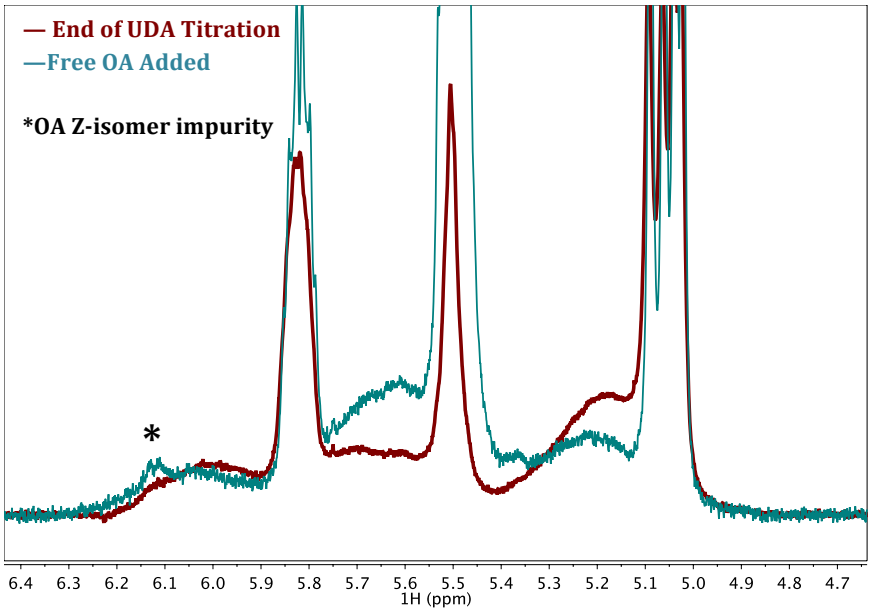

Figure 2.11: 600 MHz ^{1}H NMR spectrum of 100 μM CdSe QDs and 0.012 M UDA in toluene-d_8 before (maroon) and after (teal) the addition of 0.010 M free oleic acid. The stared peak indicates the Z-isomer of OA that is present in lab grade OA.

Absorbance and PL spectra were recorded over the course of the titration to examine if displacement of Z-type Cd(oleate)$_2$ occurs during exchange, or if the exchange process is purely X-type (Figure 2.12). Upon addition of UDA, a minute blue shift (2 nm) of the CdSe excitonic peak is observed. This could arise from the reduced solvent shielding that arises from the shorter-chain UDA ligand. Importantly, there is no change to any of the higher-order absorbance peaks, and no quenching of the steady-state PL, suggesting no displacement of Cd(oleate)$_2$ from the NC occurs.[136,157] These data suggest that exchange occurs solely between the X-type ligands, and the surface cadmium atoms remain unaltered.

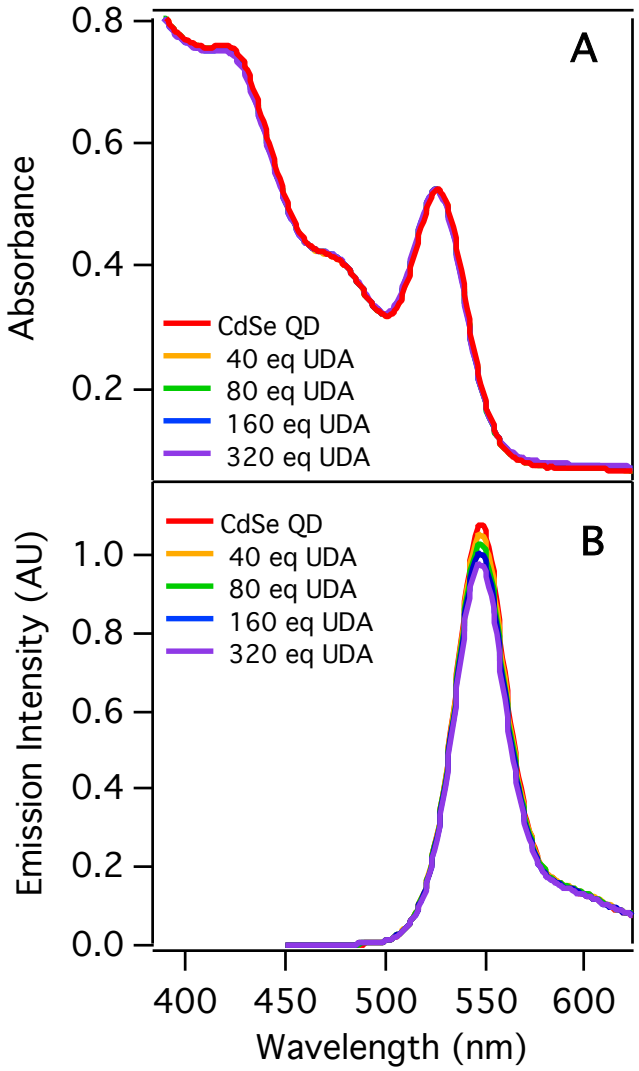

Figure 2.12: A) Absorption spectrum of 3 μM CdSe QDs in toluene titrated with UDA. **B)** Steady-state PL spectrum (425 nm excitation) of 3 μM CdSe QDs in toluene titrated with UDA.

The K_{eq} value determined for this ligand exchange reaction corresponds to a ΔG of 454 J/mol, indicating this exchange is slightly unfavourable at room temperature. To further probe the surface equilibrium between OA and UDA, variable temperature NMR studies were performed. ^{1}H NMR spectra were recorded at temperatures ranging from 313 K to 283 K for samples containing OA-capped QDs and UDA (Figure 2.13). A Van 't Hoff plot was constructed from the K_{eq} values determined across the temperature range (Figure 2.14). The

ΔH = +8.45 ± 0.1 kJ/mol determined for this X-type ligand exchange indicates that this exchange is an endothermic process. For comparison, two recent reports utilizing isothermal titration calorimetry to assess ligand adsorption thermodynamics show that the reversible binding of L-type ligands to vacant coordination sites of CdSe/CdZnS core/shell particles is an exothermic process while the exchange of X-type acetate for catechol on ZnO nanocrystals in accompanied is accompanied by a positive ΔH.[153,158] These limited data suggest that X-type exchange may generally be an endothermic process.

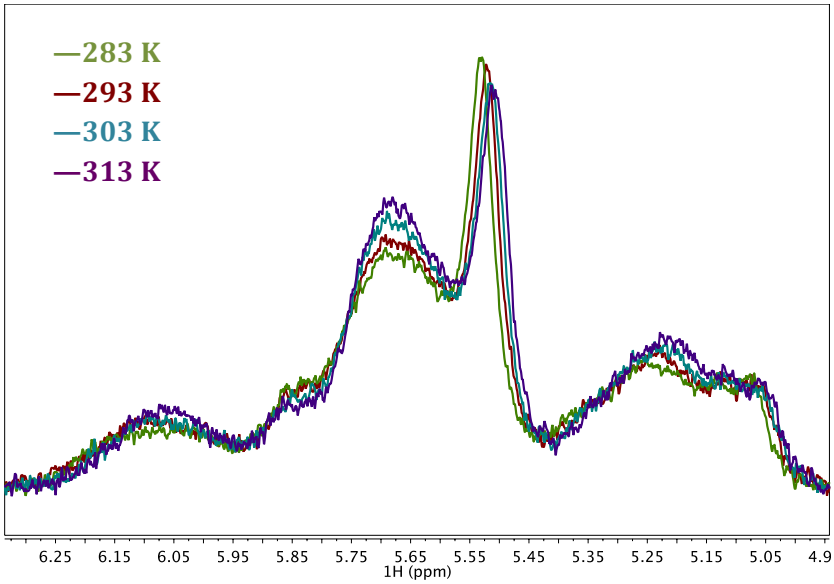

Figure 2.13: 500 MHz ^{1}H NMR spectrum of 0.0015 M UDA and 0.0001 M QD at temperatures ranging from 283 K to 313 K.

For the X-type exchange reaction explored here, a value of ΔS = +28 J/mol•K was obtained from the Van 't Hoff analysis. As the ΔS value is derived from extrapolation to an intercept, entropy values determined from Van 't Hoff analyses are often considered especially prone to error, thus just the sign of the ΔS value is commonly interpreted.[159] The positive ΔS value indicates that exchange is an entropically favourable process. While the observed increase in entropy is not obvious from the 1:1 exchange quantified through NMR studies, the aforementioned acetate–catechol exchange on ZnO nanocrystals is also

accompanied by a positive ΔS (+13.1 J/mol•K).[158] Overall, the energetic parameters obtained in these studies are consistent with previous observations of carboxylic acid ligand exchange reactions for CdSe; a large excess of exchange ligand is required, and these exchange reactions often require heating or sonication to achieve full ligand displacement.[55,79,160]

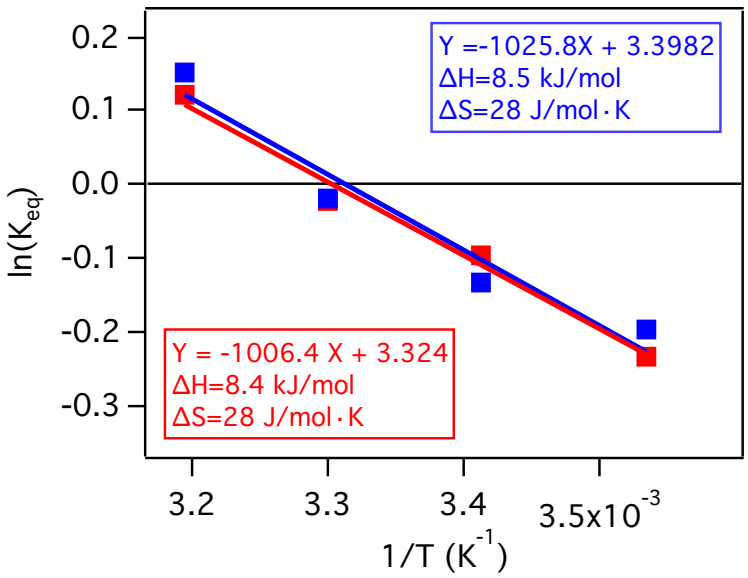

Figure 2.14: Van 't Hoff plot for the ligand exchange between native OA and UDA in toluene-d_8. Sample 1 (blue trace) contains 0.0015 M UDA and 0.0001 M QD. Sample 2 (red trace) contains 0.0030 M UDA and 0.0001 M QD.

There have been conflicting literature claims as to whether or not the acidic proton on the incoming exchange ligand is involved in the exchange reaction. Does the exchange mechanism follow a protonation of native surface oleate, followed by loss of oleic acid and binding of the exchange ligand carboxylate? Does nucleophilic attack by the exchange carboxylic acid occur? Or is a dissociative mechanism responsible for exchange? In an aim to probe the exchange pathway, we performed experiments with OA-capped CdSe QDs with UDA and 1 equivalent of N,N-diisopropylethylamine. This base was specifically chosen because the steric hindrance from the isopropyl groups allow it to interact with the acidic proton of UDA in solution, but interaction with the QD surface will be severely hindered.

Owen and coworkers have shown that a 2 M solution of a similar base, tributyl amine, only displaces 2% of native surface oleate groups.[136] At the concentrations utilized in this study (2 mM to 16 mM), the effect displacement from the N,N-diisopropylethylamine is negligible. In the NMR spectrum of UDA with 1 equivalent of N,N-diisopropylethylamine (Figure 2.15), the peaks for the protons in the alpha and beta positions to the carboxylic acid undergo significant shifts (2.1 ppm) when N,N-diisopropylethylamine is added, while the terminal alkene protons are unaffected. This indicates an interaction between the N,N-diisopropylethylamine and UDA, though full deprotonation may not occur.

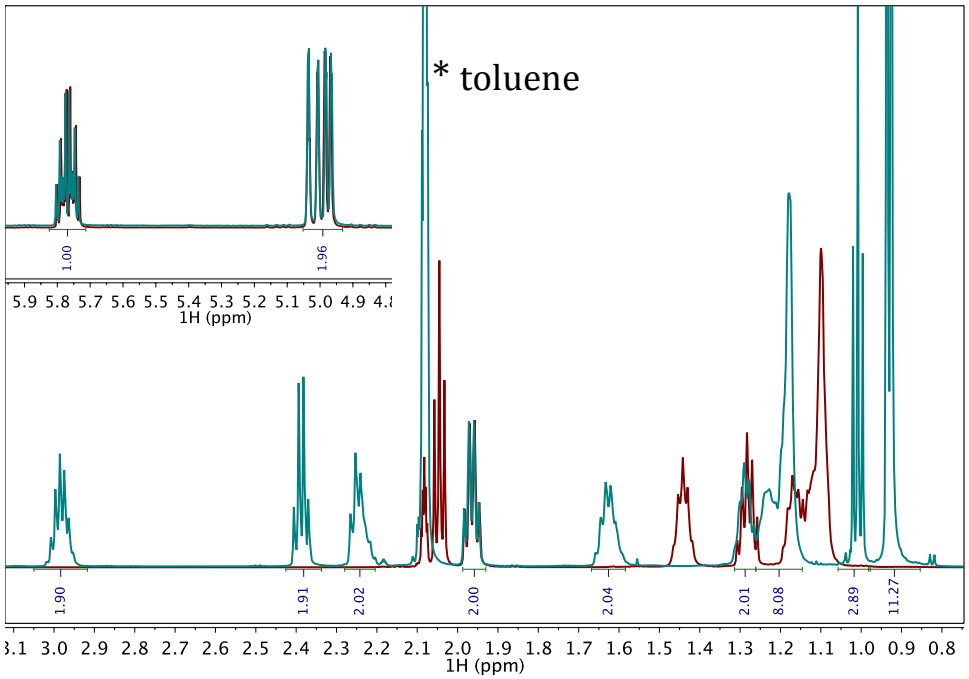

Figure 2.15: 600 MHz ^{1}H NMR spectrum of UDA before (maroon) and after (teal) the addition of 1 equivalent of N,N-diisopropylethylamine in toluene-d_8. The starred peak indicated toluene solvent signal

OA-capped CdSe QDs were titrated with 1:1 UDA:N,N-diisopropylethylamine (Figure 2.16). Upon titration, both states of OA (5.64 ppm bound, 5.46 ppm free) and UDA (5.96 ppm and 5.15 ppm bound, 5.78 ppm and 5.01 ppm free) are observed. As was done for

samples without base added, the NMR spectra at different UDA concentrations were integrated and a K_{eq} of 0.84 was determined. This value obtained for K_{eq} is the same as that obtained for protonated UDA. This suggests that a protonation of surface bound oleate by the exchange ligand may not be the mechanism for surface displacement. Even if N,N-diisopropylethylamine does not fully deprotonate UDA, and instead forms an adduct, this adduct would be less acidic than UDA, and a change in the K_{eq} would be expected. We suggest that a dissociative mechanism may be at play, but further investigation is required. A correlation between the extent of displacement or exchange K_{eq} and exchange ligand pK_a would shed additional light on the mechanism of surface exchange.

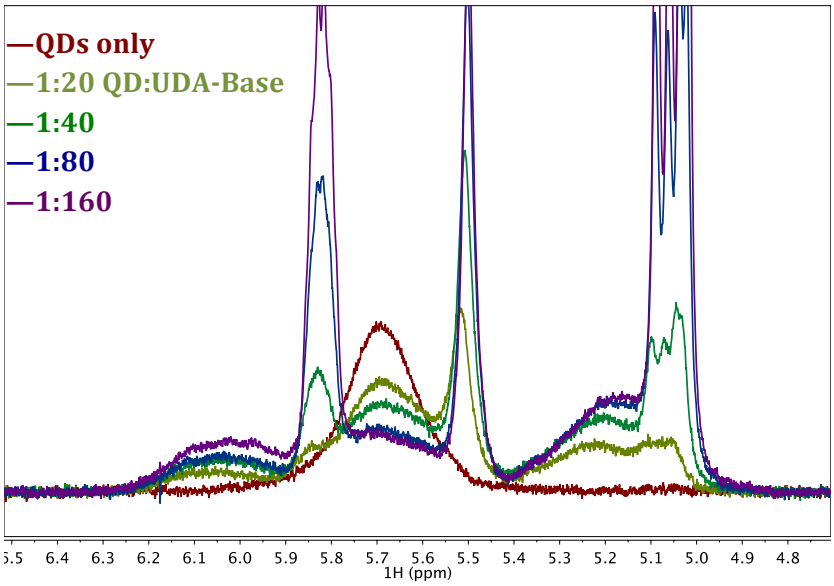

Figure 2.16: 600 MHz ^{1}H NMR spectrum of 100 μM CdSe QDs titrated with UDA–N,N-diisopropylethylamine in toluene-d_8. Legend indicates the QD:UDA ratio in solution.

2.3.4. Ligand Exchange with Phosphonic Acid-Terminated Ligands

The phosphonic acid analogue of UDA, undec-10-en-1-ylphosphonic acid (UDPA), was synthesized by a Michaelis-Arbuzov reaction of triethylphosphite with 11-bromo-1-undecene acid, followed by cleavage of the ester groups with bromotrimethylsilane. OA-

capped CdSe NCs were titrated with UDPA and monitored by ^{1}H NMR (Figure 2.17). Unlike the carboxylic acid analogues, only bound UDPA (δ 5.89 and 5.12 ppm), bound OA (δ 5.64 ppm), and free OA (δ 5.45 ppm) are observed across the addition of up to 40 equivalents of UDPA. Free UDPA (δ 5.80 and 5.02 ppm) only appears once all of the oleic acid is displaced from the surface, suggesting that this ligand exchange is not an equilibrium process, but rather involves quantitative displacement of OA by UDPA. Integration of the free OA and the bound UDPA signals yields an exchange ratio of 1.06:1 free OA:bound UDPA, indicating that UDPA does not initially bind uncoordinated atoms on the NC surface before displacing OA, consistent with work by Hens and coworkers.[132]

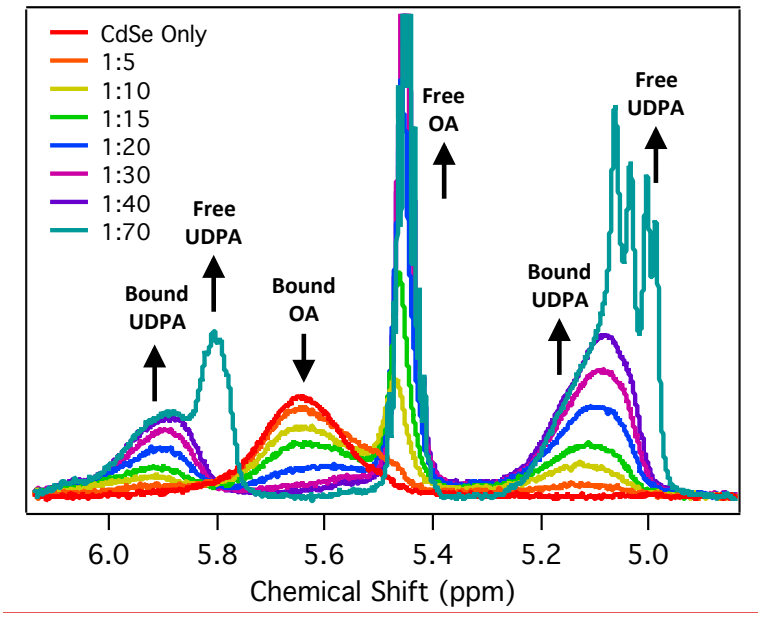

Figure 2.17: ^{1}H NMR spectrum of 100 μM CdSe QDs titrated with UDPA in toluene-d_8 (600 MHz). Legend indicates the QD:UDPA ratio in solution.

To probe the reversibility of this exchange, UDPA-capped QDs were isolated by a single precipitation with ethanol at the end point of the titration. The UDPA-capped QDs were then immediately dispersed in toluene-d_8 (Figure 2.18). Upon the addition of OA to the

UDPA-capped QD, only free OA is observed in the ^{1}H NMR spectrum indicating that carboxylic acids do not displace phosphonic acid ligands on CdSe surfaces under these conditions. By contrast, when excess octylphosphonic acid is added to UDPA-capped QDs, free UDPA ligand is observed in the ^{1}H NMR spectrum (Figure 2.19), indicating that phosphonic acid-terminated ligands can displace other phosphonic acid ligands. The limited stability of the UDPA-capped QDs limited us from studying this exchange reaction in more depth.

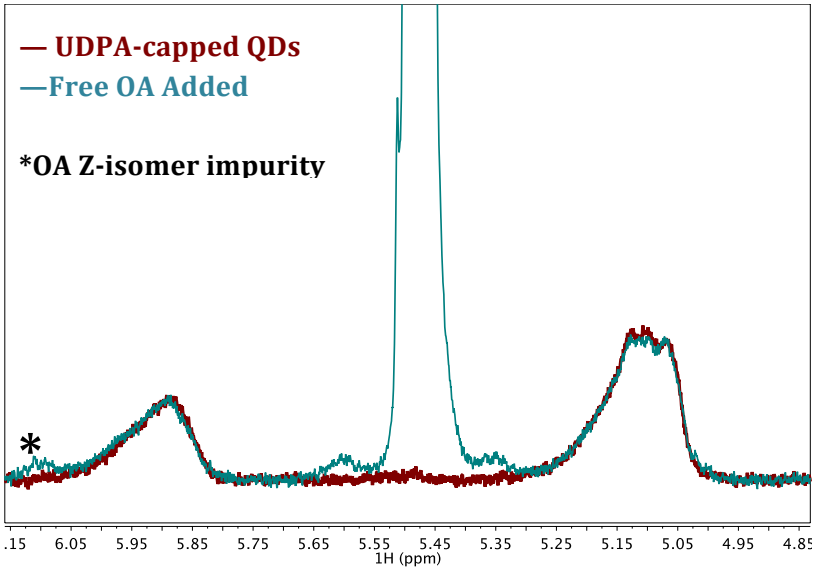

Figure 2.18: 600 MHz ^{1}H NMR spectrum of CdSe QDs capped with UDPA before (maroon) and after (teal) the addition of free OA. The starred peak indicates the Z-isomer of OA that is present in lab grade OA.

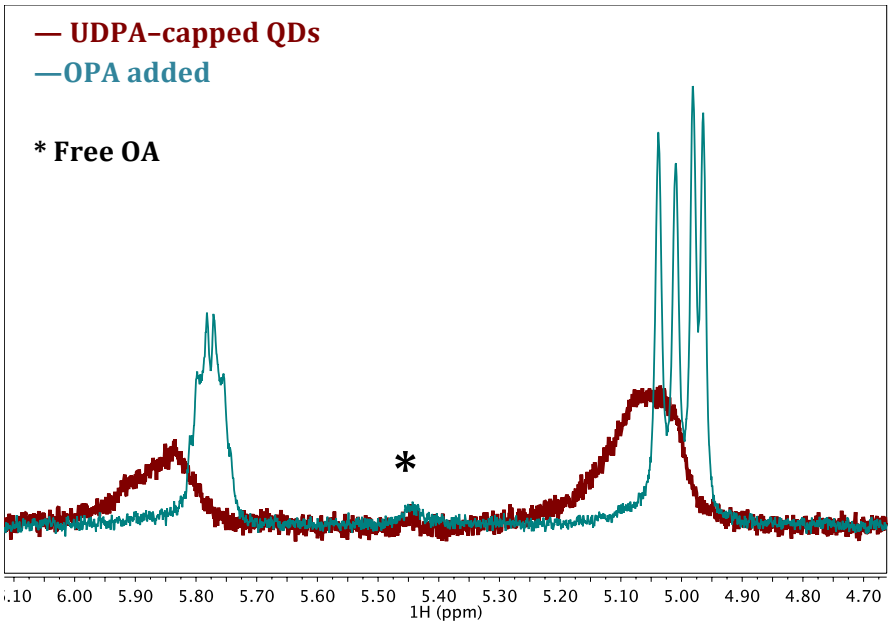

Figure 2.19: 600 MHz ^{1}H NMR spectrum of CdSe QDs capped with UDPA before (maroon) and after (teal) the addition of free octylphosphonic acid (OPA). The starred peak indicates residual free OA.

Figure 2.20 shows the absorbance and PL spectra of CdSe QDs titrated with UDPA. Upon addition of UDPA, the excitonic absorption peaks red shift by 5 nm and decrease slightly in intensity. The absorbance feature at 420 nm also decreases in intensity, and the $1S_e \leftarrow 2S_{h3/2}$ peak at 476 nm flattens slightly. The PL of the quantum dots is 98% quenched with 130 equivalents of UDPA. Similar results were obtained upon titration with octylphosphonic acid. The changes in the absorption spectrum and PL intensity suggest that the irreversibility of the phosphonic acid exchange arises because the NC surface is altered during the exchange.

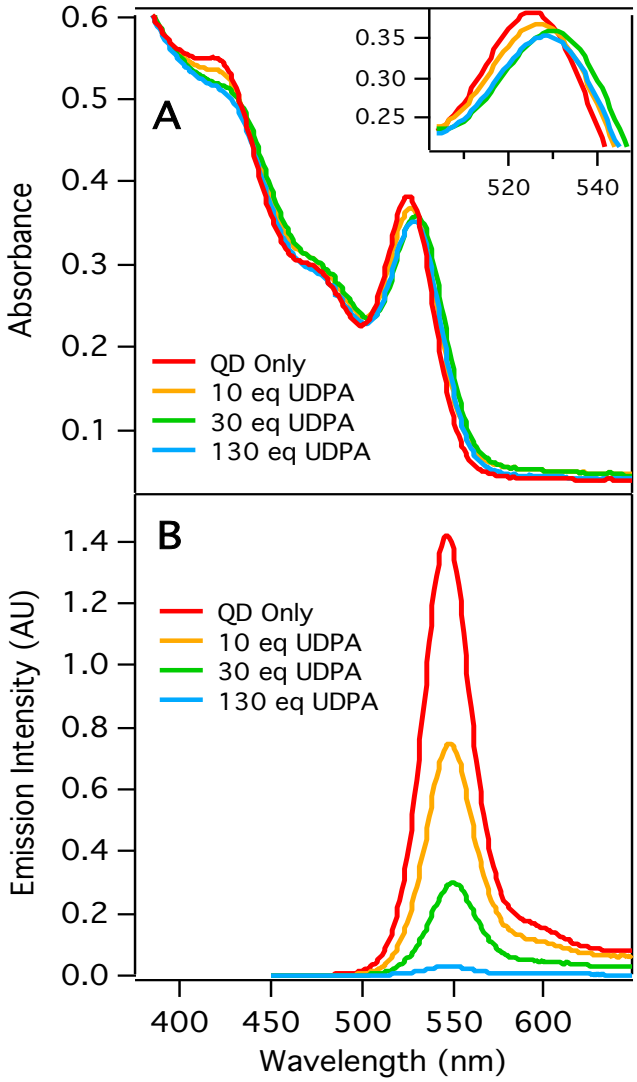

Figure 2.20: A) Absorption spectrum of 2.3 μM CdSe QDs in toluene titrated with UDPA. **B)** Steady-state PL spectrum (425 nm excitation) of 2.3 μM CdSe QDs in toluene titrated with UDPA.

Of note, when concentrations of UDPA greater than necessary to quantitatively displace the native OA ligands are added, the excitonic absorbance feature begins to blue shift (2 nm with 130 equivalents added). This blue shift does not occur when stoichiometric amounts of N,N-diisopropylethylamine are present (1:1 UDPA:base or 1:2 UDPA:base), and the PL quenching plateaus at 90% rather than >98% under these conditions (Figure 2.21). Further, samples with excess UDPA were found to degrade overnight, as evidenced by

bleaching of all excitonic absorbance features (Figure 2.22). These data suggest excess phosphonic acid leads to etching of zinc blende CdSe nanocrystals.

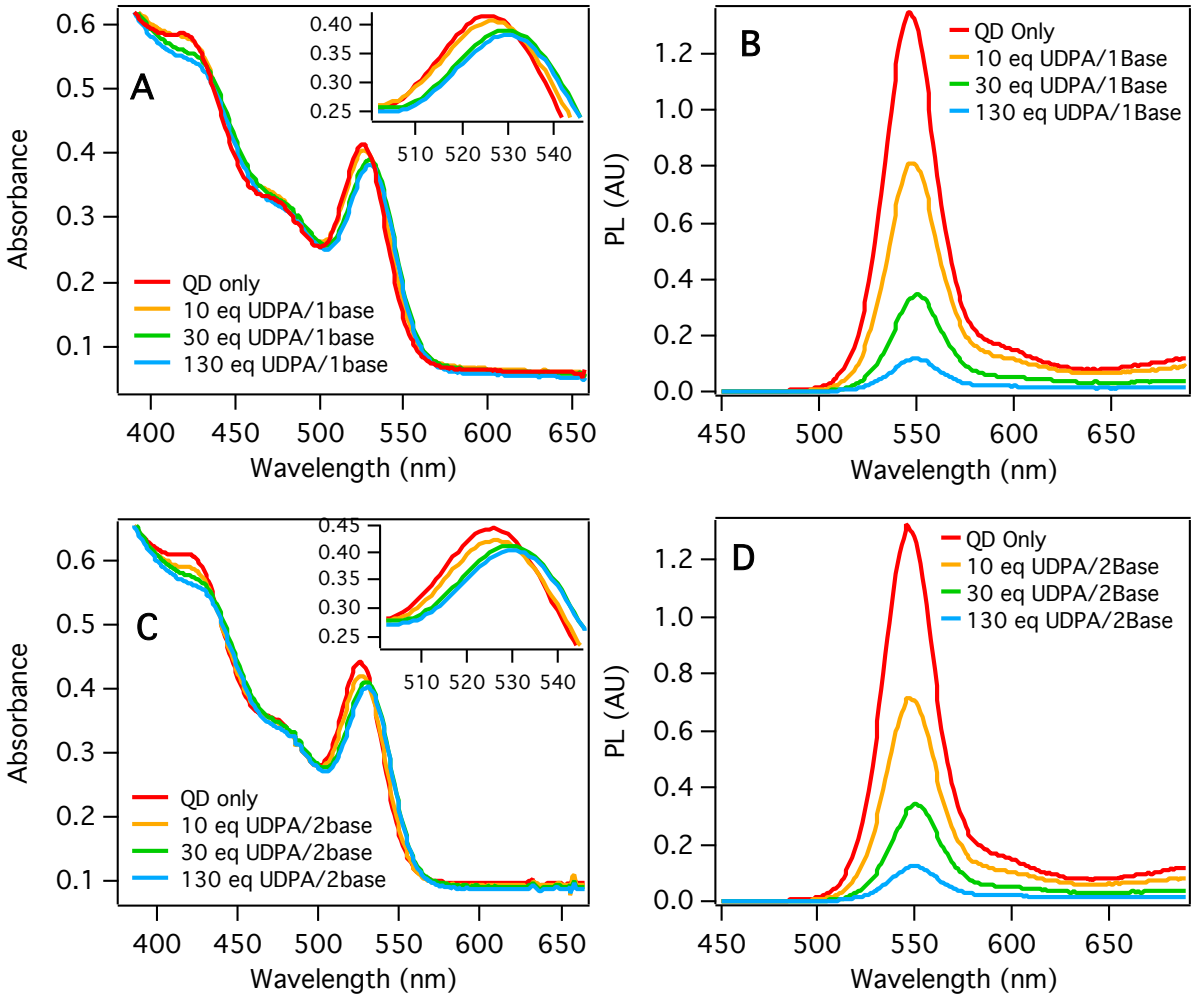

Figure 2.21: **A)** Absorption spectrum of 2.3 μM CdSe QDs in toluene titrated with UDPA and 1 equivalent N,N-diisopropylethylamine. **B)** Steady-state PL spectrum (425 nm excitation) of 2.3 μM CdSe QDs in toluene titrated with UDPA and 1 equivalent N,N-diisopropylethylamine. **C)** Absorption spectrum of 2.3 μM CdSe QDs in toluene titrated with UDPA and 2 equivalents N,N-diisopropylethylamine. **D)** Steady-state PL spectrum (425 nm excitation) of 2.3 μM CdSe QDs in toluene titrated with UDPA and 2 equivalents N,N-diisopropylethylamine.

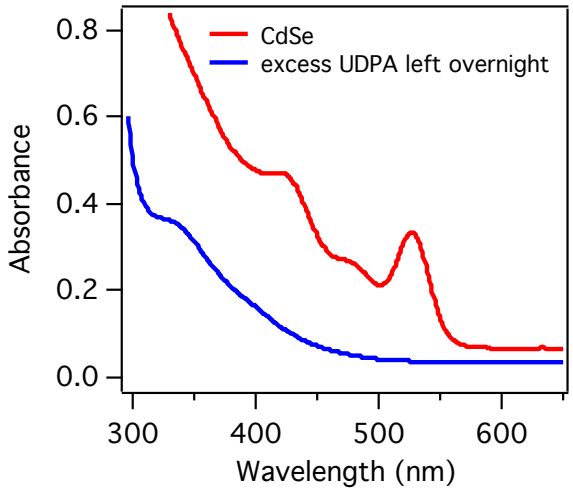

Figure 2.22: Absorbance of 2 μM QDs CdSe QDs (red) exposed to excess UDPA for 2 days (blue).

2.3.5. Ligand Exchange with Thiol-Terminated Ligands

Undec-10-ene-1-thiol (UDT) was synthesized by a nucleophilic substitution of 11-bromoundecene with potassium thioacetate. Upon addition of UDT (10 eq.) to OA-capped CdSe NCs, both the bound (δ 5.95 and 5.13 ppm) and free (δ 5.77 and 5.01 ppm) forms of UDT are observed in the ^{1}H NMR spectrum (Figure 2.23). Peaks corresponding to both the bound and free forms of UDT increase with increasing additions of UDT. However, unlike for the carboxylic acid exchange, the vinylic proton resonances of UDT appear as sharp signals with distinct splitting patterns.

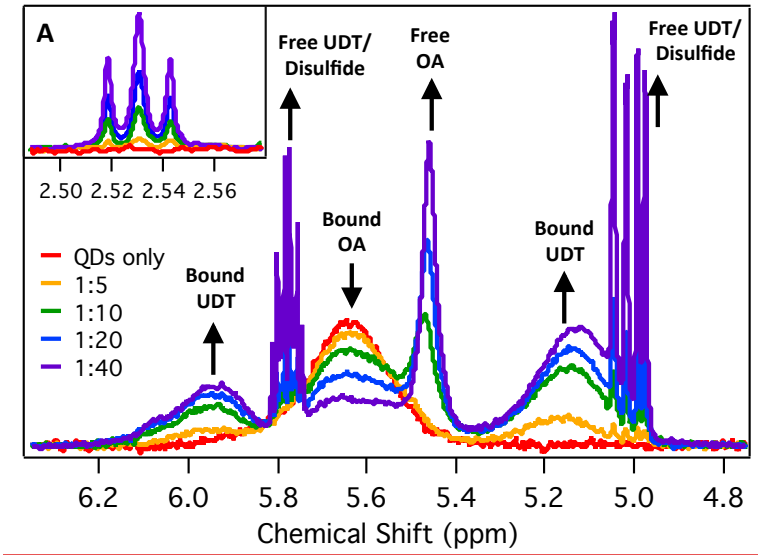

Figure 2.23: 600 MHz ^{1}H NMR spectrum of 100 µM CdSe QDs titrated with UDT in toluene-d_8. Legend indicates the QD:UDT ratio in solution. Inset A: Upfield region of the NMR titration showing the Triplet peak which indicates disulfide formation.

We initially attributed this observation to slow exchange kinetics, but then also considered that these peaks could arise from the corresponding disulfide. A disulfide molecule would be unable to bind to the QD surface, and thus would exist only in the free form in solution and give rise to a sharp resonance in the ^{1}H NMR spectrum. It has previously been reported that CdSe QDs catalyze the formation of disulfides from thiol ligands, even in ambient light.[55,129,130] In the free thiol, the protons alpha to the thiol group appear as an overlapping doublet of triplets splitting pattern (apparent quartet, coupling to the thiol proton and adjacent CH_2 protons are very similar) and have a chemical shift of 2.20 ppm. Upon disulfide formation, the resonance for these protons shifts downfield to 2.58 ppm and exhibits a clear triplet splitting pattern because coupling to the thiol proton is lost. Observation of this triplet signal at δ 2.58 ppm in our ^{1}H NMR (Figure 2.24) confirms that the disulfide is indeed produced under the conditions employed for the titration. Because the vinyl resonance of the disulfide has the same chemical shift as the free thiol, and we cannot

deconvolute the signals, we are unable to use this resonance as an indicator for free UDT in solution, as was done previously for UDA and UDPA. However, we were still able to obtain exchange ratios and perform reversibility experiments.

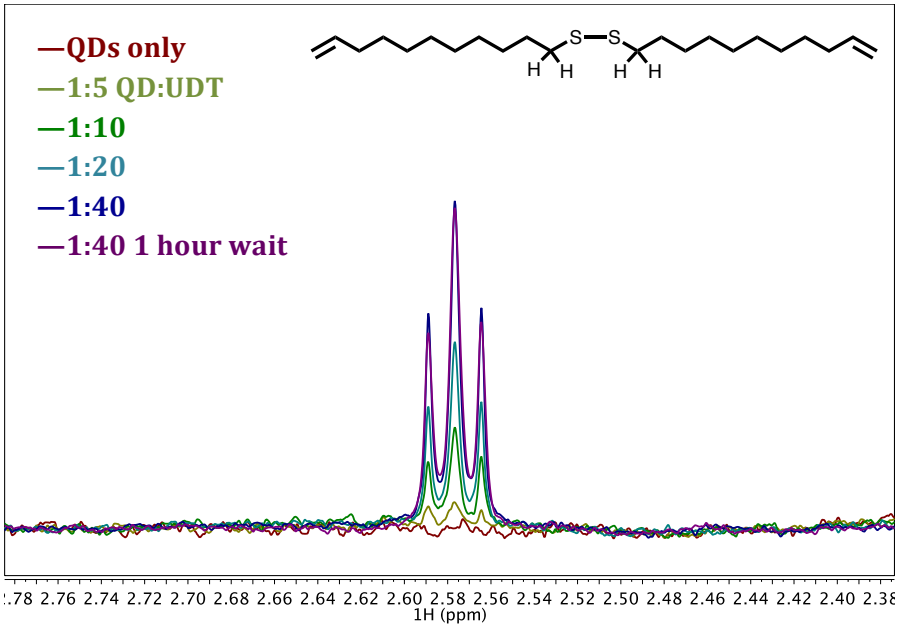

Figure 2.24: 600 MHz ^{1}H NMR spectrum of 100 µM CdSe QDs titrated with UDT in toluene-d_8. Legend indicates the QD:UDT ratio in solution. Triplet peak indicates disulfide formation.

Unlike the exchange reactions with carboxylic acids and phosphonic acids discussed above, for which a 1:1 exchange ratio is observed, the ratio of free OA to bound UDT is 1:2.3 for the first UDT addition (Table 2.2). This corresponds to a ligand density of 1.3 OA/nm^2 and 0.2 UDT/nm^2, giving a total ligand density of 1.5 ligands/nm^2. Upon successive titrations, this ratio approaches 1:1.6 (0.6 OA/nm^2 and 1.3 UDT/nm^2). This suggests that the thiols first bind to open coordination sites on the QD surface before displacing OA ligands. Additionally, the smaller size of the thiol anchoring group compared to a carboxylic acid or phosphonic acid could allow more thiol ligands to bind to the QD surface. Further, the monodentate binding nature of thiols also likely influences the binding stoichiometry.

Cossairt and coworkers have recently shown that carboxylic acids bind to InP nanoclusters in 4 modes, one of which involves symmetric bridging of two indium atoms.[161] If this bridging binding mode is also present for native oleate ligands on CdSe, the increased coverage of thiol ligands could result from displacement of carboxylic acids binding in this bridging motif. In order to maintain charge balance in these various ligand exchange processes, the ligands binding open coordination sites are likely doing so as neutral thiols, while those displacing the native oleate ligands undergo a proton transfer reaction and bind as thiolates. Alternatively, Z-type $Cd(oleate)_2$ ligands may be involved in exchange in order to maintain charge balance.

Table 2.2: Ligand exchange ratios obtained for different additions of UDT to a sample of OA-capped CdSe QDs.

[UDT] added (M)	$[OA]_F$:$[UDT]_B$	OA Coverage (OA/nm^2)	UDT Coverage (UDT/nm^2)	Total ligand Coverage ($Ligands/nm^2$)
0.0005	1:2.30	1.3	0.2	1.5
0.001	1:2.11	1.2	0.4	1.6
0.002	1:1.89	1.1	0.5	1.6
0.003	1:1.71	1.0	0.6	1.6
0.006	1:1.62	0.8	1.0	1.8
0.008	1:1.59	0.6	1.3	1.9

In order to probe the reversibility of this exchange, UDT-capped QDs were isolated by a single precipitation with ethanol after addition of excess UDT. The QDs were then immediately dispersed in toluene-d_8. Free thiol/disulfide is still observed after a single cleaning with ethanol (Figure 2.25), but further purification attempts led to loss of solubility in toluene. Upon the addition of OA to these isolated UDT-capped NCs, only free OA is observed, suggesting that thiolate ligands cannot be displaced by carboxylic acids.

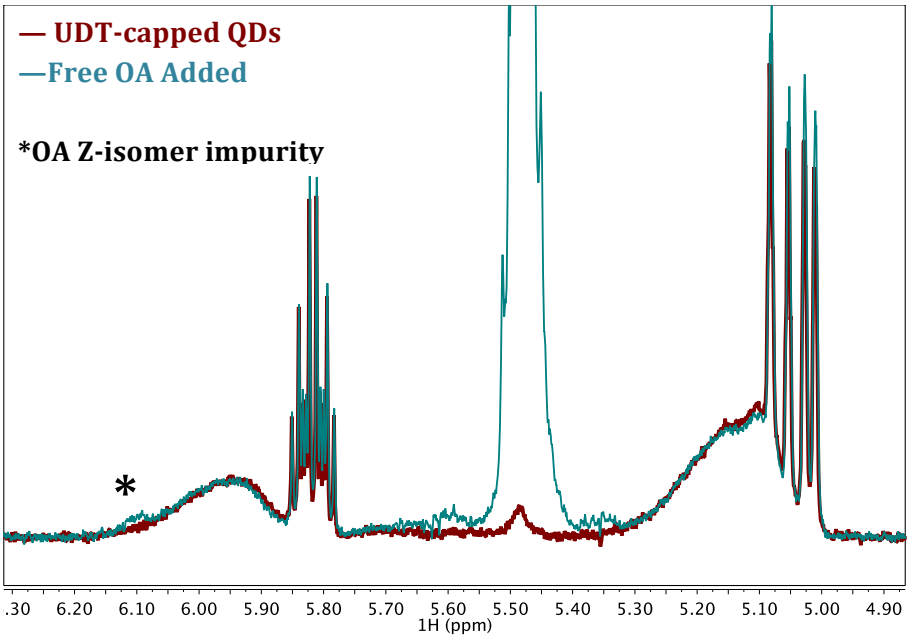

Figure 2.25: 600 MHz ^{1}H NMR spectrum of CdSe QDs capped with UDT before (maroon) and after (teal) the addition of free OA. The starred peak indicates the Z-isomer of OA that is present in lab grade OA.

We also examined the absorbance and emission of CdSe QDs upon titration with dodecanethiol (Figure 2.26). Upon addition of dodecanethiol, the excitonic absorbance peak red shifts by 2 nm, and an increase in intensity is observed over the entire absorbance spectrum. Though visually the sample did not seem to scatter light significantly, this absorption change is usually indicative of increased scattering in a sample, which could be due to ligand loss from the oxidation of surface ligands to disulfides. The red shift observed may be due to excitonic delocalization over the stronger binding thiol ligands which has been reported previously for dithiocarbamate ligands.[65,162] Quenching of the steady-state PL spectrum is also observed, consistent with prior observations for nanocrystals exposed to *n*-alkane thiols and generally attributed to hole transfer to thiol-terminated ligands.[65,129,140,141,163–165]

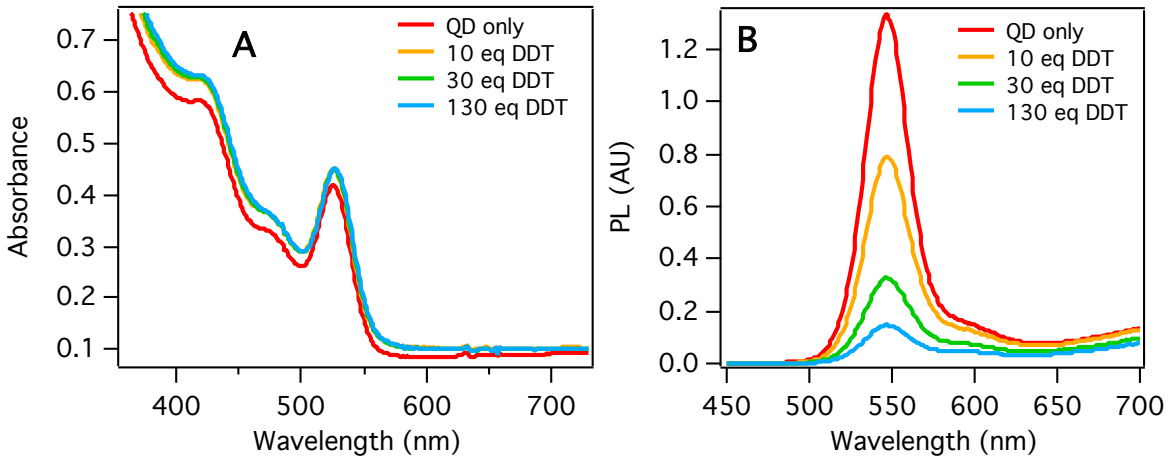

Figure 2.26: **A)** Absorption spectrum of 2.3 μM CdSe QDs in toluene titrated with dodecanethiol (DDT). **B)** Steady-state PL spectrum (425 nm excitation) of 2.3 μM CdSe QDs in toluene titrated with DDT.

2.4. Conclusions

Ligand exchange reactions at CdSe nanocrystal surfaces employing a family of ligands with various surface anchoring groups (carboxylic acid, phosphonic acid, and thiol) and terminal alkene functionalities have allowed us to quantify the relative concentrations of free and surface-bound forms of both the exchange ligand as well as the native oleic acid ligand via ^{1}H NMR spectroscopy. The addition of undec-10-enoic acid to OA-capped quantum dots results in a surface equilibrium between the two ligands (K_{eq} = 0.83). UDA exchanges in a 1:1 stoichiometry with native oleic acid, with no binding to open surface sites observed. Absorbance and emission experiments suggest this exchange occurs purely between surface ligands, and the surface metal atoms remain unaltered during the exchange. Undec-10-en-1-ylphosphonic acid irreversibly displaces OA ligands from CdSe QDs with a 1:1 stoichiometry. Absorption and emission experiments suggest that the surface metal atoms may be involved in this exchange reaction, and prolonged exposure to free phosphonic acids leads to etching of the QDs. Undec-10-ene-1-thiol also irreversibly displaces native OA ligands, with a ligand exchange stoichiometry of 1:1.6 free OA to bound UDT. A higher

(1:2.3) exchange ratio is initially observed suggesting thiols first bind to open sites on the QDs before displacing OA ligands. However, production of a disulfide product is observed when UDT is added to CdSe QDs, which limits the long-term stability of these ligands.

CHAPTER 3. Revealing the Relationship between Semiconductor Electronic Structure and Electron Transfer Dynamics at Metal Oxide-Chromophore Interfaces

Reprinted with permission from Knauf, R. R.; Brennaman, M. K.; Alibabaei, L.; Norris, M. R.; Dempsey, J. L. Revealing the Relationship between Semiconductor Electronic Structure and Electron Transfer Dynamics at Metal Oxide-Chromophore Interfaces. *J. Phys. Chem. C* **2013,** *117* (48), 25259-25268.

3.1. Introduction

Solar energy conversion technologies, including dye-sensitized solar cells and dye-sensitized photoelectrosynthesis cells may provide access to a sustainable-energy based future.[10,45,81] Both DSSC and DSPEC devices rely on chromophores bound to nanocrystalline wide-band-gap semiconductors. In these devices, photoexcitation of the chromophore promotes rapid charge injection from the dye into the conduction band of the semiconductor. In a DSSC, voltage produced by the charge separated state is used to drive a load while in a DSPEC, redox equivalents generated are used to promote fuel-forming catalysis.

Ultimately, the performance of these and similar devices are dictated by the rates and efficiencies of various electron transfer processes, including electron injection, back electron transfer, charge transport and fuel formation reactions. Significant research efforts have been put forth to elucidate the dynamics of these processes and understand the device parameters that influence them. These collective studies have contributed to a deeper understanding of device mechanism and performance, but the complex semiconductor structures and intricate charge transport mechanisms have yet to be fully elucidated. To date, the vast majority of these studies for device applications have focused on nanocrystalline TiO_2-based systems,

though other semiconductor materials, including SnO_2, Nb_2O_5, and ZnO, have warranted investigation.[83,107,166,167] In the context of a DSPEC anode material, SnO_2 is an attractive alternative to TiO_2. The SnO_2 conduction band is 0.4 V positive of TiO_2,[83,107,108] compatible with a variety of chromophores that feature weakly reducing excited states and in turn, have ground state oxidation potentials capable of driving water oxidation catalysis. Despite the promise of SnO_2, the intrinsic and interfacial electron dynamics are less well studied for this material than for TiO_2.

In this study, we utilize nanosecond laser flash photolysis to evaluate the kinetics of back electron transfer between injected electrons and oxidized surface-bound ruthenium chromophores in aqueous conditions. The semiconductor-chromophore systems explored in this study include both TiO_2 and SnO_2 nanoparticle films with bound ruthenium chromophores containing phosphonate linkers for stable surface binding, $[Ru(bpy)_2(4,4'\text{-}(PO_3H_2)_2bpy)]^{2+}$ (RuP) and $[Ru(bpy)_2(4,4'\text{-}(CH_2PO_3H_2)_2bpy)]^{2+}$ ($RuCH_2P$) (bpy = 2,2′-bipyridine, 4,4′-$(PO_3H_2)_2$bpy = 4,4′-bis(phosphonic acid)-2,2′-bipyridine; 4,4′-$(CH_2PO_3H_2)_2$bpy = 4,4′-bis(methylphosphonic acid)-2,2′-bipyridine).[46,168] Systematic variations of pH, excitation intensity, and chromophore linker have allowed us to tune parameters including the conduction band edge potential, surface trap state identity, injection yields and electronic coupling. Complementary electrochemical measurements provide additional insight into the energetic distribution of sub-band-gap trap states. This side-by-side comparison of TiO_2 and SnO_2 has revealed details of charge recombination mechanisms and highlighted the influence of electron trap state identity on back electron transfer.

3.2. Experimental

3.2.1. Chromophore Synthesis

$[Ru(bpy)_2(4,4'\text{-}(PO_3H_2)_2bpy)]Cl_2$ (RuP) and $[Ru(bpy)_2(4,4'\text{-}(CH_2PO_3H_2)_2bpy)]Cl_2$ ($RuCH_2P$) were prepared by previously reported methods.[46]

3.2.2. Metal Oxide Film Fabrication

Screen-printed nanocrystalline TiO_2 films were prepared as previously reported with Dyesol (18NR-T transparent titania paste, Dyesol, 20 nm particle diameter) on FTO-coated glass (Hartford Glass; sheet resistance 15 Ω cm^{-2}).[169] Nanocrystalline ZrO_2 films were prepared on FTO-coated glass via a previously reported procedure.[169] Nanocrystalline SnO_2 films were prepared using a modified literature preparation on FTO-coated glass.[100] To a rapidly stirred SnO_2 colloidal solution (37 g, 15% w/v, Alfa Aesar, 15 nm particle diameter), 1 g of glacial acetic acid was added dropwise. The resulting mixture was stirred at room temperature in a sealed container for 36 hours. The solution was then autoclaved at 240 °C for 80 hours, and allowed to cool. The resulting colloid was dispersed with a Branson Ultrasonics sonic horn for 3 minutes (50% duty cycle, 70% total power). Hydroxypropylcellulose (3 g, Aldrich, MW = 80,000) was then added slowly over 3 minutes. The resulting paste was stirred for several days prior to preparing films. Thin films were prepared using the doctor blade method with tape-casting and sintered at 450 °C for 120 minutes. All films were approximately 3.5 μm thick.

3.2.3. Surface Attachment

For this study, all chromophore-derivatized nanocrystalline films were fully loaded with dye. Sensitizers were anchored to the SnO_2 and TiO_2 nanocrystalline surfaces by

soaking mesoporous metal oxide film coated FTO electrodes overnight in room temperature 0.1 M $HClO_4$ aqueous solutions containing RuP (or $RuCH_2P$) with concentrations ranging from $1x10^{-5}$ M to $2x10^{-4}$ M. Slides were then soaked for at least 8 hours in 0.1 M $HClO_4$ aqueous solution to remove excess unanchored complexes. Absorptions measurements were made with an Agilent Cary 60 UV-Vis Spectrophotometer. Loaded slides were placed in a cuvette at 45° angle to the beam direction, the cuvette was filled with an aqueous solution of $HClO_4$, and samples placed under an Argon atmosphere. The background of the bare SnO_2 slide absorbance has been subtracted from the reported absorbances. Optical densities of the RuP–SnO_2, $RuCH_2P$–SnO_2 and RuP–TiO_2 films employed were nearly identical.

3.2.4. Transient Absorption Spectroscopy

Nanosecond to microsecond transient absorption experiments were performed using a commercially available laser flash photolysis system (Edinburgh Instruments, Inc., model LP920) with laser excitation (532 nm, 5-7 ns FWHM, typically 4.0 ± 0.1 mJ/pulse unless stated otherwise, 5 mm beam diameter, 20 mJ/cm^2) provided by a pulsed Nd:YAG laser (Spectra-Physics, Inc., model Quanta-Ray LAB-170-10) / OPO (VersaScan-MB) combination. To accommodate the pulsed, 1 Hz intensification of the 450 W Xe probe source of the LP920, the laser system was set such that the flashlamps were fired at 10 Hz yet Q-switched at 1 Hz. Timing of the experiment, including laser and probe pulsing, was computer controlled via Edinburgh software (L900) as was data collection with the aid of a Tektronix oscilloscope (model TDS-3032C). The LP920 white light probe output was passed through a 375 nm long pass color filter before passing through the sample to minimize band gap excitation of the metal oxide. The LP920 was equipped with a multi-grating detection monochromator outfitted with a Hamamatsu R928 photomultiplier tube

(PMT) in a non-cooled housing and a gated CCD (Princeton Instruments, PI-MAX3) such that detection was software selectable. Single wavelength transient absorption kinetics were monitored with the PMT (10 ns FWHM IRF, reliable data out to 400 μs, 300 nm – 900 nm) and the gated CCD was used for recording transient spectra covering the entire visible region (400-850 nm, 3 nm spectral bandwidth) at a given time after excitation (10 ns gatewidth). For PMT measurements, spectral bandwidth was typically <5 nm with color filters placed after the sample but before the detection monochromator to eliminate laser scatter. Data were the result of averaging 50-200 laser shots. Kinetic data were analyzed using Igor Pro (WaveMetrics Inc.) or L900 (Edinburgh, Inc.) software. Data were collected at room temperature (295 ± 3 K). Derivatized SnO_2 and TiO_2 films were inserted diagonally into a 10 mm path length quartz cuvette whose top had been adapted with a #15 o-ring sealing joint, sidearm, and Kontes valve. After addition of aqueous $HClO_4$ solutions (distilled water; 70% $HClO_4$, ACS reagent, Sigma-Aldrich) to the cuvette, the sample was sparged with argon for at least 45 minutes immediately prior to experiments.

3.2.5. Steady-State Emission

PL spectra were acquired with an Edinburgh Fluorescence Spectrometer (FLS920) equipped with integration sphere (1 nm step size, 10 nm bandwidth). Excitation was at 450 nm, with a 475 nm long-pass optical filter placed before the detector. Emission intensities at each wavelength were corrected for system spectral response. The integrating sphere was used as specified for a film-based sample, with the sample films placed face up on the sample platform. Aqueous $HClO_4$ of specified pH was dropped on top of the slide, and the sample was covered with a microscope cover slip. Emission spectra have been absorbance adjusted.

Background spectra of the bare metal oxides (ZrO_2 and SnO_2) were also taken and subtracted from the reported emission spectra.

3.2.6. Electrochemical Measurements

Electrochemical measurements were performed using the nanostructured metal oxide/FTO film as the working electrode in a standard three-electrode cell with a Ag/AgCl (3 M NaCl) reference electrode and a Pt wire counter electrode. Areas of bare FTO on the working electrode were covered with Kapton tape to eliminate background current. Aqueous solutions containing 0.1 M $NaClO_4$ ($NaClO_4 \bullet H_2O$, 99%, EM Science) as the supporting electrolyte were adjusted to indicated pH values with $HClO_4$ and NaOH. Measurements were made at room temperature with a WaveNow potentiostat (Pine Instruments) controlled by Aftermath software (Pine Instruments). Cyclic voltammograms (CVs) were recorded at a scan rate of 20 mV/s. Multiple CVs were collected until the voltammogram showed no changes from the previous cycle. The CVs reported are the resulting 3rd or 4th cycles. Data were processed using Igor Pro (Wavemetrics). Open circuit potential (OCP) measurements were in the dark, in pH 1 $HClO_4$ with no supporting electrolyte (identical conditions to samples utilized in transient absorption measurements). OCP readings were taken after the voltage had stabilized (~20 minutes) within an error of ±10 mV.

3.2.7. Spectroelectrochemical Measurements

Spectroelectrochemical measurements were made with an Agilent Cary 60 UV-Vis Spectrophotometer and the setup described above for electrochemical measurements. The SnO_2/FTO working electrode was placed at 45° angle in a modified cuvette containing an aqueous solution of Argon sparged aqueous $HClO_4$. The optical compartment of the cuvette was modified with an extended sample compartment out of the spectrometer beam path

which held the reference and counter electrodes. Linear staircase voltammetry was used with a step size of 50 mV and a 2 minute hold time at each potential. The potential was stepped fromm +0.45 V to –0.4 V vs. Ag/AgCl and absorbance spectra were measured at each interval. The spectra are reported the difference of the absorbance at the specified applied voltage minus the absorbance at 0.45 V, $Abs_{Applied} - Abs_{0.45V}$.

3.3. Results

3.3.1. RuP–SnO_2 Characterization

Adsorption of RuP-SnO_2 was measured as a function of solution immersion time to obtain an adsorption isotherm shown in Figure 3.1; the intensity of the metal-to-ligand charge-transfer (MLCT) absorption increases with surface coverage and plateaus as a complete monolayer of dye is formed. The loading isotherm indicates complete surface coverage is achieved within 120 minutes of loading slides in $1x10^{-4}$ M RuP in a 0.1 M $HClO_4$ aqueous solution. RuP–SnO_2 and RuP–TiO_2 films utilized in the experiments described below were all loaded overnight to ensure complete surface coverage. A surface coverage dependence was not investigated here yet prior studies on RuP–TiO_2 indicated charge recombination dynamics vary with surface loading presumably arising from the disparate number of electrons injected which simulates an applied bias effect.[170] The maximum surface coverage for SnO_2 films were calculated as previously reported for TiO_2.[170]

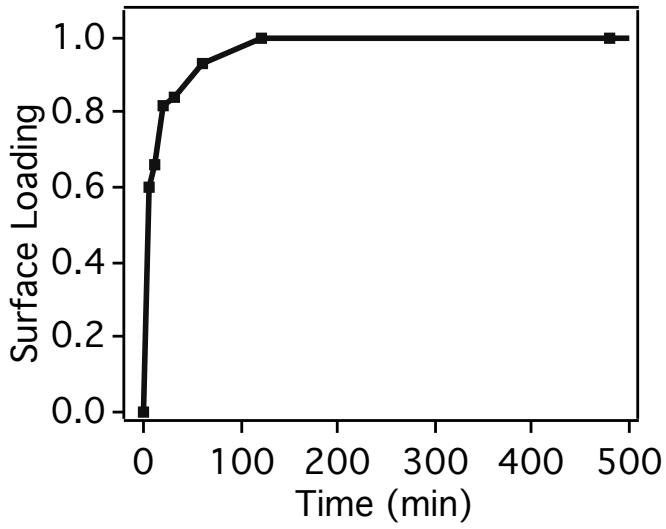

Figure 3.1: Surface loading isotherm for RuP–SnO_2.

The absorption spectra of the RuP–SnO_2 films is dominated in the visible region by the metal-to-ligand charge-transfer absorption (λ_{max} = 455 nm) of RuP with contributions from both $d\pi \rightarrow \pi^*(bpy)$ and $d\pi \rightarrow \pi^*(bpy(PO_3H_2)_2)$ transitions (Figure 3.2). The MLCT absorbance feature undergoes a slight hypsochromic shift when the solution pH is increased from pH 1 to pH 3 (Figure 3.2, inset), consistent with observations of RuP–TiO_2.[170] The spectral shifts are attributed to proton loss from phosphonate groups of the surface bound RuP chromophore, which has a pK_a of ~2 when bound to TiO_2.[171] The absorbance of the RuP–SnO_2, $RuCH_2P$–SnO_2 and RuP–TiO_2 films utilized for experiments were comparable, indicating equivalent surface loading.

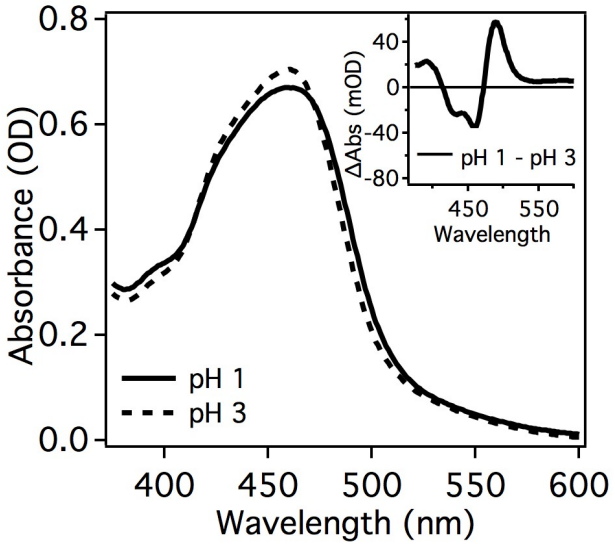

Figure 3.2: Absorption spectra of RuP loaded on SnO_2 (SnO_2 absorption background subtracted) in pH 1 and pH 3 aqueous $HClO_4$ solutions. Γ = 7.5 x 10^{-8} mole•cm^{-2}. Inset: Absorption difference spectrum between pH 1 and pH 3.

3.3.2. Steady-State Photoluminescence

Photoluminescence emission spectra (λ_{ex} = 450 nm) were obtained for RuP–ZrO_2 and RuP–SnO_2 as a function of pH (Figure 3.3). Emission spectra were collected in an integrating sphere and are corrected for the amount of light absorbed. The conduction band energy of ZrO_2 is significantly negative of the RuP^* oxidation potential; as such, electrons are unable to inject. For RuP–ZrO_2, there is a slight hypsochromic shift in the RuP PL maxima between pH 1 and 3, consistent with the absorbance spectra. This is attributed to proton loss from the surface bound phosphonate groups of the RuP chromophore ($pK_a \approx 2$). Further, the PL intensity of RuP–ZrO_2 changes very little with pH. By contrast, the PL intensity of RuP–SnO_2 is almost completely quenched; at pH 1, the PL intensity of RuP–SnO_2 is less than 1% of that for RuP–ZrO_2. This emission quenching, along with long lived transient bleach signals (hundreds of μs) and the relatively high oxidation potential of RuP gives strong evidence for efficient electron injection into SnO_2.

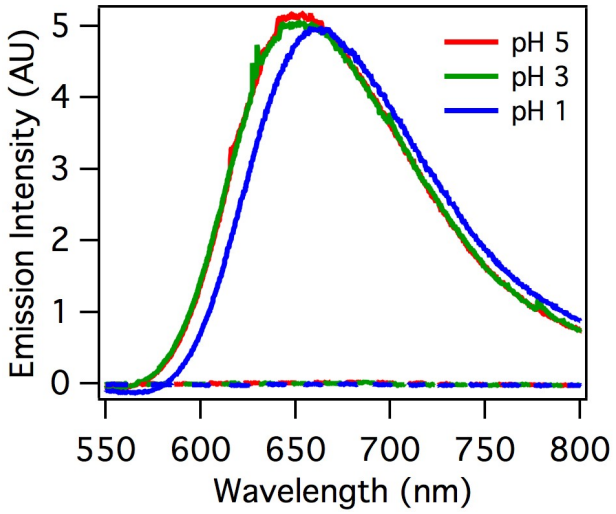

Figure 3.3: Background corrected emission spectra of RuP on ZrO_2 (solid lines) and SnO_2 (dashed lines) in pH 1, 3, and 5 aqueous $HClO_4$ solutions.

The bare ZrO2 and has a minor emission peak centered at 660 nm which is less than 5% of the emission intensity of RuP on ZrO_2. This background PL is subtracted from the spectra in Figure 3.3. The SnO_2 slides show this same emission background (Figure 3.4), suggesting it arises from light scattering which is unaccounted for by the integrating sphere correction. However, the emission of RuP on SnO_2 is extensively quenched (Figure 3.3, suggesting near 100% injection), and as such, the emission spectrum is dominated by this background feature. The SnO_2 PL background is subtracted from the RuP–SnO_2 spectra in Figure 3.5. The RuP-SnO_2 PL intensity is less than 1% of RuP–ZrO_2 PL, as such the signal intensities recorded for RuP–SnO_2 PL are near the instrument detection limits (Figure 3.5). It is possible that the small differences observed with pH for the RuP–SnO_2 PL may be simply due to sample variation.

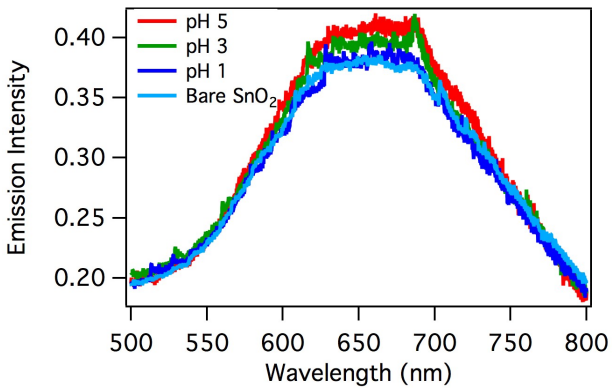

Figure 3.4: Raw steady-state emission spectra of RuP–SnO_2 in pH 1, 3, and 5 aqueous $HClO_4$ solutions, as well as the emission spectrum of bare SnO_2 collected in an integrating sphere.

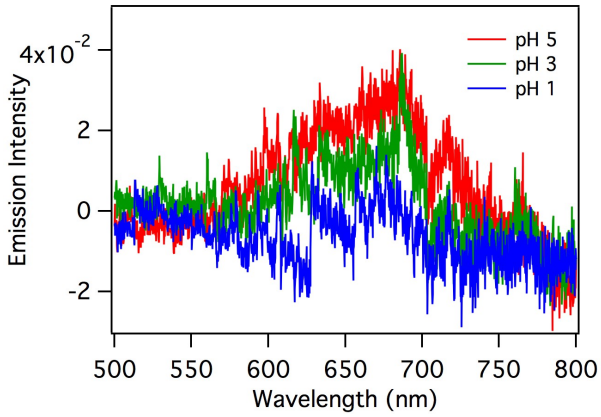

Figure 3.5: Background emission/scatter corrected steady-state emission spectra of RuP–SnO_2 in pH 1, 3, and 5 aqueous $HClO_4$ solutions.

The quenching of RuP–SnO_2 PL decreases slightly with increasing pH, indicating injection efficiency is highest at low pH values (Figure 3.4), although these differences are minute. Kinetics traces recorded for RuP–SnO_2 (discussed below) better illustrate the increased injection yields observed with decreasing pH, where the ΔAbs_{max} increases by a factor of ~2 from pH 5 to pH 1. These observations are consistent with previously observed behavior of RuP–TiO_2.[170] Kinetics traces obtained from TA experiments also indicate that injection yields for RuP–SnO_2 and RuP–TiO_2 are comparable at pH 1(vide infra).

3.3.3. Interfacial Charge Recombination Dynamics

Transient absorption spectra (Figure 3.6) were measured as a function of delay time relative to pulsed laser excitation of RuP–SnO_2 (λ_{ex} = 532 nm). The difference spectra are dominated by a bleach centered at 460 nm, corresponding to the oxidized chromophore. A low intensity broad absorption on the low energy side of the spectrum is also observed. Spectroelectrochemical measurements of bare SnO_2 films (Figure 3.7) show a similar broad absorption feature beginning near 600 nm when the films are reduced electrochemically, by comparison to similar observations made for reduced TiO_2[45,172–175] this feature is assigned to $SnO_2(e^-)$.

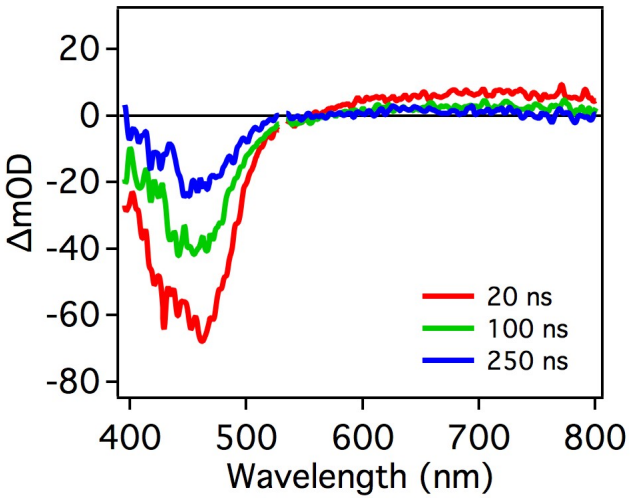

Figure 3.6: Transient absorption spectra of RuP–SnO_2 in pH 1 $HClO_4$, following 532 nm excitation, at various time delays. Excess noise was filtered from the data by using 3 passes of binomial smoothing.

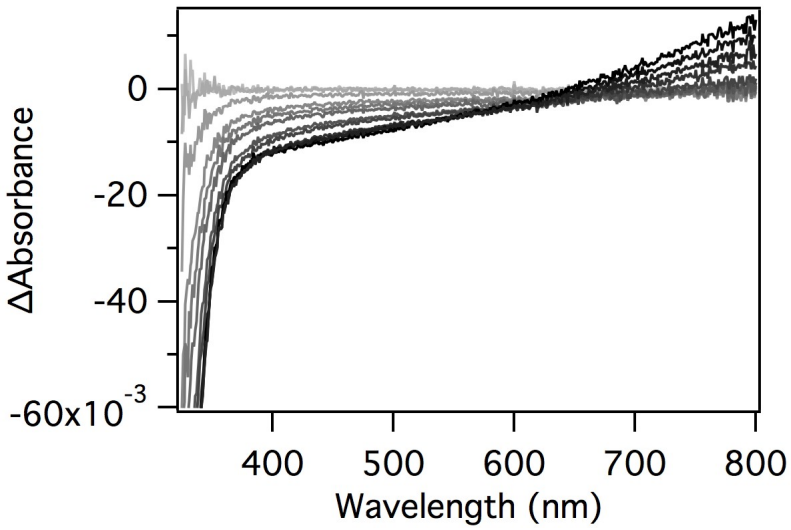

Figure 3.7: Spectroelectrochemical measurements of SnO_2 in aqueous pH 1 $HClO_4$. Difference spectra shown are of the absorbance at the applied voltage minus the absorbance at 0.45 V, $Abs_{Applied} - Abs_{0.45V}$, (grey to black) with applied voltages ranging up to –0.4 V vs. Ag/AgCl in 50 mV steps (some steps omitted for clarity).

These transient spectral features indicate rapid electron injection to form the charge separated state $Ru^{3+}P–SnO_2(e^-)$. The intensity of the transient spectral features decreases on the order of microseconds, corresponding to charge recombination (back electron transfer, BET). Similar observations have previously been reported for $RuP–TiO_2$.[170]

Charge recombination dynamics for $RuP–SnO_2$ and $RuP–TiO_2$ were monitored via single wavelength transient absorption. Nearly identical kinetics were obtained at 400 nm (ground-state/excited-state isosbestic point[176]) and 450 nm (near the maximum of the transient bleach). Kinetics analyses, discussed below, were carried out on traces collected at the ground-state/excited-state isosbestic point (Figure 3.8). The magnitude of the bleach upon photoexcitation is comparable for the two systems under identical conditions (pH 1, 4 mJ pulse energy, fully loaded films), indicating similar injection yields are achieved for the two metal oxide systems.

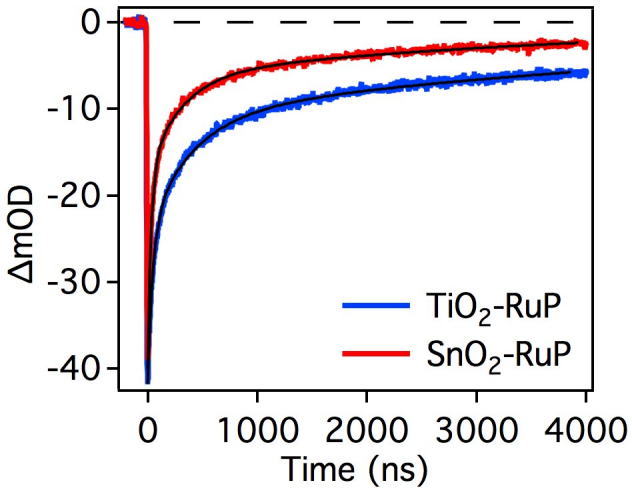

Figure 3.8: Transient absorption spectral changes of RuP–SnO_2 (red) and RuP–TiO_2 (blue) monitored at 400 nm following 532nm excitation (4 mJ) in pH 1 aqueous $HClO_4$ solution.

The recombination dynamics for both RuP–TiO_2 and RuP–SnO_2 are highly complex, as has been observed in similar studies.[23,45,177] BET occurs over a broad span of timescales (nanoseconds – milliseconds) with kinetics that have been fit by various models in related studies. One approach utilizes equal-concentration second-order kinetics, or a sum of equal-concentration second-order components, which models recombination of the charge separated state Ru^{3+}–$MO_x(e^-)$ in an analogous fashion to solution-based charge-recombination processes.[45,94,95,97] Another method applies the Kohlrausch-Williams-Watts distribution, or a stretched exponential, to fit the transient to a Levy distribution of rate constants based on the distribution of localized trap states and a 'continuous-time random walk' model.[45,178–180] Here, we utilize a third approach—a tri-exponential function.[168,170] This model has previously been used in related systems when neither of the above models can provide a satisfactory fit to the kinetic data, and was chosen here in order to provide direct comparison to previous related reports of BET dynamics in RuP–TiO_2. While the triexponential model has no implication toward a functional form derived from physically

relevant reaction pathways, it is used to quantitatively track and compare dynamics between data sets.

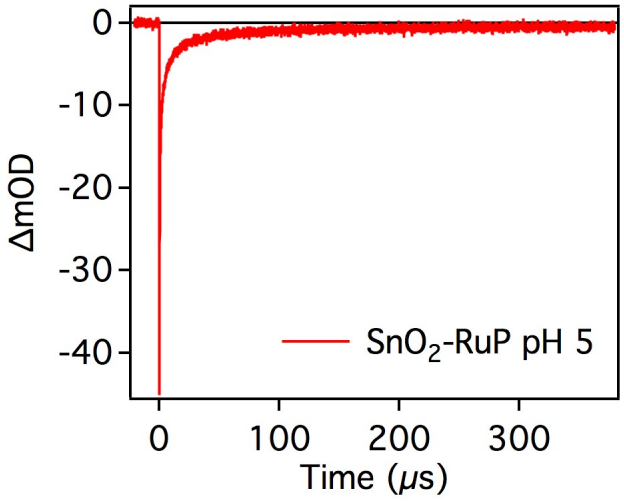

Figure 3.9: Kinetics trace of RuP–SnO_2 monitored at 400 nm following 532 nm excitation (4mJ) in pH 5 aqueous $HClO_4$ solutions.

Two major kinetics processes are observed—a fast component occurring on the microsecond timescale followed by a slower process on the timescale of hundreds of microseconds (RuP–SnO_2) or milliseconds (RuP–TiO_2) (Figure 3.9, Reference 170). Due to current instrumentation limitations, we were unable to obtain satisfactory measurements of the long component dynamics. The short component, taken as the first 4 μs, which accounts for more than 75% of the total amplitude change, was fit to a tri-exponential function (Equation 3.1), and the longer component was examined qualitatively by the parameter ΔA_{slow} as in previous related studies of RuP–TiO_2, permitting direct comparison.[170] Error bars in Tables 3.1, 3.2, and 3.3 indicate the standard error of the mean values obtained from 3–4 independent measurements.

$$\Delta Abs = A_1 e^{-k_1 t} + A_2 e^{-k_2 t} + A_3 e^{-k_3 t} \quad (3.1)$$

$$\tau_i = 1/k_i; \ < \tau >= \sum A_i \tau_i^2 / \sum A_i \tau_i \quad (3.2)$$

The kinetics traces (λ_{obs} = 400 nm) for RuP–TiO_2 and RuP–SnO_2 at pH 1, and their respective fits, are presented in Figure 3.8. The BET in RuP–SnO_2 occurs at a faster rate than the TiO_2 system. Additionally, the RuP–SnO_2 recombination trace contains a smaller contribution from the long time component. Kinetic parameters for the two samples, presented in Table 3.1, indicate that recombination on the microsecond timescale is about twice as fast for RuP–SnO_2, but the time constants determined for the two systems are of similar magnitude. However, the amplitude contribution from the long time component (ΔA_{slow}) is nearly three times greater for RuP–TiO_2.

Table 3.1: Kinetic parameters from fits to transient absorption data in Figure 3 in pH 1 $HClO_4$. λ_{ex} = 532 nm (4 mJ), λ_{obs} = 400 nm.

	A_1	τ_1 (ns)	A_2	τ_2 (ns)	A_3	τ_3(ns)	<τ>(ns)	ΔA_{slow}[b]
RuP–SnO_2	0.02	27 ±3	0.01	260 ±10	0.006	3710 ± 170	3500	5.0 ±0.4
RuP–TiO_2	0.015	55 ±5	0.013	450 ±20	0.010	6500 ±200	5900	14 ± 0.5
RuP–TiO_2[a]	0.36	50	0.31	450	0.33	6000	5600	15

[a] Literature value for normalized TA data taken at 400 nm. Reference [170]
[b] Percent of the total signal remaining at 4 μs

3.3.4. pH Dependence Studies

Kinetics traces for RuP–SnO_2 measured at pH 1, 3, and 5 with equal excitation pulse energies (4 mJ) are shown in Figure 3.10. Corresponding kinetic parameters are presented in Table 3.2. The rate of recombination is attenuated as pH is increased; τ_1 doubles between pH

1 and pH 5, while τ_2 and τ_3 increase only slightly. The pH dependence observed for RuP–SnO_2 at equal excitation pulse energy is less significant than that observed in similar studies of RuP–TiO_2.[170] In the TiO_2 system studied previously, all three time constants (τ_1, τ_2 and τ_3) increase by a factor of ca. 2 when the pH is increased from pH 1 to pH 5 while ΔA_{slow} increases from 15 to 30 % in the same range.[170]

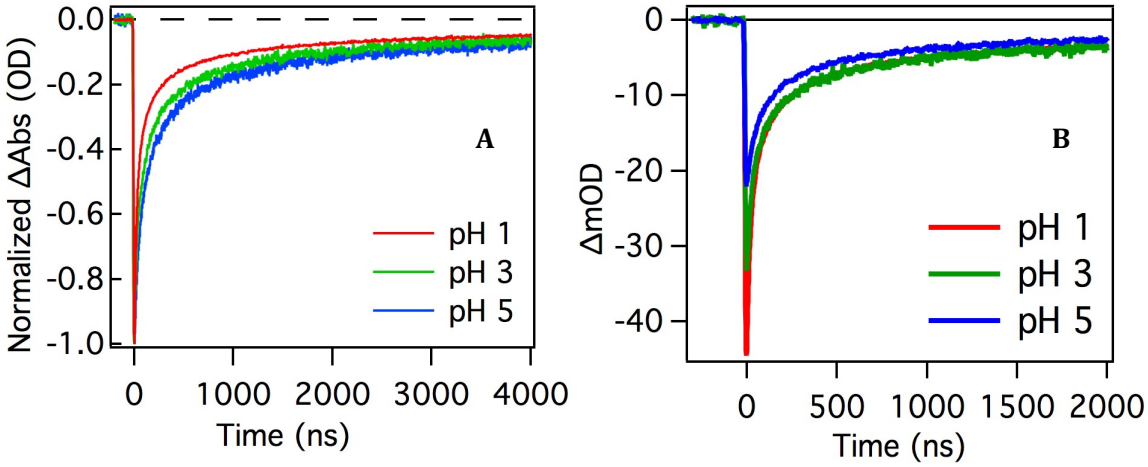

Figure 3.10: A) Normalized and **B)** un-normalized transient absorption spectral changes of RuP–SnO_2 monitored at 400 nm following 532 nm excitation (4mJ) in pH 1, 3, and 5 aqueous $HClO_4$ solutions.

Table 3.2: Kinetic parameters from fits to normalized transient absorption data in Figure 3.10A at pH 1, 3, and 5 $HClO_4$. λ_{ex} = 532 nm, λ_{obs} = 400 nm.

	Pulse Energy (mJ)	A_1	τ_1 (ns)	A_2	τ_2 (ns)	A_3	τ_3(ns)	<τ>(ns)	ΔA_{slow}[a]
pH 1	4	0.6	27 ±3	0.28	260 ±10	0.14	3700 ±170	3300	5.0 ± 0.4
pH 3	4	0.5	41 ±3	0.31	313 ±10	0.18	3950 ±140	3400	7.0 ±0.3
pH 5	4	0.45	62 ±3	0.33	403 ±20	0.19	4285 ±200	3600	9.0 ±1.2
[a] Percent of the total signal remaining at 4 μs									

Importantly, these kinetics traces (Figure 3.10B) indicate injection yields are inequivalent for samples at different pH, based on the magnitude of the bleach at 400 nm. It has ben previously shown for RuP-TiO_2 that increased laser intensity (and in turn a greater

number of injected electrons) leads to faster recombination rates.[170] As such, recombination dynamics were then measured for RuP–SnO_2 and RuP–TiO_2 as a function of pH with varied excitation pulse energies in order to achieve equivalent injection yields between samples, as determined by the magnitude of the bleach at 400 nm (Figure 3.11). Qualitatively, the RuP–TiO_2 sample series (Figure 3.11B) exhibits a significantly more dramatic pH dependence than the RuP–SnO_2 sample series (Figure 3.11A). The kinetic parameters (Table 3.3) indicate the pH dependence for BET in RuP–SnO_2 is minor; τ_1 and τ_2 increase slightly with increasing pH, while τ_3 decreases slightly. Importantly, ΔA_{slow} is nearly identical at each pH. On the other hand, the RuP–TiO_2 samples show a well-defined dependence on pH when injection yields are equivalent. The pH dependence for RuP–TiO_2 is completely manifested in the largest time constant (τ_3)–τ_1 and τ_2 remain constant for all three samples while τ_3 increases from 8.5 μs to 12.5 μs when the pH is increased from 1 to 5. Additionally, the amplitude contribution from the long time component for RuP-TiO_2 nearly doubles from 16% at pH 1 to 28% at pH 5, in stark contrast to the observations of RuP–SnO_2, where no significant change in ΔA_{slow} is observed in the same range.

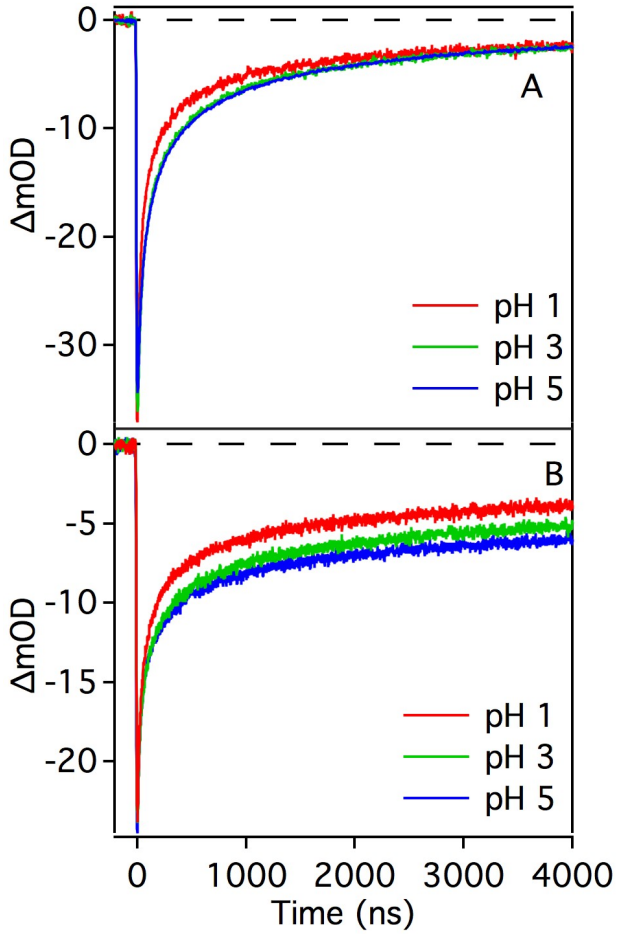

Figure 3.11: Transient absorption spectral changes of **(A)** RuP–SnO_2 and **(B)** RuP–TiO_2 monitored at 400 nm following 532 nm excitation in pH 1, 3, and 5 aqueous $HClO_4$ solutions. The pulse energies were varied to obtain the same maximum ΔAbsorbance (within ±3 mOD).

Table 3.3: Kinetic parameters from fits to transient absorption data in Figure 4. λ_{ex} = 532 nm, λ_{obs} = 400 nm.

Oxide	pH	Pulse Energy (mJ)	τ_1 (ns)	τ_2 (ns)	τ_3(ns)	<τ>(ns)	ΔA_{slow} [a]
RuP–SnO_2	1	3.5	30 ±3	310 ±10	4000 ±180	3300	6.5 ±0.5
RuP–SnO_2	3	3.8	50 ±5	360 ±15	3600 ±200	3100	7.0 ±0.5
RuP–SnO_2	5	4.2	50 ±5	380 ±20	3500 ±200	3000	7.5 ±0.5
RuP–TiO_2	1	3.5	50 ±5	430 ±10	8500 ±250	8000	16.0 ±1.0
RuP–TiO_2	3	3.9	50 ±5	430 ±10	10000 ±200	9700	22.5 ±1.0
RuP–TiO_2	5	4.2	50 ±5	430 ±10	12500 ±200	12200	28.0 ±1.5

[a] Percent of the total signal remaining at 4 μs

3.3.5. Electronic Coupling Studies

The effect of electronic coupling on the back electron transfer rates in RuP–SnO_2 was evaluated by comparing recombination dynamics to those of $RuCH_2P$–SnO_2. The driving force for electron injection is very similar yet the introduction of a –CH_2 spacer perturbs the wavefunction overlap between the chromophore and metal oxide surface, reducing electronic coupling.[168] Figure 3.12 shows the kinetics of BET (λ_{obs} = 400 nm) observed for RuP–SnO_2 and $RuCH_2P$–SnO_2 in pH 1 $HClO_4$, which are quite indistinguishable from each other; the tri-exponential rate constants obtained for $RuCH_2P$–SnO_2 are within the experimental error of those obtained for RuP–SnO_2 at both pH 1 and pH 5. Similar findings were previously reported for RuP–TiO_2 and $RuCH_2P$– TiO_2.[168]

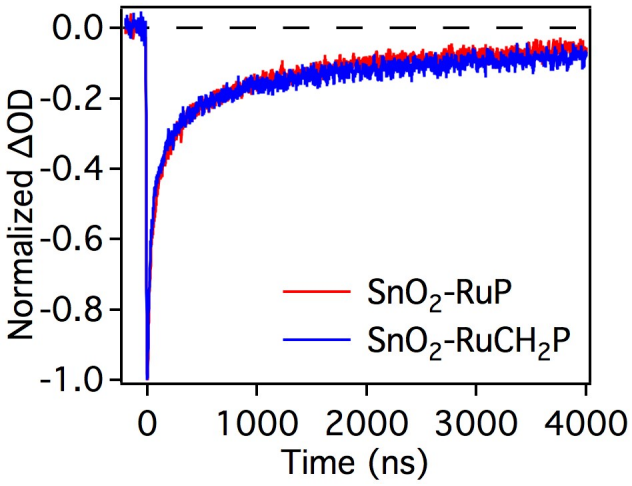

Figure 3.12: Transient absorption spectral changes of RuP–SnO_2 and $RuCH_2P$–SnO_2 monitored at 400 nm following 532 nm excitation (4mJ) in pH 1 aqueous $HClO_4$ solution.

3.3.6. Electrochemical Measurements

Cyclic voltammetry (CV) was performed on FTO electrodes coated with ~3.5 μm films of nanocrystalline SnO_2 and TiO_2 film to examine the change in distribution of sub-band gap trap states as a function of pH. Figure 3.13 shows the cyclic voltammograms of

bare, nanocrystalline SnO_2 and TiO_2 at various pH values. Current densities were estimated from the 2D active area of the metal oxide electrode, as experimental limitations prevented us from determining the exact surface area of the porous nanocrystalline thin films. As the conduction band potential and intra-band-gap states undergo a Nernstian shift with pH, the voltammogram window was adjusted –59 mV/pH unit.[93,181] Of note, the SnO_2 CVs in Figure 3.13B are measured in potential ranges positive of the H_2 evolution potential, and we do not see any contribution from H_2 evolution in the TiO_2 CVs.

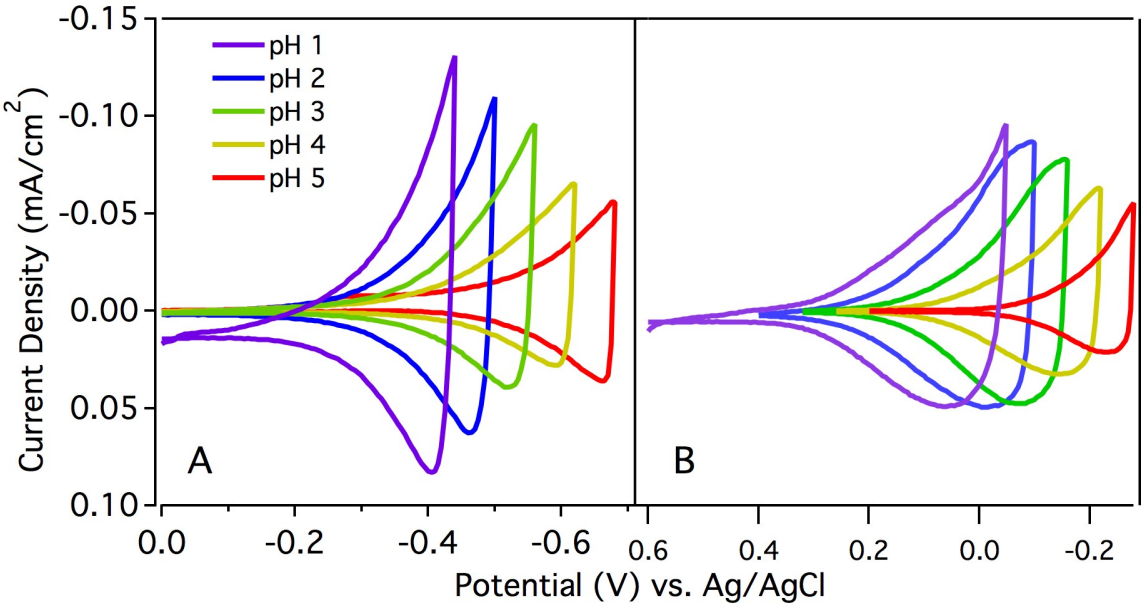

Figure 3.13: Cyclic voltammograms of **A)** TiO_2 and **B)** SnO_2 in various pH solutions of $HClO_4$ containing 0.1 M $NaClO_4$ as a supporting electrolyte. Scan rate: 20 mV/s. E°(Ag/AgCl) = 0.209 V vs. NHE. Current densities were estimated from the 2D active areas of the metal oxide electrodes.

In each cathodic scan, the current rises with a roughly exponential dependence on potential. A significant increase in cathodic current is also observed upon changing from pH 5 to pH 1. The same general trend is seen for TiO_2 (Figure 3.13A). This increase in current is attributed to an increased density of unoccupied trap states near the conduction band edge at low pH values.[170] It is worth noting that the shapes of the scans are more exponential for

TiO_2 than SnO_2. The difference in shape has been studied previously, with shape deviation from an exponential rise in current attributed to a lower capacitance.[182] A lower capacitance for SnO_2 suggests a lesser ability to efficiently store charge, possibly due to a lower density of unoccupied trap states. A monoenergetic peak at potentials positive of the exponential rise is observed for TiO_2 samples measured at high pH (Figure 3.14). Observation of this peak is very dependent on slide history. Others have also noted that this peak disappears as the film ages or after several voltammograms have been measured on a film.[182–184] A monoenergetic peak is not observed for any of the SnO_2 films studied here.

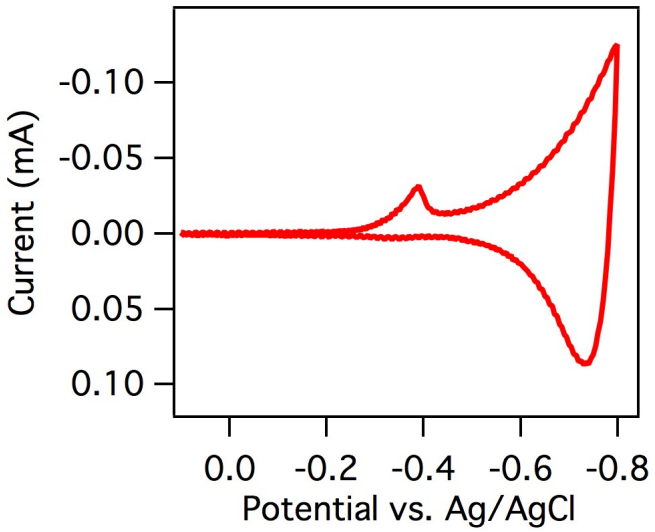

Figure 3.14: Cyclic voltammogram of TiO_2 in aqueous pH 7 solution with 100 mM $NaClO_4$. Scan rate 20 mV/s.

3.4. Discussion

3.4.1. Correlating Recombination Dynamics with Metal Oxide Trap State Densities

The goal of this study was to investigate the recombination dynamics of RuP–TiO_2 and RuP–SnO_2 systems and relate these dynamics to the intrinsic properties of the semiconductor employed. Luminescence quenching and transient absorption experiments

indicate efficient injection from photoexcited RuP into SnO_2 to form the charge separated state $Ru^{3+}P–SnO_2(e^-)$. Previous studies have shown similar results for RuP–TiO_2.[168,170] The excited state oxidation potential for RuP ($E°'(Ru^{3+/2+*})$ = –0.55 V vs. NHE) indicates the dye is sufficiently reducing to inject into the CB of TiO_2 (~ –0.1 V vs NHE at pH 1)[83,93,185] as well as SnO_2 whose conduction band is ~0.4 V positive of TiO_2.[83,107,108,186] The injection yields are similar for the two materials, though it has previously been shown that the ultrafast injection kinetics for related ruthenium chromophores are significantly faster for TiO_2 than SnO_2.[104,187,188] The difference has been attributed to the conduction band electronic structure; the density of states in the d-type TiO_2 conduction band being almost 2 orders of magnitude greater than that in the sp-type SnO_2 conduction band.[45,189]

The kinetics traces presented here show that BET occurs at a significantly faster rate in RuP–SnO_2 films as compared to RuP–TiO_2. Durrant and coworkers have reported qualitatively similar observations for related ruthenium-sensitized TiO_2 and SnO_2 films in acetonitrile solution, though in the non-aqueous study recombination rates were 2–3 orders of magnitude faster for SnO_2 than TiO_2 ($t_{1/2}$ = 800 μs (TiO_2) and 4 μs (SnO_2)).[100] By comparison, our results in aqueous conditions and at significantly higher irradiances indicate recombination is about 2–3 times faster for SnO_2. Differences between the solution and electrolyte identities, as well as injection yields, likely give rise to the disparity.

Details of the electronic structure, transport, and recombination mechanisms of TiO_2 and SnO_2 offer insight into differences in BET rates. While a full description of the density of unoccupied acceptor states (DOS) in nanocrystalline, anatase TiO_2 films remains elusive,[45] the model that has emerged from photochemical, electrochemical and spectroscopic experiments indicates that TiO_2 has an exponential distribution of intra-band-gap states

below the conduction band edge.[45,181,182,190] These bulk exponential trap states, often termed 'shallow trap states' or 'band-gap states,' have been attributed to defects, vacancies, adsorbed species and lattice alignment/mismatch which arise from high surface area and high density of particle/particle interfaces in the nanocrystalline material, though their origin is not completely understood. Like the conduction band, their redox energies exhibit a Nernstian shift with pH.[93,181] The energies and densities of the exponential distribution of intra-band-gap states for both TiO_2 and SnO_2 slides employed in this study were determined directly via cyclic voltammetry measurements (Figure 3.13).

Additionally, in reported electrochemical experiments, a capacitance peak is often observed for TiO_2 at an energy below the exponential distribution which is attributed to the reversible filling of a monoenergetic band-gap state.[184,190–193] Its position and the number of trapped electrons are both found to be pH dependent.[184,190,192] This characteristic peak in nanocrystalline electrodes is not seen in single-crystal electrodes. These observations together suggest that these monoenergetic traps are surface related and may arise from grain boundaries.[184,193] These trap states are often referred to as 'deep surface trap states.' In cyclic voltammograms measured as part of this work, a monoenergetic peak was observed for TiO_2 films only at pH values greater than 5 (Figure 3.14).

Electrons residing in trap states are localized, and thus charge transport through TiO_2 is believed to occur through thermal activation of trapped electrons to the CB or shallow trap states (a trapping/detrapping model) and/or a hopping mechanism whereby the electron moves directly between localized states.[194] Interfacial recombination is intimately related to the method of transport, as trapped electrons must be thermally activated to the conduction band or a shallow surface state by a detrapping mechanism in order to recombine with an

oxidized dye. As a result, recombination dynamics are highly nonexponential and dispersive.[45,100,173]

By comparison to TiO_2, details regarding the electronic structure, transport, and recombination mechanisms in SnO_2 offer insight to the enhanced rates of recombination. The ~400 mV positive shift in CB energy for SnO_2, as compared to TiO_2, decreases the driving force for recombination with the oxidized surface chromophore ($E°'$ ($Ru^{3+/2+}$)=1.33 V vs. NHE).[168] The faster recombination rates in SnO_2 are consistent with Marcus inverted region behavior, as has been seen in some driving force dependence studies where chromophore redox potentials are varied.[45,97,101,195] However, related experiments have shown contrary results where BET is independent of driving force[32,94,173] and coupling,[168] suggesting that recombination is rate-limited by electron transport within the metal oxide, not interfacial ET. These data, along with our observation of identical BET rates for both RuP–SnO_2 and $RuCH_2P$–SnO_2, inform us that the observed consistency with the Marcus inverted region kinetics is coincidental.

Like TiO_2, the conduction band of SnO_2 shifts –0.059 V per pH and an exponential distribution of trap states, as well as deep monoenergetic surface states, lie below the conduction band edge, though the density of states is significantly lower in SnO_2 (Figure 3.13).[100,196] The complex BET dynamics observed for sensitized SnO_2 by us and others[100,101] suggest the recombination mechanism from shallow trap states is qualitatively similar to that in TiO_2. However, the resting potentials measured for our films at pH 1 are 0.15 V and 0.25 V vs. Ag/AgCl (0.359 and 0.459 V vs. NHE) for SnO_2 and TiO_2, respectively, similar to measurements reported for related ruthenium-sensitized SnO_2 and TiO_2 films in acetonitrile.[100,197] As such, the electron density of RuP–SnO_2 is much higher (and the resting

potential much closer to the conduction band edge ~ +0.3 V vs NHE at pH 1) than in the corresponding TiO_2 system (conduction band edge ~ –0.1 V vs. NHE at pH 1), as illustrated in Figure 3.15. Several recent reports have shown that progressive filling of TiO_2 and SnO_2 exponential trap states via applied bias results in increased electron mobility and faster recombination dynamics, underscoring the intricate relationship of electron density, electron mobility and recombination rates.[100,170,198] Our observed recombination kinetics and the reported electron mobility for SnO_2 (which is 2-3 orders of magnitude greater than that of TiO_2)[104–106] are consistent with these measurements. Given identical injection yields for RuP–SnO_2 and RuP–TiO_2, the comparatively higher resting potential of SnO_2 suggests the injected electrons in SnO_2 occupy and are more concentrated in very shallow trap states, while the injected electrons in TiO_2 are distributed among the many empty, available trap states throughout the exponential tail of intra-band-gap localized states, as well as deep surface states. As a result, injected electrons in SnO_2 have low activation energies for thermal detrapping to the conduction band or shallow surface trap states, which leads to rapid BET and high mobility.

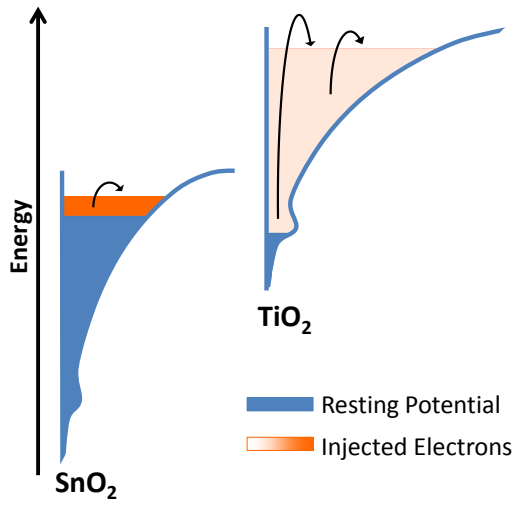

Figure 3.15: Comparison of the trap state distribution and resting potentials of SnO_2 and TiO_2. The orange shading indicates the concentration of injected electrons that occupy these trap states, with darker orange corresponding to higher concentrations.

While the dispersive recombination kinetics observed in both TiO_2 and SnO_2 indicate related mechanisms of recombination, recent reports from Hupp[47] and Meng[196] suggest a second recombination pathways may be present in sensitized SnO_2—electrons trapped in reactive, low-energy surface states may recombine directly with photosensitizers. These surface states—which are thought to arise from incomplete or incorrect coordination of Sn(IV) sites or dangling bonds on the nanoparticle surface[199]—can be passivated by a thin layer of Al_2O_3[47] or TiO_2[196] to yield devices with improved performance. While deep, surface trap states also exist for TiO_2, it has been suggested they are not reactive enough to provide a pathway for recombination.[26,47] Our results are consistent with this model; electrons trapped in deep surface states of TiO_2 have high activation barriers to thermal detrapping or must tunnel and these mechanisms are likely responsible for the large slow time component (ΔA_{slow}) observed.[200,201] Complete recombination occurs on the millisecond timescale for RuP–TiO_2. While we did not observe deep, surface trap states for SnO_2 directly in our cyclic

voltammograms (and found no electrochemical observations in the literature) and these states would likely be filled in the dark resting state, they could offer a second pathway for rapid BET based on the reports above. Indeed, recombination is complete within hundreds of microseconds for RuP–SnO_2 (Figure 3.9). This slow time component is critical in DSPEC applications where additional electron transfer process occur after electron injection into the metal oxide.

In summary, the differences in recombination dynamics observed for photoexcited chromophore-derivatized TiO_2 and SnO_2 nanocrystalline films arise from the precise identity, energetic distribution, and density of both shallow and surface trap states, as well as the recombination pathways available from these states.

3.4.2 pH Dependence of Recombination Kinetics

BET kinetics for RuP–SnO_2 at constant pulse energy show an increase in recombination rates at lower pH values. The trend is similar to the pH dependence previously reported for RuP–TiO_2, though less significant.[170] In other related chromophore–metal oxide systems, the pH dependence of recombination dynamics has been studied with conflicting results, with evidence for both pH dependence and non-dependence reported.[99,180,202,203] Many factors can give rise to an observed pH dependence in these systems. Importantly, in these and related experiments, the injection yield for RuP–TiO_2 decreases from 1.0 at pH 1 to 0.7 at pH 5 at pulse energies of 4 mJ.[110,170] Since the BET dynamics are dependent on the number of injected electrons, direct comparisons at different pH values are not straightforward under these conditions. Furthermore, it has been noted that certain fitting methods, including sums of exponentials, are more sensitive to the initial concentration of charge separated species than other methods which utilize second order kinetics.[94] Thus we

turned to variable irradiance experiments wherein decreased pulse energies were used to offset the increased injection yields at lower pH values. Under these conditions, the same concentration of charge-separated species was obtained at pH 1, 3, and 5 at our earliest observation time (10 ns; however an ultrafast time component for back electron transfer has been reported[204]). Under these variable irradiance conditions, the effects of pH can be isolated from injection yield and the pH dependence can be related solely to differences in the semiconductor electronic structure under the variable conditions**.** As seen in Figure 3.11, a pH dependence is still observed for the BET dynamics of RuP–TiO_2 when injection yields are equal, while BET dynamics of RuP–SnO_2 are nearly pH independent under the same conditions.

As noted above, the conduction bands of both TiO_2 and SnO_2 display a Nernstian dependence on pH, with the CB edge shifting –59 mV per pH unit.[93] As faster recombination rates are observed at lower pH, the differences are consistent with Marcus inverted region kinetics. However, as discussed above, this explanation does not correlate with the rate-limiting transport via detrapping and/or hopping mechanisms which are widely accepted for describing back electron transfer in these systems.

We suggest that the pH dependence of the back electron transfer rates arises from pH-specific identity and distribution of metal oxides trap states. As discussed above there are both shallow trap states as well as deep surface states in TiO_2, and the number, energies and identity of these states vary with pH. Meyer and coworkers have suggested that faster back electron transfer rates for RuP–TiO_2 at lower pH values are due to increased occupation of shallow trap sites.[170] Our electrochemical measurements support the notion that the number of shallow trap states available in TiO_2 (and SnO_2) increases at lower pH values (Figure

3.13). A microscopic explanation for the pH dependence of trap states density and identity is the focus of current investigations. Upon photoexcitation, electrons are injected into the conduction band of the metal oxide and are quickly trapped at these sub band gap localized states. The initial probability of the injected electron occupying any localized trap state likely mirrors the exponential distribution of these states, as the energetic distribution of intra-band-gap states reflects an ensemble measurement for a nanocrystalline film, not a single nanoparticle. Under the assumption of rate-limited trap site diffusion, relaxation to the lower energy trap states is slow as electron mobility in TiO_2 is relatively low.[105] BET, which proceeds through similar mechanisms, competes with relaxation of trapped electrons. As such, at low pH, the increased availability of shallow trap states means more electrons are localized near the conduction band or shallow, reactive surface states where they have low activation energies for BET (Figure 3.16).

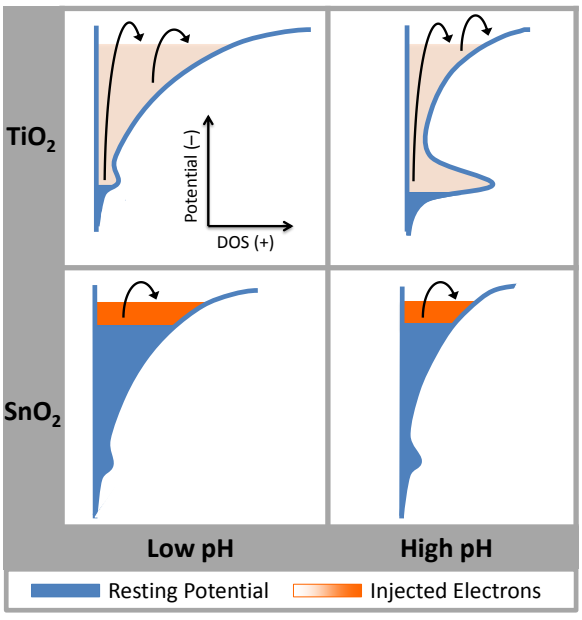

Figure 3.16: Schematic comparing of the distribution of trap states and available recombination pathways for RuP–SnO_2 and RuP–TiO_2 at low and high pH values. The orange shading indicates the concentration of injected electrons that occupy these trap states, with darker orange corresponding to higher concentrations.

This pH dependence of shallow trap states is consistent with the pH dependent recombination rates observed for RuP–TiO_2. The higher resting potential of SnO_2 can explain the near pH independence observed for RuP–SnO_2. Because the resting potential is so close to the conduction band edge for SnO_2, deeper exponential trap states as well as surface states are filled in the 'dark' resting state. This means that injected electrons are concentrated in the shallow trap states near the band gap edge. Although our electrochemical measurements of SnO_2 indicate the number of shallow trap states also increases at low pH values, the overall density of these trap states is significantly lower than TiO_2 and only a subtle pH dependence is observed.[104,107,187] These results are consistent with the observation that in aqueous conditions, BET for RuP–TiO_2 films accelerates upon application of a negative bias as trap states are filled and injected electrons are relegated to trap states nearer the conduction band.[170]

Deep surface states also influence recombination kinetics. The low resting potential of TiO_2 suggests some of these localized trap states are empty in the 'dark' resting state, and a percentage of injected electrons will occupy these low energy states. As noted above, the high activation barriers for thermal detrapping, or alternatively a tunneling pathway, from these deep surface states corresponds to the slow time component of the BET kinetics. Lindquist has shown that the number of these deep surface states in TiO_2 increases with increasing pH, which is consistent with our electrochemical observations and correlates with the larger ΔA_{slow} values observed at higher pH.[192]

By contrast, recombination from highly reactive, low-energy surface states in SnO_2 may proceed via direct and rapid recombination with the oxidized chromophore, as discussed above.[47,196] Little has been reported about the pH dependency of these surface states, and we

were unable to probe them directly in our electrochemical measurements. However, these low energy states may be filled under 'dark' resting conditions and are thus not occupied by injected electrons. Nevertheless, the presence of this rapid, direct recombination pathway minimizes the need for surface trapped electrons to recombine via high activation barrier pathways. As such, recombination kinetics in RuP–SnO_2 contain only a small, pH independent ΔA_{slow} component which unlike TiO_2, does not correspond to detrapping from deep surface states.

In summary, the pH dependence of BET dynamics observed for RuP–TiO_2 and pH independence observed for RuP–SnO_2 correlate with the pH dependence of the metal oxide trap states, as well as the mechanism of recombination from these states.

3.5. Conclusion

We have demonstrated that the interfacial charge recombination dynamics of RuP–SnO_2 and RuP–TiO_2 in aqueous conditions correlate with the electronic structure of the nanocrystalline metal oxide films. Back electron transfer in RuP–SnO_2 is 2–3 times faster than RuP–TiO_2, qualitatively consistent with previous reports of related systems in non-aqueous conditions.[100] The rapid recombination kinetics in RuP–SnO_2 are consistent with the reported high electron mobility and fast transport dynamics of SnO_2, all of which are based on thermally activated electron trapping/detrapping dynamics. Rates of charge recombination are also pH dependent in RuP–TiO_2 systems, with BET kinetics accelerating as the pH is lowered. Conversely, rates of charge recombination in RuP-SnO_2 systems are nearly pH independent. We suggest that the observed pH effects in RuP–TiO_2 are correlated with the pH dependent trap state identity and distribution within the metal oxide nanoparticle

matrices. While the trap state identity and distribution of SnO_2 is also pH dependent, the comparatively high resting potential accounts for the nearly pH independent behavior observed for RuP–SnO_2 systems. Ultimately, while SnO_2 is an attractive semiconductor material for DSPECs due to its low conduction band energy, the intrinsic electronic structure promotes rapid interfacial charge recombination kinetics which could be detrimental to device performance.

CHAPTER 4. Photophysical Characterization of Porphyrin and Porphyrin-Ru(II) Polypyridal Chromophore-Catalyst Assemblies on Mesoporous Metal Oxides

Reproduced from Nayak, A.; Knauf, R. R.; Hanson, K.; Alibabaei, L.; Concepcion, J. J.; Ashford, D. L.; Dempsey, J. L.; Meyer, T. J. Synthesis and photophysical characterization of porphyrin and porphyrin–Ru(II) polypyridyl chromophore–catalyst assemblies on mesoporous metal oxides. *Chem. Sci.*, **2014**, *5*, 3115 with permission from The Royal Society of Chemistry.

4.1. Introduction

Dye-sensitized solar cells and photoelectrosynthesis cells provide viable strategies for solar-to-electricity or solar-to-fuel conversion, respectively.[20,205] Central in both is excitation and injection by surface-bound chromophores or chromophore–catalyst assemblies on mesoporous, nanoparticle metal oxide surfaces. The use of organic chromophores is appealing given their potentially low cost, high light absorptivities, and the ability to modify them systematically by chemical synthesis. In terms of spectral coverage and excited and ground state redox potentials, porphyrins, with high molar absorptivities in the visible spectrum, are advantageous.[206–208] They have been used routinely in DSSC applications but there are few examples in DSPECs.[209–214]

In DSPEC applications, the heart of the device is a chromophore–catalyst assembly which absorbs light and undergoes excited-state electron or hole injection followed by electron transfer activation of the catalyst. We describe here the photophysical properties of a high-potential, electron deficient porphyrin with phosphonate anchors. It is used to prepare chromophore–catalyst assemblies on nanostructured, mesoporous metal oxides by a layer-by-layer approach pioneered earlier for polypyridyl complexes of ruthenium.[215–217] Transient

spectroscopic measurements provide direct evidence for excited-state electron injection from the SnO_2-bound porphyrin; in the chromophore–catalyst assembly, oxidation of the catalyst via intra-assembly electron transfer follows.

4.2. Experimental

4.2.1. Materials

All reagents and solvents were obtained from either Sigma Aldrich or Fisher Scientific and used without any purification. Inert atmosphere manipulations were carried out under argon prepurified by passage through a drying tower (Linde 3-Å molecular sieves). Deuterated solvents $CDCl_3$ and CD_3OD for NMR were obtained from Cambridge Isotope Laboratories Inc. Nano-TiO_2, ZrO_2 and SnO_2 films on top of FTO (fluorine doped tin-oxide) coated glass were prepared according to previously published methods.[1-3] Porphyrin

4.2.2. Chromophore and Catalyst Synthesis

5,15-Bis[4-(dihydroxyphosphoryl)phenyl]-10,20-bis(pentafluorophenyl)porphyrin **(1)**, Ru(2,6-bis(1-methylbenzimidazol-2-yl)pyridine)(4,4'-CH_2 PO_3H_2bpy)-$(OH_2)^{2+}$ **(2)**, Zinc(II)-5,15-bis[4-(Dihydroxyphosphoryl)phenyl]-10,20-bis(pentafluoropehenyl)porphyrin **(3)**, 5,15-Bis[4-(diethoxyphosphoryl)phenyl]-10,20-bis(pentafluoropehenyl)porphyrin **(4)**, and Zinc(II)-5,15-bis[4-(Diethoxyphosphoryl)phenyl]-10,20-bis(pentafluoropehenyl)porphyrin **(5)** were synthesized via literature procedures.[28,218]

4.2.3. Transient Absorption Spectroscopy

Nanosecond to microsecond transient absorption experiments were performed using a commercially available laser flash photolysis system (Edinburgh Instruments, Inc., model LP920). Laser excitation (425 nm, 5-7 ns FWHM, 3.8 ± 0.1 mJ/pulse, 15mJ/cm^2 unless

stated otherwise) was provided by a pulsed Nd:YAG laser (Spectra-Physics, Inc., model Quanta-Ray LAB-170-10) / OPO (VersaScan-MB) combination. To accommodate the pulsed, 1 Hz intensification of the 450 W Xe probe source of the LP920, the laser system was set such that the flashlamps were fired at 10 Hz yet Q-switched at 1 Hz. Timing of the experiment, including laser and probe pulsing, as well as data collection was computer controlled via Edinburgh software (L900) with the aid of a Tektronix oscilloscope (model TDS-3032C). The LP920 white light probe output was passed through a 380 nm long pass color filter before passing through the sample to minimize band gap excitation of SnO_2. The LP920 was equipped with a multi-grating detection monochromator outfitted with a Hamamatsu R928 photomultiplier tube (PMT) in a non-cooled housing and a gated CCD (Princeton Instruments, PI-MAX3) such that detection was software selectable. The gated CCD was used for recording transient spectra of SnO_2–**3** and ZrO_2–**3** covering the visible region (400-850 nm, 3 nm spectral bandwidth) at a given time after excitation (10 ns gatewidth). Data were the result of averaging 100-200 laser shots. The transient spectral data for complex SnO_2–**1**, ZrO_2–**1,** SnO_2–**1**–Zr–**2** and ZrO_2–**1**–Zr–**2** were generated from kinetic traces measured with the PMT. Kinetics were taken every 5–10 nm, and were the result of averaging 30–50 laser shots. Spectral data were analyzed using Igor Pro (WaveMetrics Inc.) software. Data were collected at room temperature (295 ± 3 K). Derivatized MO_x films were inserted diagonally into a 10 mm path length quartz cuvette whose top had been adapted with a #15 o-ring sealing joint, sidearm, and Kontes valve. After addition of solvent (0.1 M $LiClO_4$ in acetonitrile or aqueous 0.1 M $HClO_4$) to the cuvette, the sample was sparged with argon for at least 45 minutes immediately prior to experiments.

4.2.4. Steady-State Emission

Emission data were collected at room temperature using an Edinburgh FLS920 spectrometer with luminescence first passing through a 450 nm long-pass color filter, then a single grating (1800 l/mm, 500 nm blaze) Czerny-Turner monochromator (10 nm bandwidth) and finally detected by a peltier-cooled Hamamatsu R2658P photomultiplier tube. Samples were excited at 425 nm using light output from a housed 450 W Xe lamp / single grating (1800 l/mm, 250 nm blaze) Czerny-Turner monochromator combination with 10 nm bandwidth and a 375 nm long pass filter to avoid direct excitation of the metal oxide.

4.2.5. Time Resolved Emission

Time resolved emission dynamics were monitored using the FLS920's time-correlated single-photon counting capability (1024 channels; 1 ns per channel) with each data set collecting a set number of counts. Excitation was provided by an Edinburgh EPL-445 picosecond pulsed diode laser (444.2 nm, 80 ps FWHM) operated at 20 MHz. . Derivatized metal oxide samples were placed in a two piece cuvette and argon degassed as described for the TA measurements.

4.2.6. Spectroelectrochemistry

Spectroelectrochemistry was carried out in in CH_3CN (0.1 M [^{n}Bu$_4$N][PF_6]) using a honeycomb cell and Ag/AgCl nonaqueous reference electrode. Ferrocene was then used as an internal standard ($E°'$ ($Fc^{+/0}$) = + 630mV vs. NHE).[4] Inert atmosphere was maintained by performing experiments in a nitrogen-filled glovebox. Linear staircase voltammetry was used, with a 2 minute hold time and 100 mV step size. Absorbance spectra were measured at each step. The data are reported as a difference spectra of the absorbance at the specified potential minus the absorbance without a potential applied.

4.2.7. Cyclic Voltammetry

Cyclic voltammetry of compounds **4** and **5** in solution was performed in CH_2Cl_2 (0.1 M [$^nBu_4N$][PF_6]) using a 3-cell set up with a glassy carbon as working, nonaqueous $Ag/AgNO_3$ as reference and a Pt wire as counter electrode. Inert atmosphere was maintained by purging argon through the solution for 2 minutes before scans. Ferrocene was used as an internal standard ($E°'$ ($Fc^{+/0}$) = + 690 mV vs. NHE).

4.2.8. X-ray Photoelectron Spectroscopy (XPS)

XPS data was taken on a Kratos Axis Ultra DLD system equipped with a monochromatic Al Ka x-ray source. The XPS chamber had a base pressure of ca. 5 $x10^{-9}$ torr and a pass energy of 20 eV was used for all high resolution scans.

4.3. Results and Discussion

Porphyrin derivatives used in this study, **1** and **3**, are shown in Figure 4.1. They have *meso* positions substituted with pentafluorophenyl groups and 4-phosphonated phenyl groups for surface binding and assembly formation. Pentafluorophenyl substituents were added to the porphyrin to shift the potential for the $porphyrin^{+/0}$ couple sufficiently positive to drive water oxidation catalysis. The porphyrin was synthesized from 5-pentafluorophenyldipyrrylmethane and 4-(diethoxyphosphoryl)benzaldehyde by an acid-catalyzed condensation reaction. Synthesis and characterization of the water oxidation catalyst **2** was previously reported.[218]

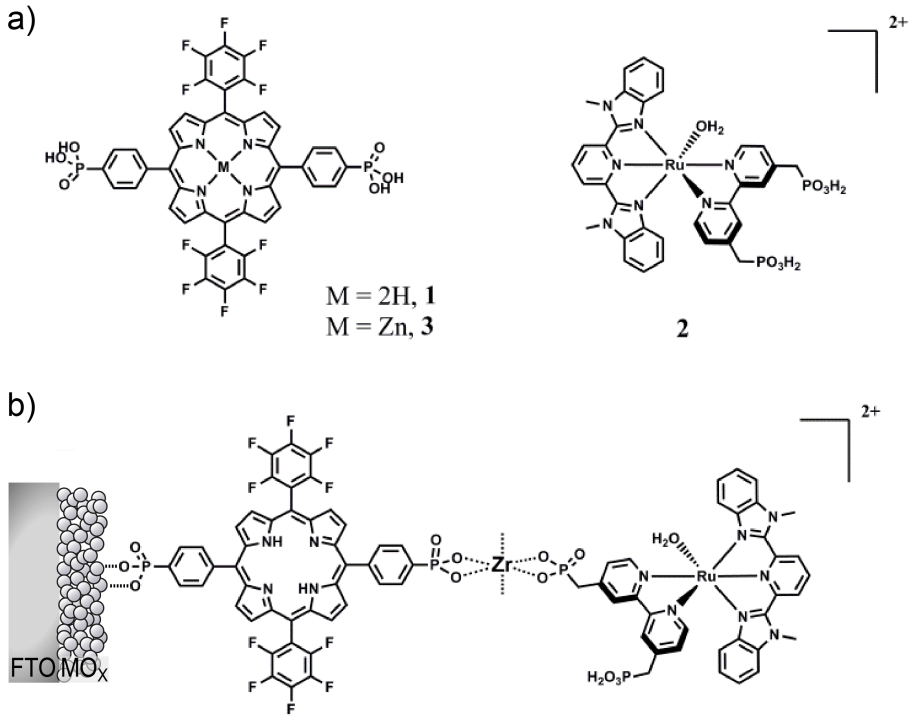

Figure 4.1 A) Structures of porphyrin chromophores (**1** and **3**) and ruthenium water oxidation catalyst (**2**). **B)** The layer-by-layer chromophore-catalyst assembly MO_2–**1**–Zr–**2**.

Cyclic voltammetry of the free base porphyrin phosphonate ester **4** (Figure 4.2A) exhibits reversible oxidation waves at $E_{1/2}(P^+/P)$ = 1.58 V and $E_{1/2}(P^{2+}/P^+)$ = 1.79 V vs NHE in CH_2Cl_2. For the Zn(II) porphyrin phosphonate ester **5**, a reversible oxidation wave appears at $E_{1/2}(P^+/P)$ = 1.31 V vs NHE (Figure 4.2B).

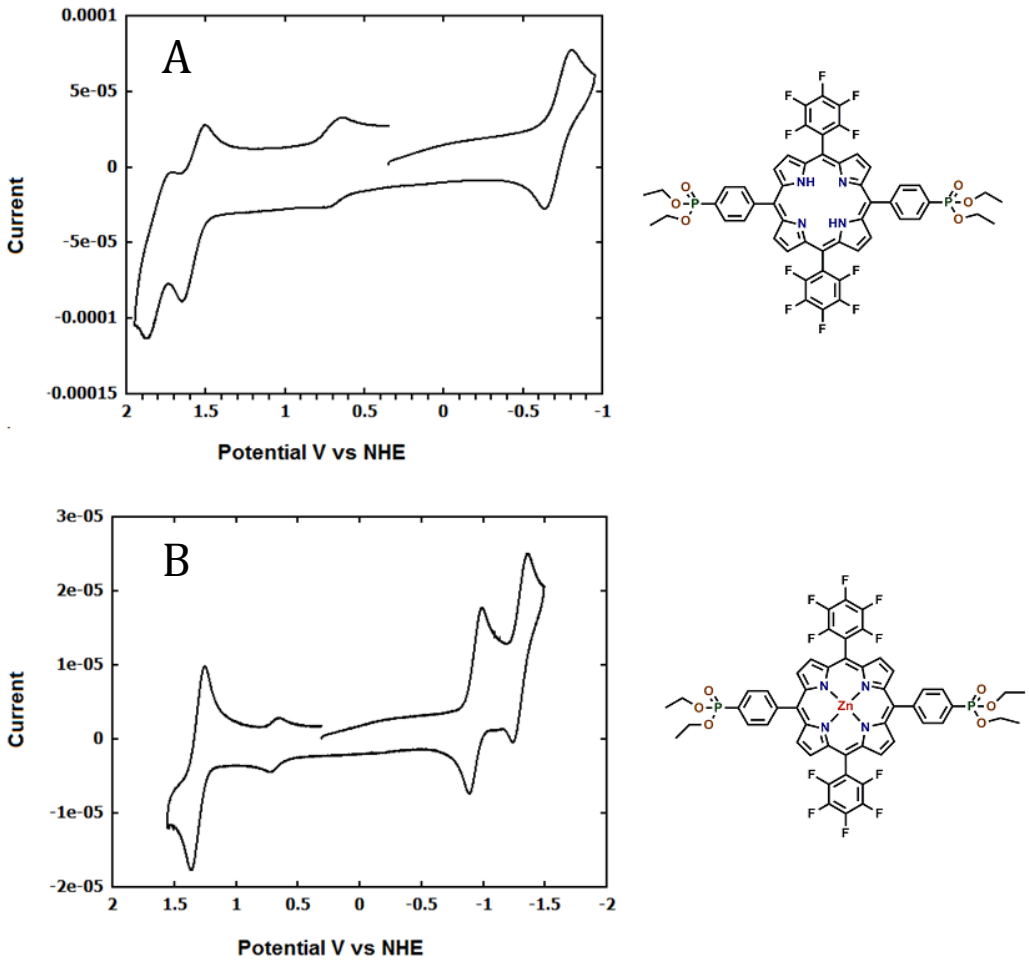

Figure 4.2: A) Cyclic voltametry of free base **4** and **B)** Zn-porphyrin **5** in 0.1 M [^{n}Bu$_4$N][PF$_6$] in CH_2Cl_2. Scan rate = 100 mV/second. Ferrocene was used as an internal standard ($E^{\circ\prime}$ ($Fc^{+/0}$) = + 690 mV vs. NHE).

Porphyrin loaded mesoporous, nanoparticle TiO_2, SnO_2 and ZrO_2 films (*nano*MO_2, ~7 μm thick) on FTO coated glass substrates were prepared by soaking in a 1.2 mM solution of **1** or **3** in 1:1 (Volume:Volume) CH_2Cl_2/Methanol. Binding of the porphyrin on metal oxide surface was monitored by absorbance measurements with full surface coverage reached within 1 hour of soaking (Figure 4.3) The adsorption isotherm is shown in Figure 4.4, with a surface coverage of 6.3×10^{-8} mole cm^{-2} reached, comparable to typical phosphonated Ru(II)-popypyridyl chromophores.[219]

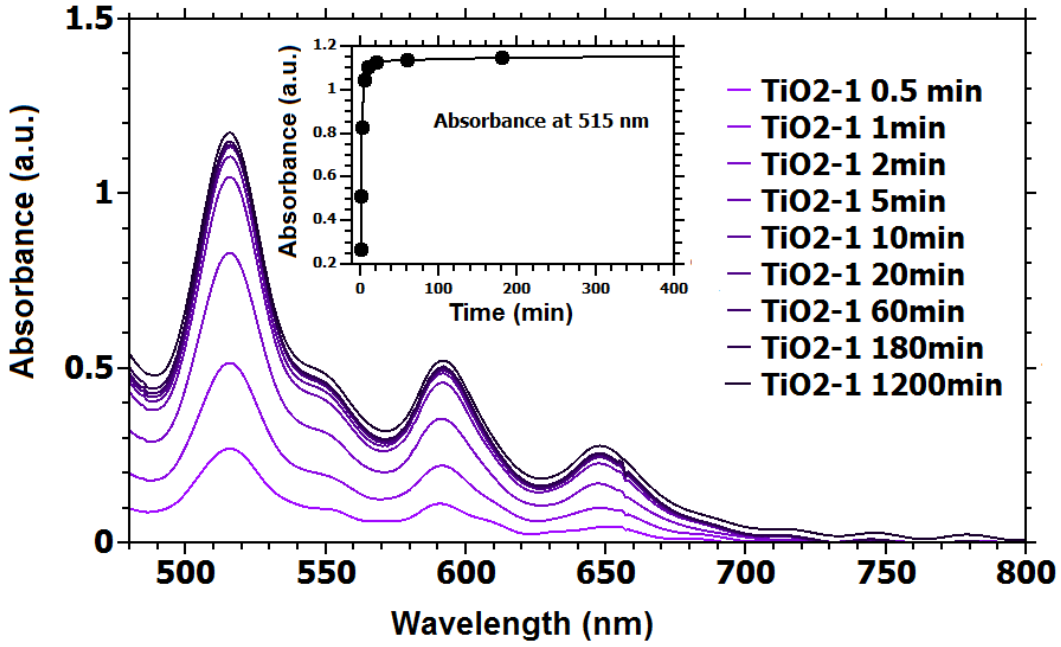

Figure 4.3: Loading of TiO_2–**1** (~7 μm thick nanocrystalline TiO_2 film) from a 1.2 mM solution of **1** in CH_2Cl_2/methanol (1:1) as a function of time.

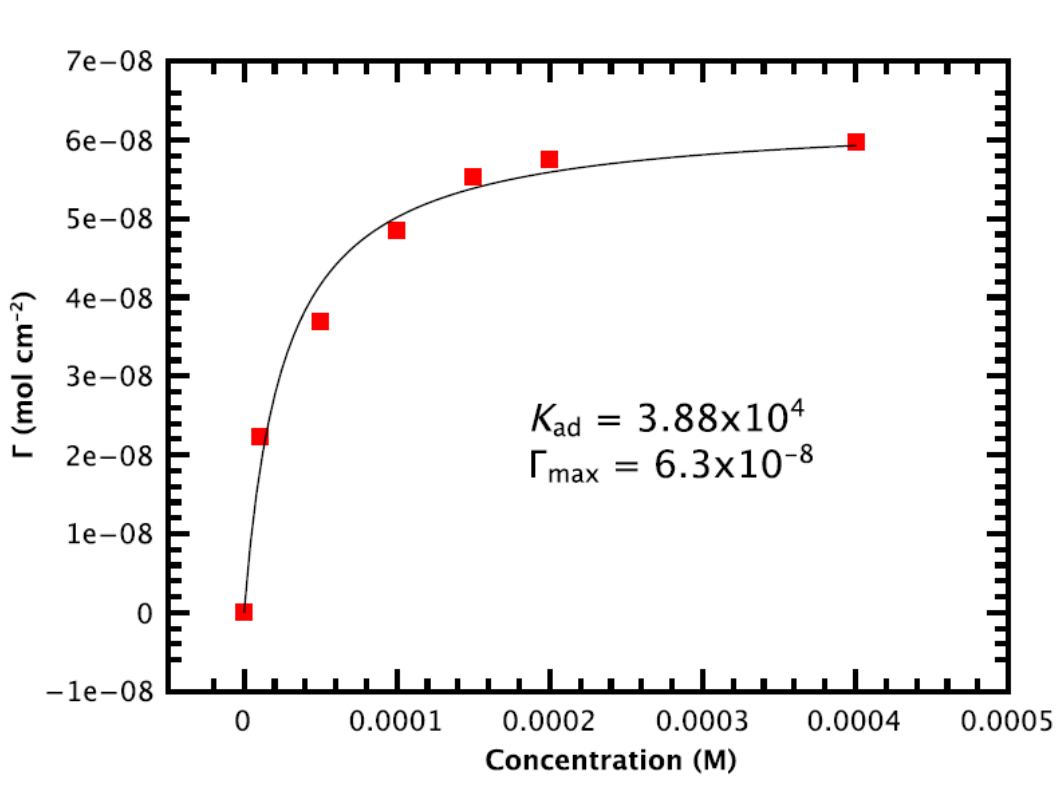

Figure 4.4: Adsorption isotherm of TiO_2–**1** in CH_2Cl_2/methanol (1:1).

Excited-state properties for both **1** and **3** were evaluated on *nano*ZrO_2. Because of its relatively high conduction band potential (~ –1.5 V vs NHE), excited-state injection does not occur into ZrO_2, allowing the excited state properties of the surface-bound porphyrins to be evaluated. ZrO_2–**1** fluoresces with vibronic components at 654 nm (1.89 eV) and 714 nm (1.73 eV) and ZrO_2–**3** at 607 (2.04 eV) nm and 658 nm (1.88 eV) in CH_3CN at room temperature (Figure 4.5). From the intersection of the normalized absorption and emission spectra for porphyrin phosphonate esters **4** and **5** in solution (Figure 4.6), E_{00} values for the emitting excited states were estimated to be 1.9 eV for **1** and 2.1 eV for **3**. Based on these values and the $E_{1/2}(P^+/P)$ values discussed above, singlet excited-state reduction potentials were estimated to be $E^{o\prime}_{(1^+/1^*)} = -0.32$ V and $E^{o\prime}_{(3^+/3^*)} = -0.79$ V vs NHE. (Figure 4.7)

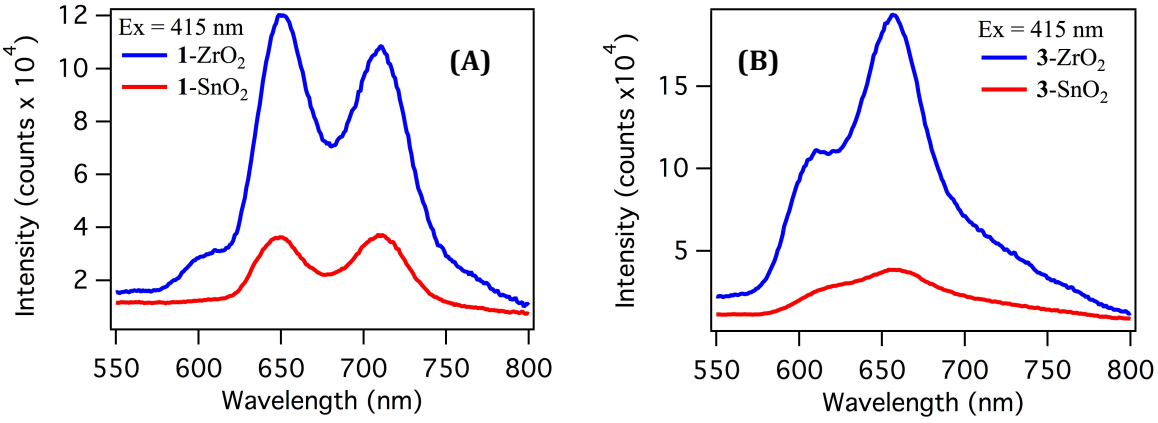

Figure 4.5: Comparison of emission quenching of **1** and **3** loaded on SnO_2 and ZrO_2 in CH_3CN (0.1 M $LiClO_4$).

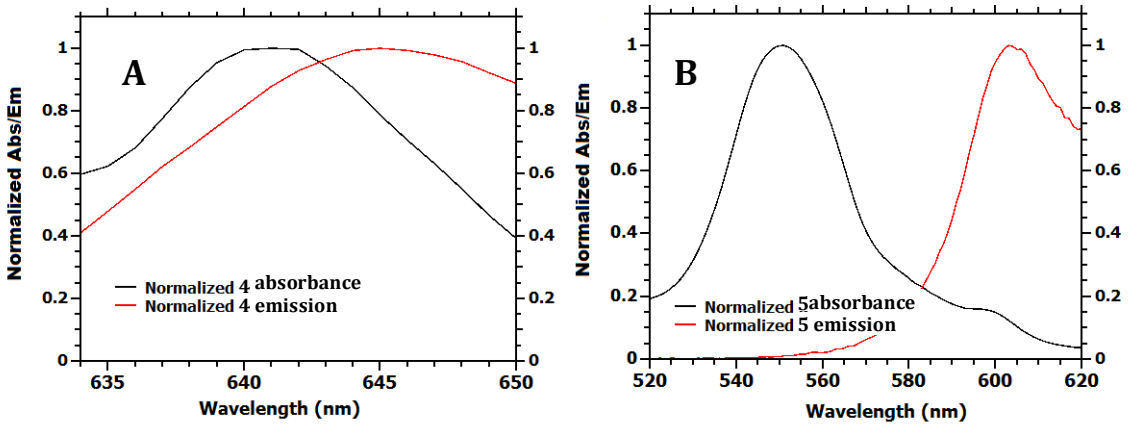

Figure 4.6: **A)** Cross sections of normalized absorption and emission for **4** and **B) 5**

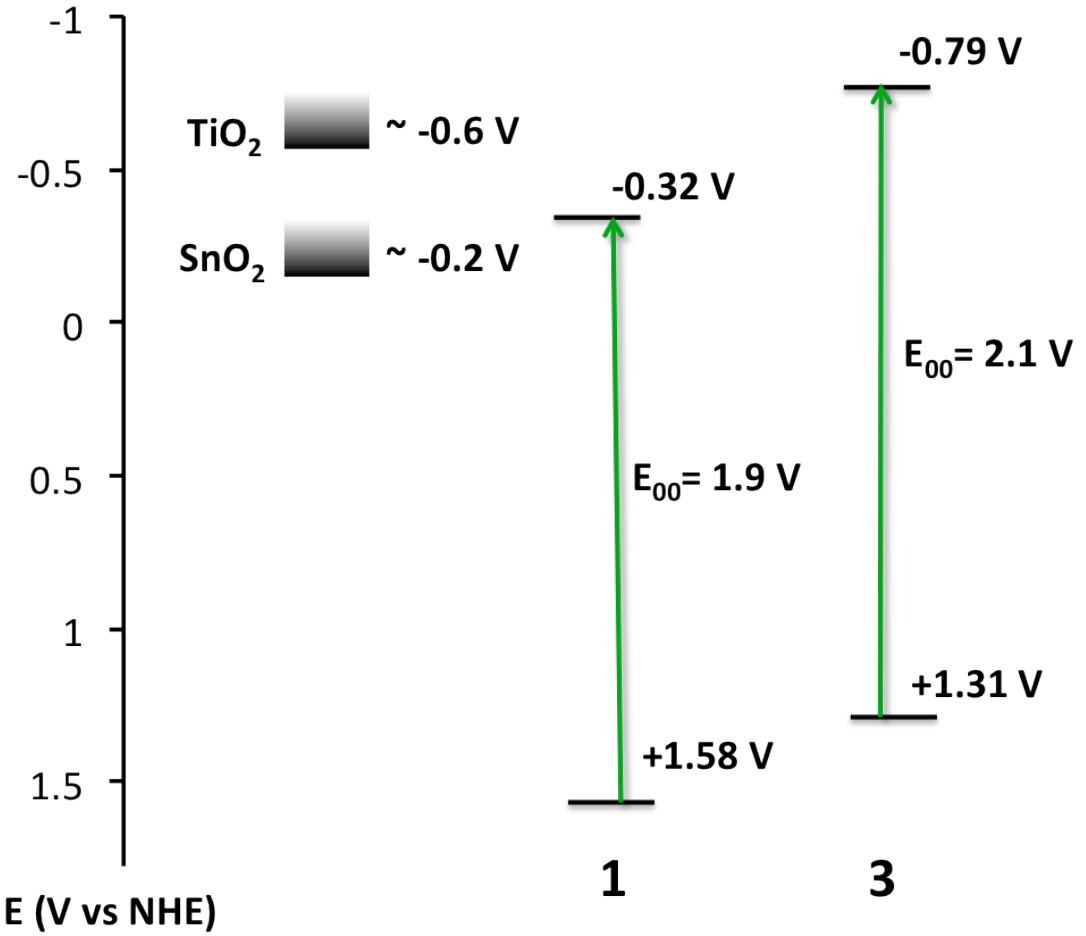

Figure 4.7: Ground and excited–state energy levels of **1** and **3** with comparison to the conduction bands of TiO_2 and SnO_2 at pH 7.[220]

When bound to *nano*TiO_2, fluorescence from **3** is quenched substantially (~80%) relative to ZrO_2–**3** (Figure 4.8). This is in contrast to TiO_2–**1**, for which negligible quenching was observed. These observations are qualitatively consistent with the lower excited-state potential for the free base porphyrin **1**. However, when bound to SnO_2, in which E_{cb} is ~0.4 V more positive than E_{cb} for TiO_2,[221] substantial emission quenching was observed for both SnO_2–**1** and SnO_2–**3** (Figure 4.5), consistent with electron injection into SnO_2 from the porphyrin excited state(s).

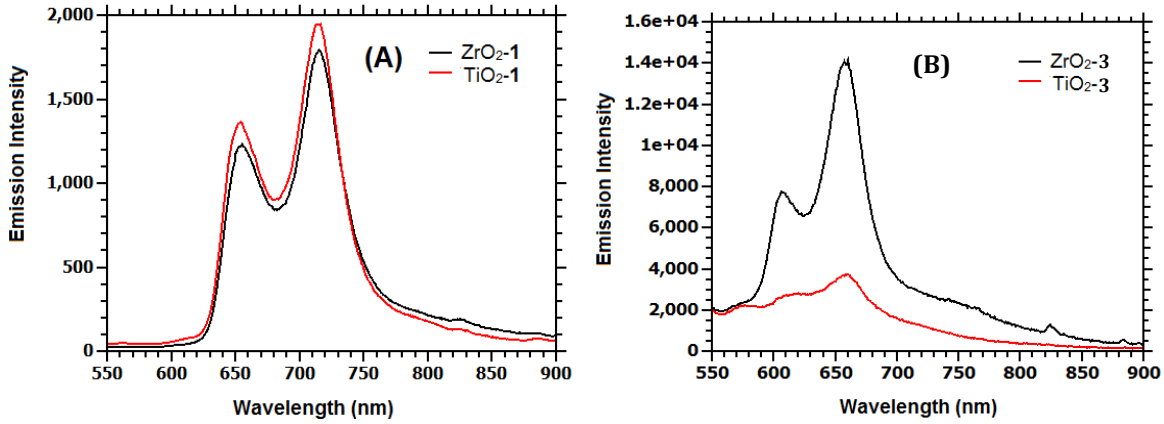

Figure 4.8: Comparison of emission quenching **1** and **3** loaded on TiO_2 and ZrO_2 in CH_3CN (0.1 M $LiClO_4$).

Transient absorption difference spectra for SnO_2–**3** at various delay intervals following 425 nm excitation in CH_3CN, (Figure 4.9A) revealed three principal features. At the earliest observation time (25 ns), a new absorption feature at λ_{max} = 464 nm, a bleach from loss of the ground state Q-band absorption at 555 nm, and a broad absorption feature from 600–750 nm appear. These new spectral features, which decay with $t_{1/2}$ ~ 2 μs, closely match those of the radical cation $\mathbf{5}^{\bullet+}$ (Figure 4.9B), consistent with excitation and injection (Equation 4.1a). They are noticeably different from spectral changes observed for ZrO_2–**3** following 425 nm excitation (Figure 4.9C). In the transient spectrum for ZrO_2–**3**, an intense

feature appears at λ_{max} = 467 nm, characteristic of the porphyrin triplet excited state which decays with $t_{1/2}$ ~ 40 μs. No transient absorption features were observed from 600–750 nm. When combined with the results of the luminescence quenching measurements, there is clear evidence for efficient electron injection by $\mathbf{3}^*$ into SnO_2 to form the surface redox-separated state $SnO_2(e^-)$–$\mathbf{3}^+$ followed by back electron transfer (Equation 4.1b).[222] Because of the similarities of the porphyrin cation and triplet absorptions near 465 nm, we cannot definitively rule out a contribution from the triplet state absorption in the SnO_2–**3** spectrum. On ZrO_2, initial excitation to give the singlet is followed by rapid intersystem crossing and decay of the triplet excited state (Equation 4.2).

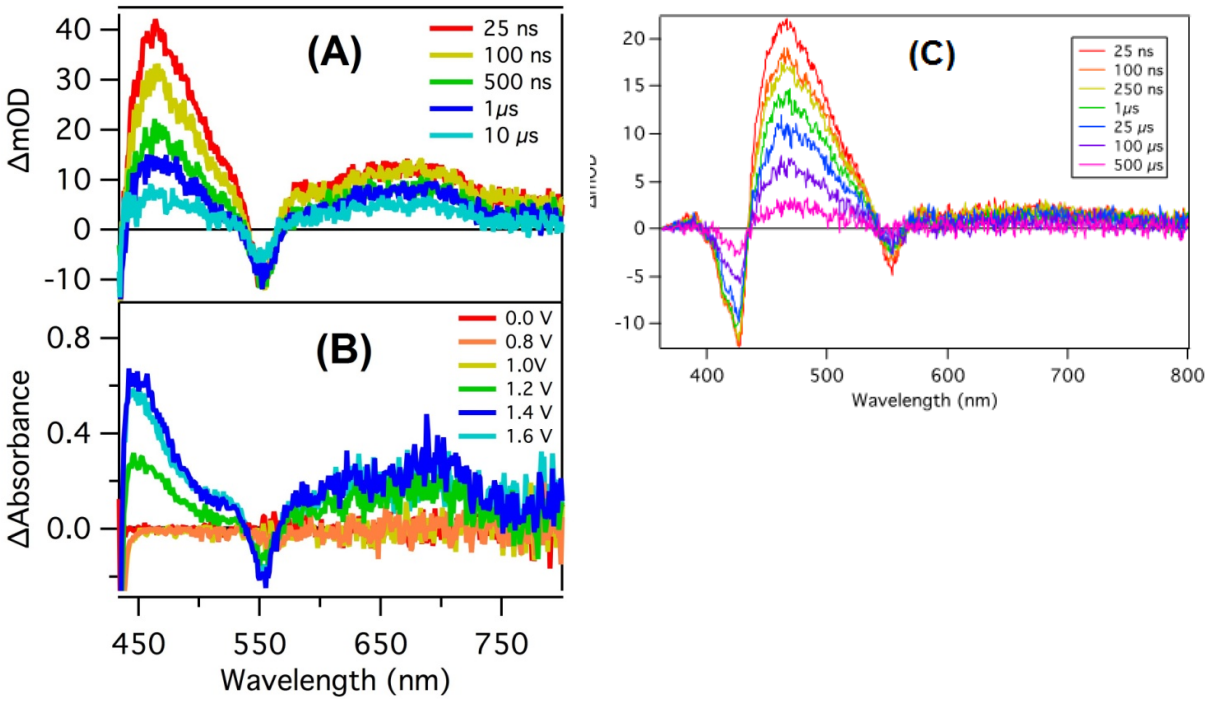

Figure 4.9: A) Time dependent transient absorption difference spectra for SnO_2–**3** following 425 nm excitation in CH_3CN (0.1 M $LiClO_4$). **B)** P^+–P absorption difference spectra for **5** in in MeCN (0.1 M [^{n}Bu$_4$N][PF_6]) as a function of applied potential as determined via a spectroelectrochemical titration. Potentials referenced vs. Ag/AgCl. **C)** Time dependent transient absorption difference spectra for ZrO_2–**3** in CH_3CN (0.1 M $LiClO_4$) after excitation at 425nm.

$$SnO_2\text{-}P \xrightarrow{h\nu} SnO_2\text{-}^1(P^*) \rightarrow SnO_2(e^-)\text{-}P^+ \quad (4.1a)$$

$$SnO_2(e^-)\text{-}P^+ \rightarrow SnO_2\text{-}P \quad (4.1b)$$

$$ZrO_2\text{-}P \xrightarrow{h\nu} ZrO_2\text{-}^1(P^*) \rightarrow ZrO_2\text{-}^3(P^*) \quad (4.2)$$

Transient absorption difference spectra for SnO_2–**1** following 425nm excitation in CH_3CN are shown in Figure 4.10A. The spectra are overall more complex than those for SnO_2–**3**, but have the same 3 characteristic features, including a new transient feature at λ_{max} = 460 nm, bleaching of the Q-band absorptions from 495–590 nm, and a new, broad transient feature from 600–750 nm. These new features match those of the radical cation $\mathbf{4}^{\bullet+}$ (Figure 4.10C). These transient features are distinctly different from those of the porphyrin triplet (Figure 4.10B), which is characterized by a strong absorption with λ_{max} < 450nm, and broad, weak absorbances throughout the visible. It is worth noting that after 9 μs, the only remaining absorbance features in the SnO_2–**1** transient absorption spectrum are those of the free base porphyrin triplet. Based on these results, intersystem crossing to the triplet excited state (Equation 4.2) competes with electron injection from the singlet excited state (Equation 4.1a). These results are consistent with similar porphyrin system which have been shown to undergo excited–state electron injection into SnO_2 via time-resolved terahertz spectroscopy.[29] A detailed analysis of these photophysics is currently under investigation.

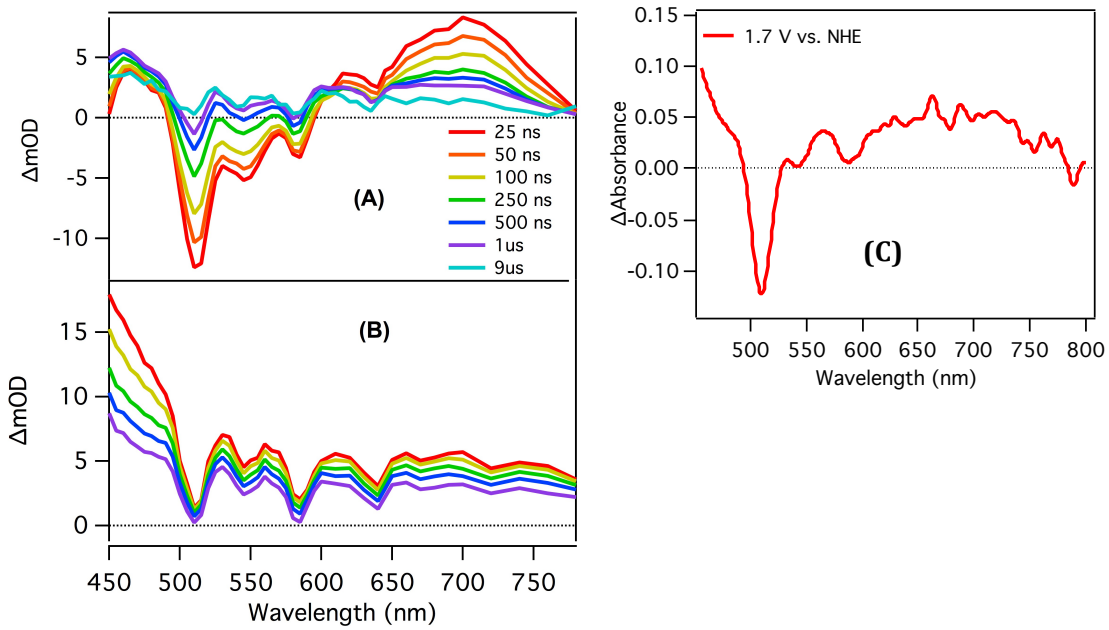

Figure 4.10: A) Time dependent transient absorption difference spectra for SnO_2–**1** following 425 nm excitation in CH_3CN (0.1 M $LiClO_4$). **B)** Time dependent transient absorption difference spectra for ZrO_2–**1** following 425 nm excitation in CH_3CN (0.1 M $LiClO_4$). **C)** P^+–P absorption difference spectra for **4** in MeCN (0.1 M [^{n}Bu$_4$N][PF_6]) at 1.7 V vs. NHE as determined via a spectroelectrochemical titration.

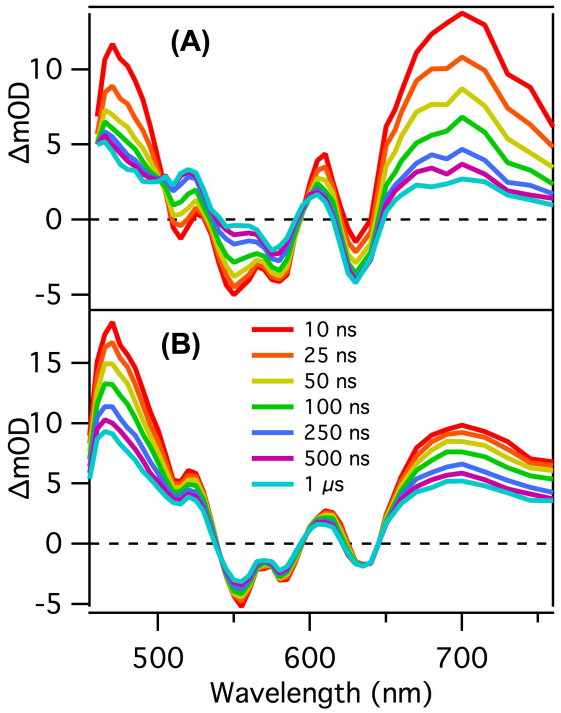

Figure. 4.11 A) Time-dependent transient absorption difference spectra for SnO_2–**1** and **B)** ZrO_2–**1** in aqueous 0.1 M $HClO_4$ after excitation at 425nm.

Transient absorption measurements for SnO_2–**1** were also conducted in aqueous 0.1 M $HClO_4$ solutions (Figure 4.11A) and the absorption features of the triplet excited state of **1** were characterized on *nano*ZrO_2 (Figure 4.11B). As with the transient absorption spectra for SnO_2–**1** in CH_3CN, absorbance contributions from both the oxidized porphyrin and the triplet excited state are observed. In fact, at 1 μs the transient spectrum is strongly dominated by the porphyrin triplet absorbance. Nonetheless, the differences in the early time spectra indicate the presence of the porphyrin cation, including a transient absorption feature at 465 nm, bleaching of the Q-band absorptions from 500–600 nm, and a broad absorption from 600–750 nm. These differences are clearly illustrated by subtracting the SnO_2–**1** and ZrO_2–**1** transient absorption spectra at 10 ns (Figure 4.12). Appearance of the oxidized porphyrin suggests excited-state injection occurs in competition with intersystem crossing to form the porphyrin triplet excited state under these conditions.

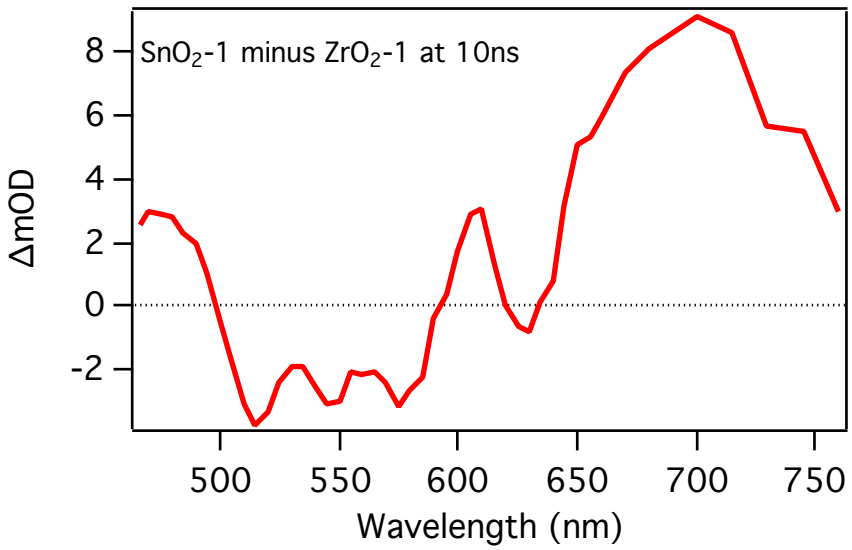

Figure 4.12: Subtraction of ZrO_2–**1** TA spectrum at 10 ns (scaled) from SnO_2–**1** TA spectrum at 10 ns, illustrating the formation of $\mathbf{1}^+$ in aqueous 0.1 M $HClO_4$.

Molecular assemblies were prepared on *nano*MO_2 surfaces by a 'layer-by-layer' deposition strategy described previously.[215–217,223] In the layer-by-layer procedure, Zr(IV) (as $ZrOCl_2$) is added to the distal $–PO_3H_2$ functional group on the surface-bound porphyrin. A second phosphonate-derivatized chromophore or catalyst is then bound to the Zr(IV) linker forming the surface-bound assembly. While co-adsorbed systems of chromophores and catalysts on metal oxide surfaces have been previously studied, chromophore-catalyst assemblies which position the catalyst distal to the surface are desirable. This design strategy attenuates back electron transfer from the reduced metal oxide surface to the oxidized catalyst. Preparation of covalently bound chromohore-catalyst assemblies is challenging as they require rigorous synthetic procedures which often have low synthetic yields.[82,109,224] The layer-by-layer deposition strategy described in this paper bypasses extensive synthesis by forming chromohore-catalyst assemblies on surface from individual catalyst and chromophore components.

The layer-by-layer procedure was applied to the preparation of a chromophore–catalyst assembly. In these experiments, SnO_2 slides were dipped sequentially into solutions of **1** (1.2 mM in MeOH), $ZrOCl_2$ (5 mM in 0.1 M $HClO_4$), and **2** (350 mM in MeOH) successively for 4 h in each solution. The resulting structure is illustrated in Figure 1B. Assembly growth was monitored by absorbance measurements (Figure 4.13). The large absorbance change observed with the Zr(IV) linker and added catalyst as the third layer is due to assembly formation and not displacement of the porphyrin by the catalyst. This was demonstrated by dipping a pre-loaded SnO_2–**1** (Figure 4.13) slide into a solution of **2,** and measuring the absorbance after a 30 min soaking period. Based on the absorbance increase at 500 nm, a λ_{max} for the Ru(II) complex, co-deposition of **2** on the surface of **1** was ≤ 15% of

the initial porphyrin loading. Over extended periods, further changes in the absorption spectrum were observed consistent with slow displacement of the porphyrin from the surface by the catalyst.

By contrast, after dipping the porphyrin-loaded slide in a $ZrOCl_2$-containing solution followed by catalyst **2**, a near doubling of the absorbance at 500 nm was observed consistent with formation of a 1:1 chromophore:catalyst adduct on the surface and formation of the SnO_2–**1**–Zr–**2** assembly (Figure 4.13). Additional support for the formulation of the stoichiometric assembly was obtained by XPS. Analysis of the XPS data demonstrated a 4:1 ratio of Phosphorus to Ruthenium and an 11:1 ratio of Nitrogen to Ruthenium, both consistent with the proposed 1:1 chromophore–catalyst ratio (Table 4.1).

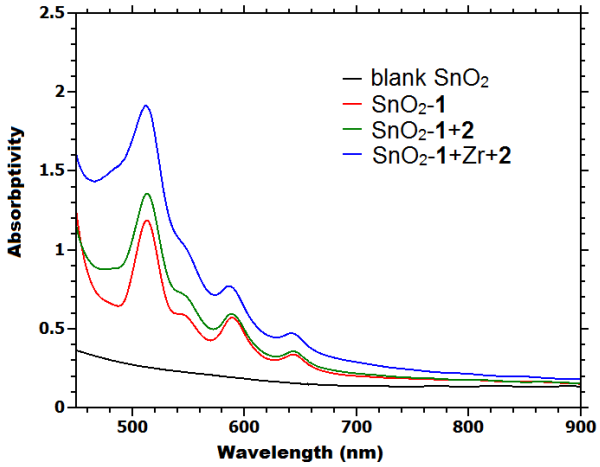

Figure. 4.13 UV-visible spectrum of the layer-by-layer chromophore–catalyst assembly SnO_2–**1**–Zr–**2** in CH_3CN.

Table 4.1: X-ray photoelectron spectroscopy (XPS) of TiO_2–**1**–Zr–**2**

	N/Ru ratio	P/Ru ratio	F/Ru ratio
TiO_2–**1**–Zr–**2**	11.7	4.1	13.8[1]
Ideal	11	4	10
[1]Deviations from ideal may be due to fluorine contributions from PF_6 anion and FTO.			

Transient absorption difference spectra for SnO_2–**1**–Zr–**2** in aqueous 0.1 M $HClO_4$ at a series of delay intervals following excitation at 425 nm are shown in Figure 4.14A. At the earliest observation time (10 ns), a bleach appears at λ_{max} = 470 nm consistent with loss of the MLCT absorption of complex **2**. Rapid appearance of the bleach is consistent with excitation of the porphyrin, excited-state injection, and rapid intra-assembly electron transfer between the porphyrin radical cation and Ru(II) catalyst (Equation 4.3a). Although a competitive light absorber, the catalyst MLCT excited state is short-lived (< 10 ns) and presumably does not contribute to the injection/electron transfer sequence.[217]

$$SnO_2\text{-}\mathbf{1}\text{-}Zr(IV)\text{-}Ru^{II}\text{-}OH_2^{2} \xrightarrow{h\nu} SnO_2\text{-}{}^{1}\mathbf{(1^*)}\text{-}Zr(IV)\text{-}Ru^{II}\text{-}OH_2^{2+} \rightarrow SnO_2(e^-)\text{-}\mathbf{1}^{+}\text{-}Zr\text{-}Ru^{II}\text{-}OH_2^{2+}$$

$$\rightarrow \quad SnO_2(e^-)\text{-}\mathbf{1}\text{-}Zr\text{-}Ru^{III}\text{-}OH_2^{3+} \qquad (4.3a)$$

$$SnO_2(e^-)\text{-}\mathbf{1}\text{-}Zr\text{-}Ru^{III}\text{-}OH_2^{3+} \rightarrow SnO_2\text{-}\mathbf{1}\text{-}Zr\text{-}Ru^{II}\text{-}OH_2^{2+} \qquad (4.3b)$$

By contrast, in the transient absorption difference spectra measured for ZrO_2–**1**–Zr–**2** (Figure 4.14B), there is no evidence for the MLCT bleach and the signature absorption features of the porphyrin triplet excited state dominate the spectra. Although a detailed analysis of the photophysical data is currently under investigation, there is clearly a contribution of the triplet excited state in the SnO_2–**1**–Zr–**2** difference spectra (Figure 4.14A) indicating competition between injection/catalyst oxidation (Equation 4.3) and triplet formation/decay (Equation 4.4).

$$SnO_2\text{-}\mathbf{1}\text{-}Zr(IV)\text{-}Ru^{II}\text{-}OH_2^{2+} \xrightarrow{h\nu} SnO_2\text{-}{}^{1}\mathbf{(1^*)}\text{-}Zr\text{-}Ru^{II}\text{-}OH_2^{2+} \rightarrow SnO_2\text{-}{}^{3}\mathbf{(1^*)}\text{-}Zr\text{-}Ru^{II}\text{-}OH_2^{2+}$$

$$\rightarrow SnO_2\text{-}\mathbf{1}\text{-}Zr(IV)\text{-}Ru^{II}\text{-}OH_2^{2+} \qquad (4.4)$$

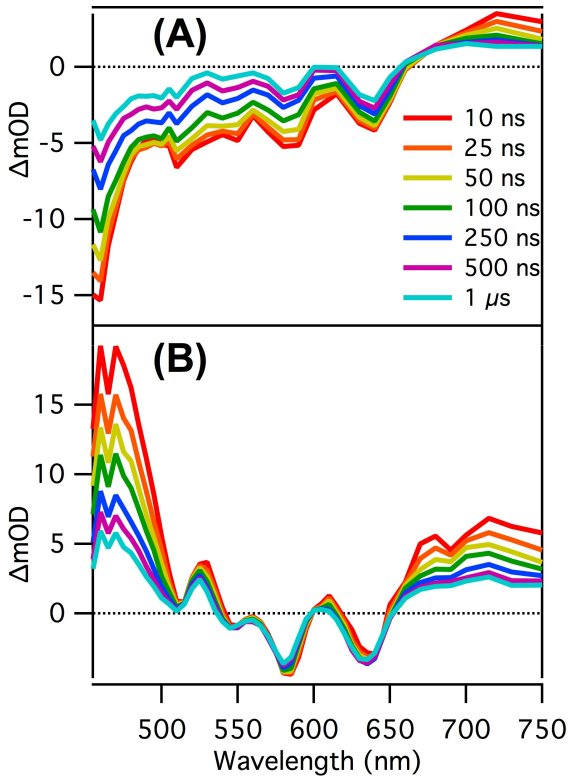

Figure. 4.14 Time-dependent transient absorption difference spectra for **A)** SnO_2–**1**–Zr–**2**, and **B)** ZrO_2–**1**–Zr–**2** in in aqueous 0.1 M in $HClO_4$ following excitation at 425nm.

4.4. Conclusion

We demonstrate here the first application of a layer-by-layer procedure for the construction of antenna and chromophore–catalyst assemblies on mesoporous, nanoparticle metal oxide films with phosphonate-derivatized porphyrins. The generality and simplicity of this layer-by-layer procedure make it especially appealing with general application to porphyrins, metal complexes, and organic chromophores. Initial photophysical measurements reveal excited-state electron injection into SnO_2 for both **1** and **3** with the ability of the photoproduced oxidized porphyrin $\mathbf{1}^+$ to transfer the oxidative equivalent to the catalyst. It is clear that this is a promising approach for the preparation of a family of surface-bound assemblies for possible use in device applications.

CHAPTER 5. Charge Recombination Dynamics in Sensitized SnO_2/TiO_2 Core/Shell Photoanodes

Reprinted with permission from Knauf, R. R.; Kalanyan, B.; Parsons, G. N.; Dempsey, J. L. Charge Recombination Dynamics in Sensitized SnO_2/TiO_2 Photoanodes. *J. Phys. Chem. C* **2015,** *119* (51), 28353-28360.

5.1. Introduction

Technologies such as dye-sensitized solar cells and dye-sensitized photoelectrosynthesis cells provide viable strategies for solar energy conversion.[45,83,205] Essential to both device architectures are surface-bound chromophores which absorb visible light and inject electrons into the conduction band of a mesoporous metal oxide semiconductor. For DSPEC devices, long-lived charge separation is crucial for carrying out multi-electron, multi-proton fuel formation reactions. As such, minimizing detrimental charge recombination (back electron transfer) is key in fabricating operative and efficient DSPEC devices.

Several strategies have been developed to slow the rates of BET in metal oxide-chromophore systems, including the use of long molecular linkers,[25,48,115,116] incorporation of donor-acceptor chromophores,[30,31,117–119] and implementation of core/shell metal oxide electrode structures.[47,120,122–127] Core/shell structures, where the conduction band potential of the shell is more negative than the core, allow for an energetically uninhibited electron injection while providing a significant barrier for BET from core-localized electrons. The use of atomic layer deposition (ALD) to construct core/shell metal oxide structures has been shown to increase DSSC device efficiencies[47,120,124] and to help achieve water splitting in

DSPEC devices.[84] Although it has been proposed that the observed performance enhancement for core/shell systems is due to a decreased BET rate, the interfacial electron transfer dynamics of these emerging core/shell materials have not been directly quantified and detailed mechanisms remain unclear.[126,127] In response, we sought to reveal how BET dynamics and shell thickness are correlated and elucidate charge recombination pathways in these materials.

In this study, we use transient absorption spectroscopy to quantify the kinetics of back electron transfer between injected electrons and oxidized surface-bound ruthenium polypyridyl chromophores for SnO_2/TiO_2 core/shell systems with varying TiO_2 shell thicknesses. Both amorphous and crystalline TiO_2 shells on nanocrystalline SnO_2 films were investigated to identify the charge recombination pathways controlling BET rates. We reveal that when the injected electrons localize in the core, shells of amorphous TiO_2 act as a tunneling barrier for charge recombination and BET is attenuated with the anticipated distance dependence as predicted by electron tunneling theory.[225,226] However, as these shells become thicker, an increasingly large fraction of the injected electrons remain localized in the shell and direct recombination from these states ensues. The relative contribution of each mechanism is dependent on the TiO_2 shell thickness. By contrast, when the films are annealed to produce crystalline TiO_2 shells, the BET dynamics display no dependence on TiO_2 shell thickness apart from an initial surface passivation, suggesting the core/shell interface is perturbed in the annealing process. Together, these results reveal that 1) there is an ideal shell thickness for optimizing BET rates in dye-sensitized core/shell films and 2) localization of injected electrons in the core materials is sensitive to the core/shell interface.

5.2. Experimental

5.2.1. Nanocrystalline SnO_2 and ZrO_2 Film Fabrication

SnO_2 and ZrO_2 nanoparticle films were prepared via previously published procedures.[110,222] SnO_2 and ZrO_2 nanoparticle films were 3.2 μm and 1.4 μm thick, respectively. The SnO_2 and ZrO_2 nanoparticles employed were approximately 15 nm and 10 nm in diameter, respectively.

5.2.2. Atomic Layer Deposition of TiO_2 Shells

Atomic layer deposition was conducted in a custom-built, hot walled, flow tube reactor described previously.[227] Reactant precursor gases, including $TiCl_4$ (99%, Strem Chemicals) and reagent grade water (Ricca Chemicals) were delivered to the reactor though heated gas lines using nitrogen carrier flow (99.999% purity, National Welders) further purified (Entegris Gate-Keeper) to reduce water contamination. The reactor was configured with gate valves to isolate the deposition zone, allowing the deposition substrate to receive extended exposure or "hold" steps to promote precursor diffusion throughout the inorganic oxide nanoparticle films.[228] Deposition was performed at 120 °C. Precursor gas flow timing was controlled electronically by a LabVIEW sequencer to achieve dose/hold/purge steps of 0.3/60/180 seconds, respectively, for the $TiCl_4$ and water reactants.

5.2.3. Chromophore Synthesis

$[Ru(bpy)_2(4,4'\text{-}(PO_3H_2)_2bpy)]^{2+}$ (RuP) was prepared by previously reported methods.[46]

5.2.4. Surface Loading of SnO_2/TiO_2-RuP Films

For this study, all films were fully loaded with the RuP chromophore. Sensitizers

were anchored to the SnO_2/TiO_2 core/shell films by soaking overnight in 0.1 M $HClO_4$ aqueous solutions containing RuP ($1x10^{-5}$ – $2x10^{-4}$ M). Slides were then soaked for 4 hours in aqueous 0.1 M $HClO_4$ solution to remove excess unanchored chromophores. Absorbance measurements of the films were performed using a Cary 60 UV-vis absorbance spectrophotometer.

5.2.5. Powder X-ray Diffraction

Powder X-ray diffraction (pXRD) was performed using a Rigaku Multiflex (CuKα, 40 kV, 40 mA) from 15° to 70° 2θ with a scan rate of 1° 2θ/min.

5.2.6. Transmission Electron Microscopy

Transmission Electron Microscopy (TEM) analysis was performed on JEOL 2010F FasTEM using an accelerating voltage of 200 kV.

5.2.6. Transient Absorption Spectroscopy

Transient absorption experiments were performed as described previously.[28] Briefly, measurements were performed using a commercial laser flash photolysis system (Edinburgh Instruments, Inc., model LP920) with laser excitation (470 nm, 7 ns FWHM, 3.8 mJ/pulse unless stated otherwise) provided by a pulsed Nd:YAG laser (Spectra-Physics, Inc., model Quanta-Ray LAB-170-10) / OPO (VersaScan-MB) combination. Single wavelength transient absorption kinetics were monitored using a multi-grating detection monochromator outfitted with a Hamamatsu R928 photomultiplier tube (50 averages, bandwidth <5nm). The LP920 white light probe output was passed through a 380 nm long pass color filter before passing through the sample to minimize band gap excitation of the metal oxide. Kinetic data were analyzed using Igor Pro (WaveMetrics Inc.).

5.3. Results

5.3.1. Characterization of SnO_2/TiO_2 Films

Conformal shells of TiO_2 were deposited on nanocrystalline SnO_2 and ZrO_2 films via ALD. Samples with varying TiO_2 shell thicknesses were obtained by altering the number of ALD cycles performed on the substrates. Previous studies have shown that similar process conditions lead to 0.6 Å of TiO_2 for each ALD cycle,[127] further confirmed here using ellipsometry on planar silicon coated simultaneously with the porous oxide substrates. To investigate the effects of annealing, some SnO_2/TiO_2 films were annealed in air at 450 °C for 30 minutes.

Due to the low deposition temperature, the as-deposited TiO_2 shells are amorphous.[229,230] The powder X-ray diffraction spectrum from an as-deposited SnO_2/TiO_2 sample (7.1 nm TiO_2 shells) is dominated by peaks corresponding to the rutile SnO_2 core and FTO background, and show no perceivable difference from the SnO_2 films without TiO_2 deposited.[231,232] However, upon annealing at 450 °C, the diffraction spectrum (Figure 5.1) exhibits new peaks corresponding to anatase TiO_2 along with peaks of smaller intensity corresponding to rutile TiO_2, indicating the annealing process leads to crystalline TiO_2, consistent with previous reports of ALD-deposited TiO_2 on planar substrates.[229] TEM images indicate the conformal shell coating is maintained during the annealing process (Figure 5.2).

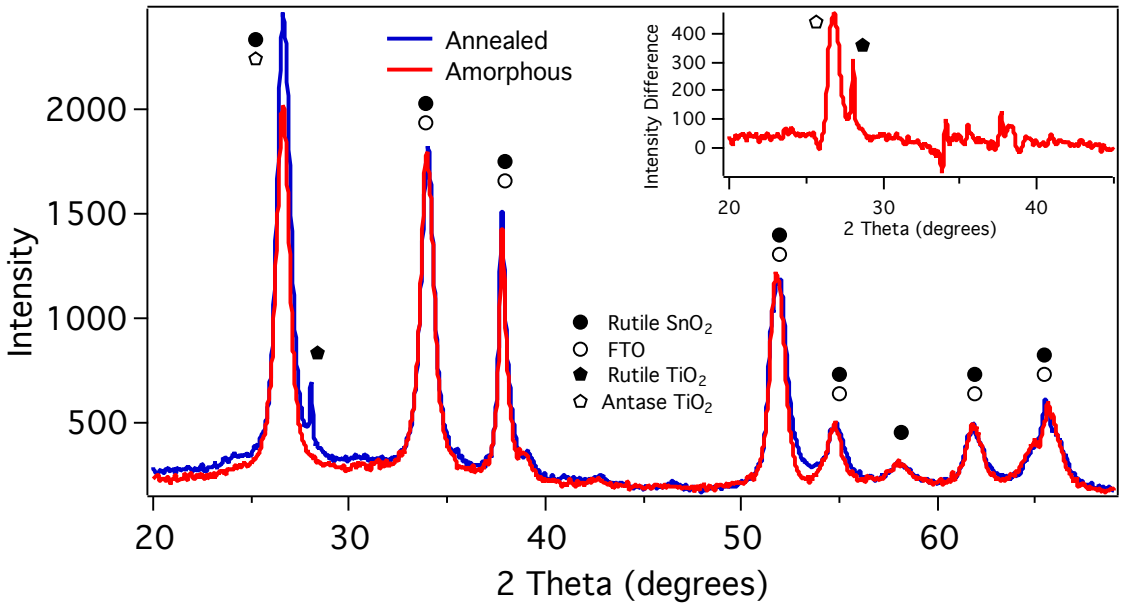

Figure 5.1: Powder XRD spectra of SnO_2/TiO_2 core/shell films with TiO_2 thickness of 7.1 nm as deposited (red, amorphous) and after annealing at 450° C (blue, annealed). The inset depicts the difference in intensity between these traces, with new peaks corresponding to anatase and rutile TiO_2.

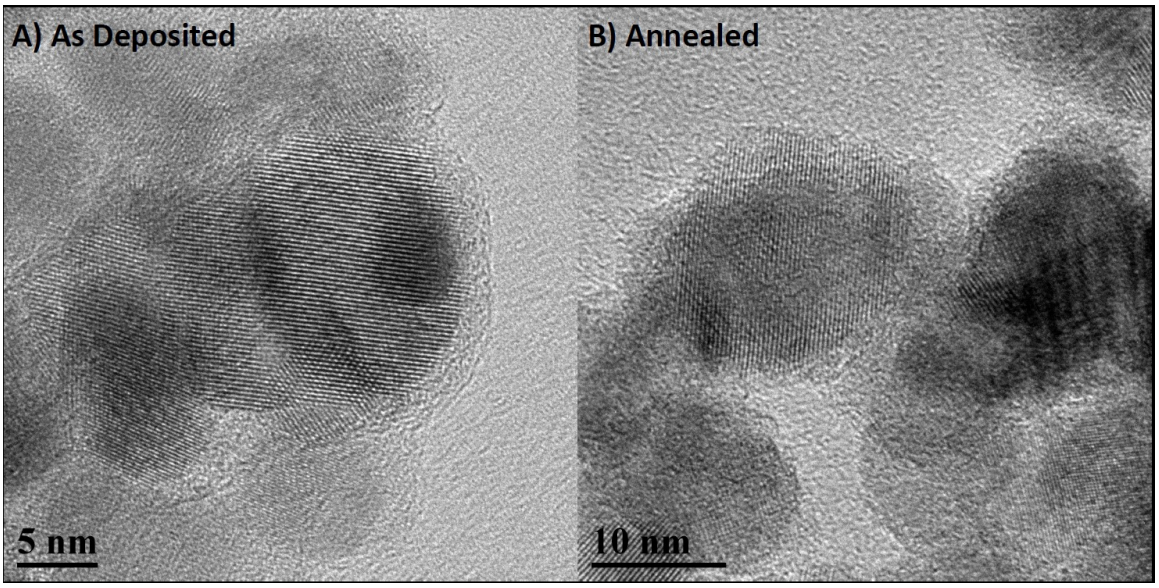

Figure 5.2: TEM images of SnO_2 nanoparticles with 2.9 nm shells of TiO_2 **A)** as deposited and **B)** after annealing at 450 °C. Conformal shell coating is observed in both samples.

The SnO_2/TiO_2 and ZrO_2/TiO_2 core/shell films were loaded with the phosphonate-functionalized ruthenium chromophore $[Ru(bpy)2(4,4'-(PO_3H_2)bpy)]^{2+}$ (RuP, bpy = 2,2′-bipyridine; 4,4′-(PO_3H_2)bpy = 4,4′-bis(methylphosphonic acid)-2,2′-bipyridine). Dye loading was quantified via absorption measurements of films.[222] Although the absorbance appears to increase with TiO_2 thickness, scattering and background TiO_2 absorbance also increase, as evidenced by the net background absorbance increase observed across the spectra (Figure 5.3). When discounting these contributions, we determined that loading decreases slightly with increasing the shell thickness, consistent with a reduction in surface area that accompanies the increase in particle diameter upon conformal ALD. There were no apparent differences in dye loading between the amorphous and annealed films, however the dye loading for the ZrO_2/TiO_2 was slightly less than half that of the SnO_2/TiO_2 films (Figure 5.3). This is consistent with the thinner ZrO_2 particle layers (1.4 μm) as compared to the SnO_2 layers (3.2 μm). The core particle sizes are roughly 15 nm and 10 nm for SnO_2 and ZrO_2, respectively.

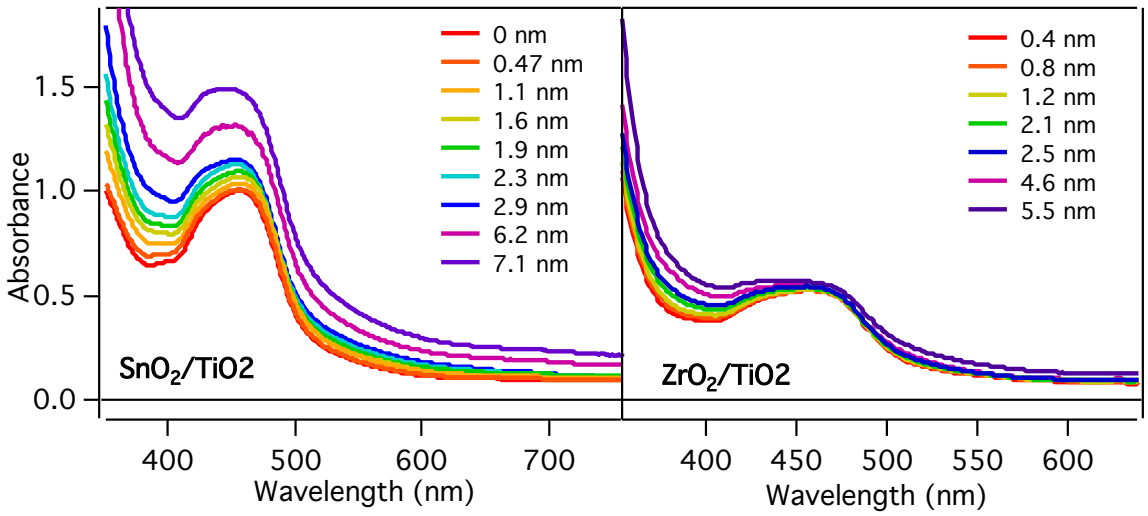

Figure 5.3: Absorption spectra of RuP-sensitized SnO_2/TiO_2 and ZrO_2/TiO_2 core/shell films in 0.1 M aqueous $HClO_4$ with varying TiO_2 shell thickness.

5.3.2. Interfacial Charge Recombination Dynamics in Amorphous Films

Single-wavelength transient absorption (TA) measurements were utilized to monitor the charge recombination dynamics of the RuP-derivatized core/shell films. Kinetics analyses were carried out on traces recorded at the RuP ground-state/excited-state isosbestic point (λ_{obs} = 400 nm), allowing the oxidized chromophore to be monitored without convolution from excited-state dynamics.[176] The recombination dynamics for the SnO_2/TiO_2–RuP systems are complex and span a range of timescales. Related studies have used a variety of models to fit these kinetics, including equal concentration second-order kinetics, stretched exponential fits, and triexponential functions.[94,97,170,178,180,222] In order to obtain a single metric to compare recombination kinetics across and range of TiO_2 thicknesses, we characterized the BET dynamics by the $\tau_{1/2}$ parameter, the time at which the signal has decreased to half of its original amplitude.

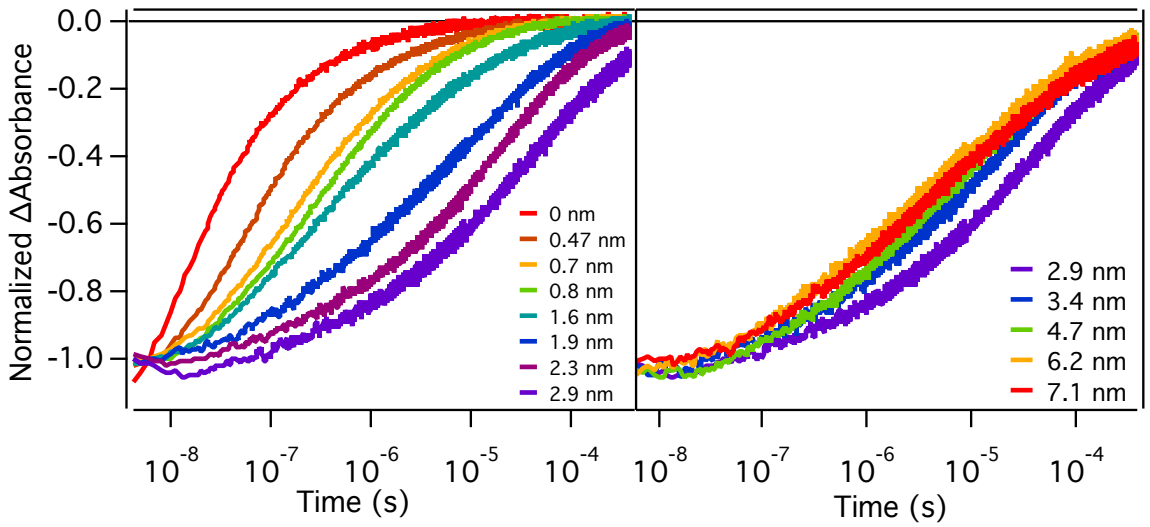

Figure 5.4. Normalized transient absorption kinetics of SnO_2/TiO_2–RuP monitored at 400 nm in aqueous 0.1M $HClO_4$ at various TiO_2 thicknesses (λ_{ex} = 470 nm, 3.8 mJ/pulse).

Kinetics traces for the amorphous SnO_2/TiO_2–RuP samples are shown in Figure 5.4. At equal pulse energies, the injection yields decrease with increasing shell thickness; to aid in

visual comparison, the bleach magnitude has been normalized. For the bare SnO_2 films, a $\tau_{1/2}$ of 39 ns is observed, consistent with previous measurements.[222] As the shell thickness is increased from 0 to 2.9 nm, the recombination time increases by three orders of magnitude to 28 μs (Table 5.1). However, as the amorphous TiO_2 shells thickness exceeds 2.9 nm, recombination begins to accelerate (Figure 5.4). For the thickest TiO_2 shells examined (> 6.2 nm), $\tau_{1/2}$ levels and the recombination dynamics become shell thickness independent.

Table 5.1: Bleach Magnitudes and $\tau_{1/2}$ Values for Amorphous SnO_2/TiO_2 Films

	Equal Pulse Energy (3.8 mJ/pulse)		Equal Injection (mΔOD ≈ 40)	
TiO_2 Thickness (nm)	$\tau_{1/2}$ (μs)[a]	Bleach Magnitude (ΔmOD)[a,b]	$\tau_{1/2}$ (μs)[a]	Pulse Energy (mJ)[a]
0	0.039	68	0.031	2.6
0.4	0.106	74	0.125	2.2
0.5	0.152	70	0.175	2.4
0.7	0.241	73	0.320	2.3
0.8	0.349	73	0.450	2.3
1.1	0.616	62	0.691	3.4
1.6	2.045	48	1.321	4.2
1.9	6.790	40	2.784	5.4
2.3	13.674	33	5.000	5.9
2.9	27.536	29	8.332	6.7
3.4	12.992	38	11.360	4.3
3.8	9.853	36	6.976	4.4
4.7	5.999	38	4.770	4.2
6.2	4.000	43	4.356	3.8
7.1	4.208	37	3.908	4.0

[a] Values are the average of 3 measurements
[b] Measured at the first observation point (10 ns)

As noted above, injection yields decrease with shell thickness as determined by the magnitude of the bleach at the earliest observation point recorded (ca. 10 ns). This likely arises in part to the decrease in surface coverage with increasing shell thickness (see above), though contributions from ultrafast back electron transfer processes that are shell-thickness

dependent are also possible. As BET dynamics have been shown to depend on the density of injected electrons in metal oxide-chromophore systems,[100,103,170,222] we also performed experiments with varied excitation pulse energy in order to achieve equivalent injection yields at the first observation timepoint (Figure 5.5). With equal injection yields, the $\tau_{1/2}$ values also increase with TiO_2 thickness up to 3.4 nm then decrease, very similar to the trends observed with equal excitation pulse energies (Table 5.1). Subtle differences between the two data sets—including the SnO_2-only BET rates and specific shell thickness with the longest charge separation—arise solely from differences in excitation pulse energies. These experiments confirm that the decrease in BET rate with increased TiO_2 shell thickness results from factors other than the diminished injection yields. Analysis was performed for both equal injection and equal pulse energy experiments and yielded very similar results. We choose to focus on the equal injection yields experiment for further discussion, consistent with previous work in **Chapter 3**.[222]

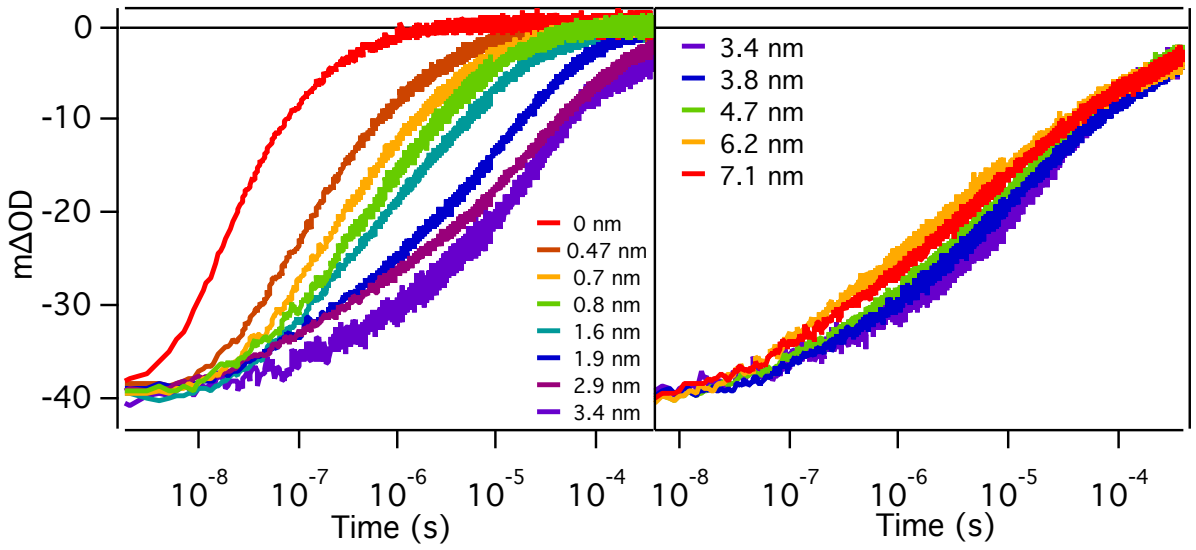

Figure 5.5. Transient absorption kinetics of SnO_2/TiO_2-RuP at 400 nm in aqueous 0.1 M $HClO_4$ at various TiO_2 thicknesses. Pulse energies are varied to obtain the same ΔOD at 10 ns. (λ_{ex} = 470 nm).

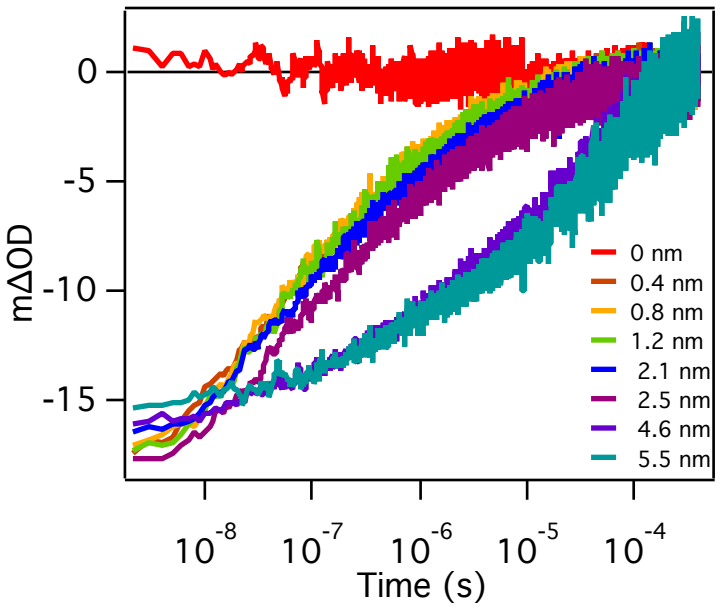

Figure 5.6: Transient absorption kinetics of as deposited ZrO_2/TiO_2–RuP at 400 nm in aqueous 0.1M $HClO_4$ at various amorphous TiO_2 thicknesses. Pulse energies are varied to obtain the same ΔOD at the first observation point, 10 ns (λ_{ex} = 470 nm).

Kinetics of BET were also recorded for sensitized ZrO_2/TiO_2 core/shell films, which served as control samples. The conduction band potential of the ZrO_2 core is ca. –1.5 V vs. NHE, 0.9 V more positive than the conduction band of TiO_2.[220] As such, electrons inject into the TiO_2 shell, but cannot localize in the ZrO_2 core. These control samples allow us to isolate the recombination dynamics of electrons localized in the TiO_2 shell. For as deposited ZrO_2/TiO_2 structures, the TA spectra recorded at equal injection yield (Figure 5.6, Table 5.2) showed an increase in $\tau_{1/2}$ from 102 ns to 4 μs as the TiO_2 shell thickness increases from 0.4 nm to 6.8 nm. As shell thickness is increased further, $\tau_{1/2}$ plateaus. As expected, no injection is observed for sensitized ZrO_2 nanoparticles without TiO_2 shells. Similar observations have been made by Meyer and coworkers and attributed to an enhanced density of TiO_2 states with increasing TiO_2 shell thickness.[127] A higher density of shell acceptor states is expected to slow the rate of BET if recombination of injected electrons occurs via a trapping/detrapping mechanism.[21,198,222,233] Notably, for ZrO_2/TiO_2 and SnO_2/TiO_2 core/shell samples with shell

thicknesses greater than 6 nm, the $\tau_{1/2}$ values for BET converge, suggesting recombination proceeds by a similar mechanism in thick-shelled samples (see below).

Table 5.2: Pulse Energies and $\tau_{1/2}$ Values for Amorphous and Annealed ZrO_2/TiO_2 Films (Equal Injection)

	Amorphous (Fig. 5.6)		Annealed (Fig. 5.10)	
TiO_2 Thickness (nm)	$\tau_{1/2}$ (μs)[a]	Pulse Energy (mJ)[a]	$\tau_{1/2}$ (μs)[a]	Pulse Energy (mJ)[a]
0	—	3.8	—	3.8
0.4	0.102	4.3	0.120	4.0
0.8	0.105	4.2	0.125	4.0
1.2	0.115	3.8	0.155	3.8
2.1	0.171	3.2	0.261	3.0
2.5	0.233	3.0	0.314	2.5
4.6	2.60	2.8	0.541	2.4
5.5	3.70	3.6	0.559	2.9
6.8	4.05	4.2	0.621	4.0
[a] Values are the average of 3 measurements				

For the ZrO_2/TiO_2 structures, experiments at equal pulse energies were also performed (Figure 5.7). In these experiments the magnitude of the bleach at 400 nm increased dramatically with increased TiO_2 thickness, likely due to the increased number of acceptor states in the shell. For this reason the equal injection data for ZrO_2/TiO_2 films was used for analysis.

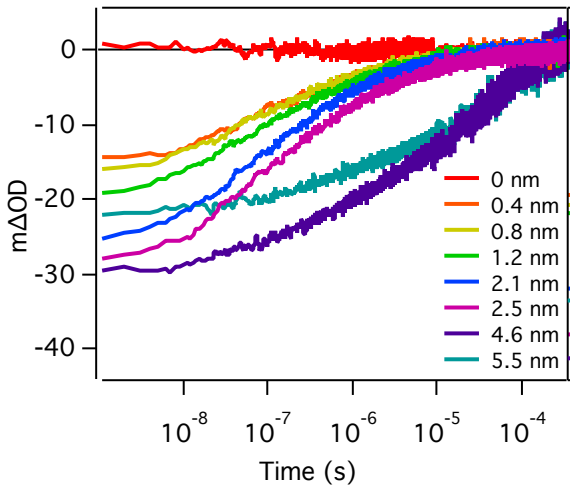

Figure 5.7: TA kinetics amorphous ZrO_2/TiO_2–RuP at 400 nm in aqueous 0.1M $HClO_4$ at various TiO_2 thicknesses. Pulse energies 3.8 mJ for all TiO_2 thicknesses (λ_{ex} = 470 nm).

5.3.3. Interfacial Charge Recombination Dynamics in Annealed Films

BET dynamics were also investigated for SnO_2/TiO_2 and ZrO_2/TiO_2 films that had been annealed at 450 °C for 30 minutes prior to dye sensitization. Kinetics traces for the charge recombination in annealed SnO_2/TiO_2–RuP systems with equal excitation pulse energies are shown in Figure 5.8. As the shell thickness increases from 0 to 0.5 nm, $\tau_{1/2}$ increases by roughly one order of magnitude compared to bare SnO_2. However, there is no significant change in the recombination dynamics as the TiO_2 shell thickness is increased beyond 0.5 nm. This observation is in stark contrast to the trend observed for core/shell samples with amorphous TiO_2 shells. Additionally, the amplitude of the bleach at 400 nm does not change dramatically with increased TiO_2 thickness, indicating roughly equal injection yields are obtained at equal pulse energy (Figure 5.9, Table 5.3).

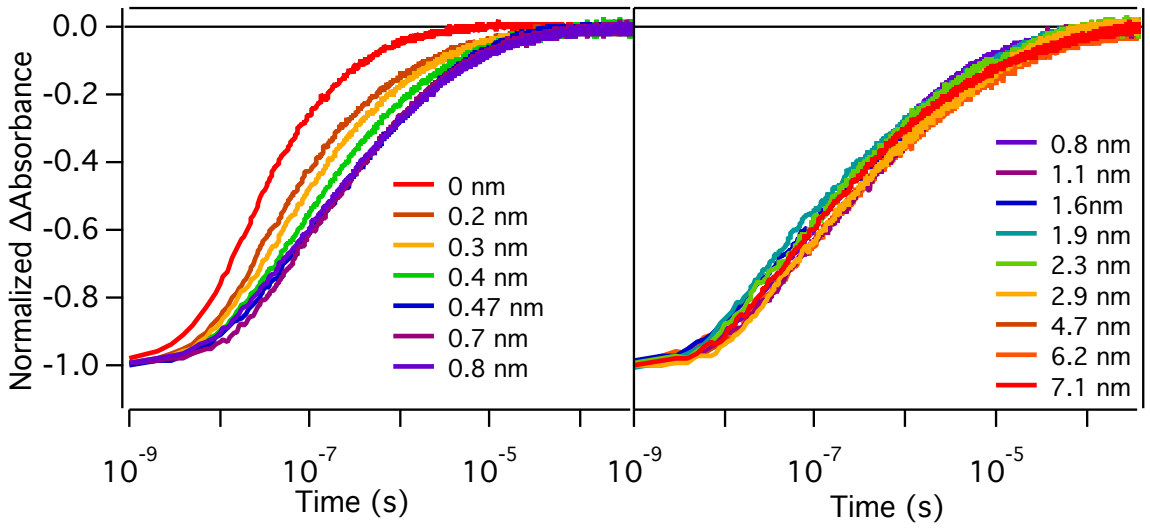

Figure 5.8: Normalized transient absorption kinetics of SnO_2/TiO_2-RuP at 400 nm in aqueous 0.1M $HClO_4$ at various TiO_2 thicknesses after annealing at 450 °C (λ_{ex} = 470 nm, 3.8 mJ/pulse).

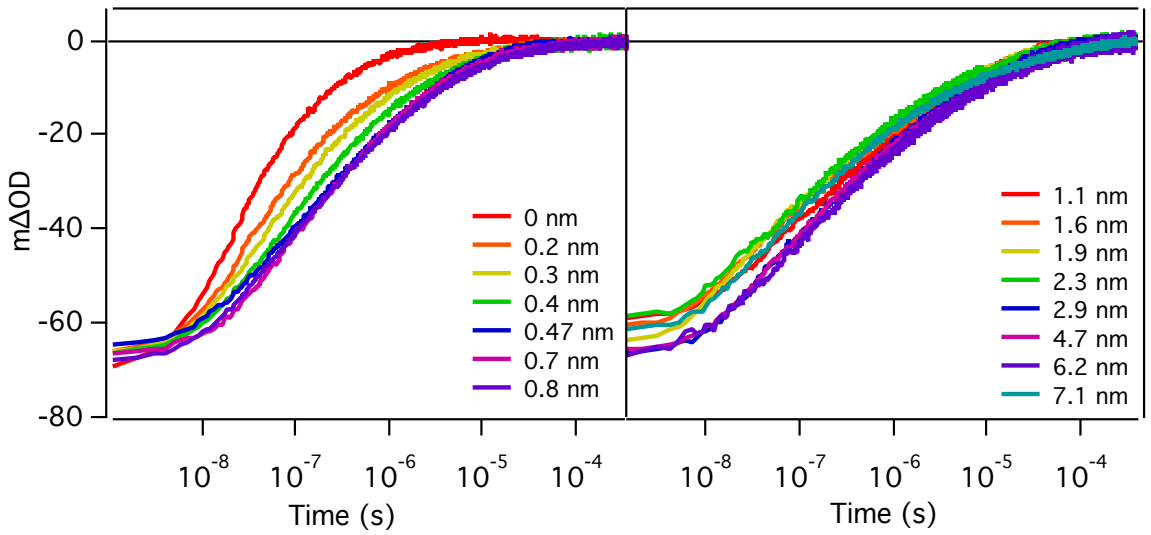

Figure 5.9: Transient absorption kinetics traces of SnO_2/TiO_2–RuP at 400 nm in aqueous 0.1M $HClO_4$ at various TiO_2 thicknesses after annealing at 450 °C (λ_{ex} = 470 nm, 3.8 mJ/pulse).

Table 5.3: Bleach Magnitudes and $\tau_{1/2}$ Values for Annealed SnO_2/TiO_2 Films

Equal Pulse Energy (3.8 mJ/pulse)		
TiO_2 Thickness (nm)	$\tau_{1/2}$ (μs)	Bleach Magnitude (ΔmOD)
0	0.030	71
0.2	0.066	67
0.3	0.094	67
0.4	0.139	67
0.5	0.205	65
0.7	0.214	67
0.8	0.197	69
1.1	0.254	60
1.6	0.180	62
1.9	0.195	64
2.3	0.179	59
2.9	0.251	66
3.4	0.227	60
4.7	0.276	66
6.2	0.308	68
7.1	0.346	62
[a] Measured at the first observation point (10 ns)		

For comparison, kinetic traces for annealed ZrO_2/TiO_2 films performed with equal injection yields are shown in Figure 5.10. For these control samples, the $\tau_{1/2}$ of BET increases with increasing film thickness from 120 ns at 0.4 nm to 620 ns at 6.8 nm (Table 5.2). The attenuation of recombination rates is much smaller than what is observed for the amorphous shells and is attributed to the lower density of trap states and better electron transport in the crystalline material compared to the amorphous TiO_2.[234]

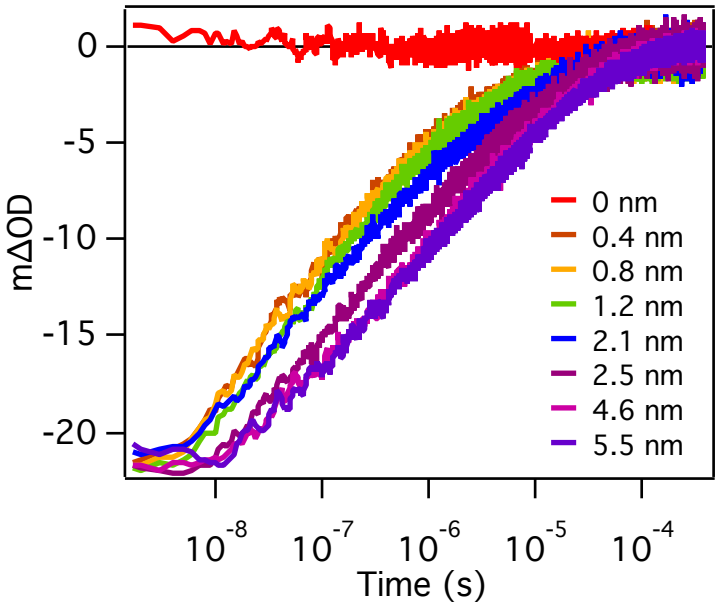

Figure 5.10: Transient absorption kinetics of annealed ZrO_2/TiO_2–RuP at 400 nm in aqueous 0.1M $HClO_4$ at various TiO_2 thicknesses. Pulse energies are varied to obtain the same ΔOD at the first observation point (λ_{ex} = 470 nm).

5.4. Discussion

5.4.1. Correlating Recombination Dynamics with Metal Oxide Shell Thicknesses

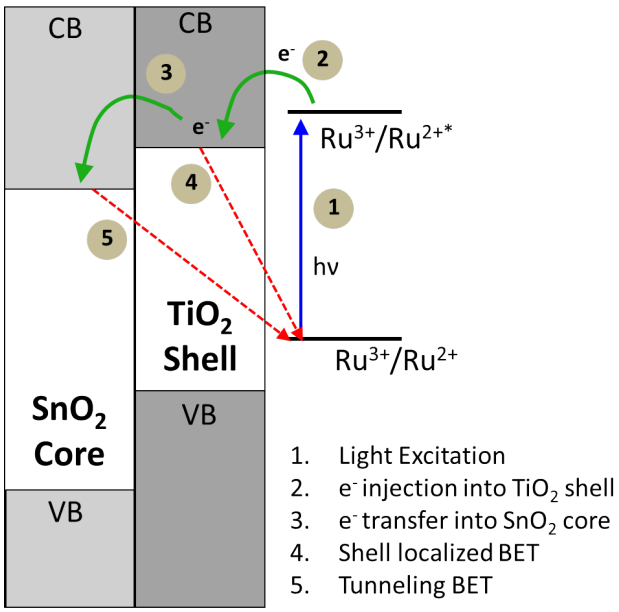

Figure 5.11. Qualitative schematic of the conduction band energies of the core and shell metal oxides. Upon photoexcitation of the RuP chromophore, the electron likely initially injects into the conduction band of the shell material. The electron can then localize into the core of SnO_2 and recombination can occur between both the shell and core-localized electrons with the oxidized chromophore.

Based on the staggered conduction band energetics of TiO_2 and SnO_2, we hypothesize that an injected electron will localize in the core metal oxide and recombination with the oxidized dye will proceed via a tunneling mechanism (Figure 5.11). The rate of long-range electron tunneling ($k_{ET}(r)$) is proportional to the square of the electronic coupling between the electron donor and the electron acceptor, which decreases exponentially with donor–acceptor distance r.[225,226,235] The steepness of this decay is described by the tunneling decay constant β, which reflects the tunneling barrier height (Equation 5.1).

$$k_{ET}(r) = k_{ET}(r_0)\exp\left(-\beta(r - r_0)\right) \quad (5.1)$$

Analyzing tunneling processes in core/shell materials is more complex than in the molecular donor-bridge-acceptor systems in which tunneling behavior has been explored extensively.[126,127,226,235,236] For core/shell systems, electrons localized in the core metal oxide tunnel through the shell to recombine with the oxidized chromophore. However, injected electrons trapped in localized acceptor states of the shell material can recombine directly with the oxidized chromophore before transferring to the core. As such, BET dynamics reflect recombination from electron populations localized in the core and trapped in the shell, and kinetic analyses must consider both populations.

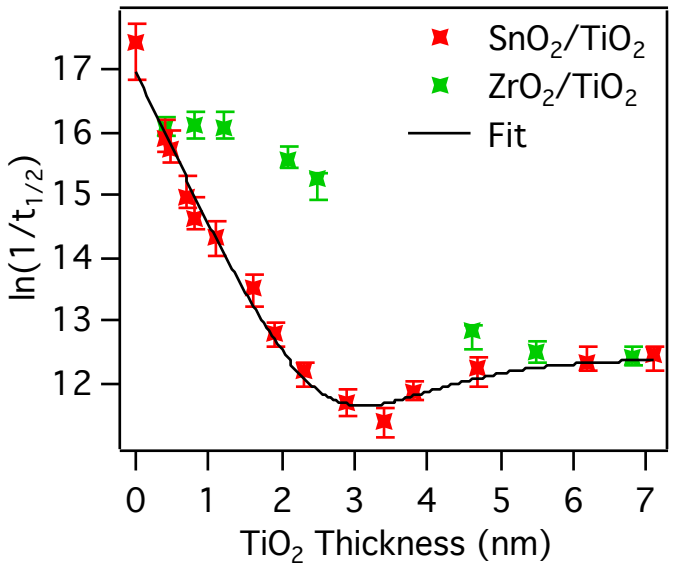

Figure 5.12: Plot of ln(1/ $\tau_{1/2}$) vs. TiO_2 thickness for amorphous SnO_2/TiO_2 films at equal injection yields (red) and ZrO_2/TiO_2 films at equal injection yields (green). The fit models the back electron transfer dynamics with contributions from both tunneling and localized shell recombination.

Figure 5.12 shows the dependence of $\tau_{1/2}$ on amorphous TiO_2 shell thickness for both sensitized SnO_2/TiO_2 and ZrO_2/TiO_2 core/shell films at equal injection yields. If a tunneling mechanism was solely responsible for the recombination in SnO_2/TiO_2 systems, a linear relationship between $\ln(1/\tau_{1/2})$ and the shell thickness would be anticipated, with the negative

slope reflecting the distance attenuation factor β. For thin shells of amorphous TiO_2 (< 3.4 nm) we observe this relationship, indicating that electron tunneling is the predominant pathway for BET. We also considered whether or not this correlation could arise purely from an increase in localized TiO_2 acceptor states formed with increasing shell thickness. However, in comparison to the distance attenuation observed for ZrO_2/TiO_2 control samples, BET in SnO_2/TiO_2 films is attenuated significantly more with increasing shell thickness, indicating that the decrease in BET rate results from other factors. This further supports our assignment of tunneling as the dominant recombination pathway for thin shell materials.

As the TiO_2 shell thickness exceeds 3.4 nm, the rate of BET accelerates and eventually plateaus. This suggests that a second recombination mechanism emerges as the predominant pathway for BET. The rate constant at which distance dependence plateaus is identical to the rate constant of BET in the ZrO_2/TiO_2 control samples at identical shell thicknesses, indicating that the dominant mechanism for recombination in these thick shell materials is diffusion-limited BET from electrons localized in trap states in the TiO_2 shell. A similar trend is observed for the equal pulse energy experiments on SnO_2/TiO_2, with subtle differences in the TiO_2 thickness at which the mechanism changes from a tunneling mechanism to a diffusion-limited BET mechanism (Figure 5.13).

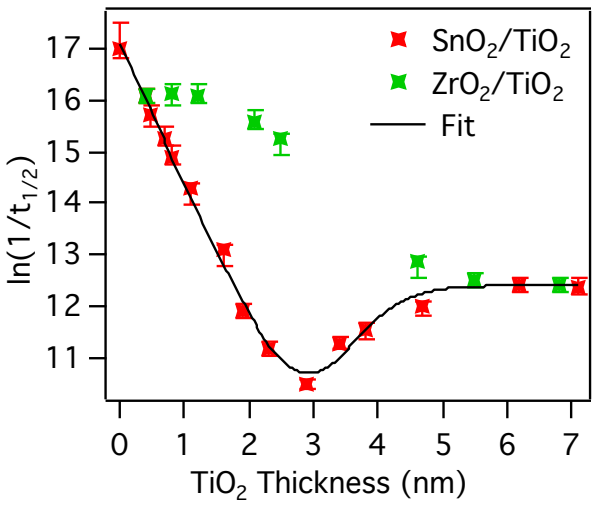

Figure 5.13: Plot of ln(1/ $\tau_{1/2}$) vs. TiO_2 thickness for amorphous SnO_2/TiO_2 films (red) at equal pulse energies and ZrO_2/TiO_2 films (green). The fit models the back electron transfer dynamics with contributions from both tunneling and localized shell recombination ($\beta = 0.27$ $Å^{-1}$ and $X_h = 3.4$ nm).

In order to determine the contribution of tunneling and direct shell recombination mechanisms to the observed rate of recombination for each TiO_2 shell thicknesses, we modeled the data presented in Figure 5.12. Equation 5.2 ($f_{tunnel}(x)$) describes the linear relationship between ln($1/\tau_{1/2}$) and TiO_2 thickness (x) expected for recombination kinetics controlled by electron tunneling, where k_{ET}^0 is back electron transfer rate with no TiO_2 shell present. Recombination between electrons localized in the TiO_2 shell and the oxidized dye can be modeled empirically by the recombination dynamics measured for the ZrO_2/TiO_2 core/shell films. The dependence on TiO_2 thickness for this shell recombination mechanism is described by Equation 5.3 ($f_{shell}(x)$), which was determined from an empirical sigmoidal fit of ln($1/\tau_{1/2}$) vs. TiO_2 thickness for the ZrO_2/TiO_2 system (Fig. 5.14). Each of these mechanisms is then weighted by a function that varies from zero to one and is dependent on TiO_2 thickness, yielding analytical insight into the contribution of each mechanism to the overall back electron transfer dynamics at each shell thickness measured. Linear, exponential

and sigmoidal weighting functions were tested, and we found that complementary sigmoid functions were found to give the best fit to the data (Equation 5.4, $f_{obs}(x)$).

$$f_{tunnel}(x) = -\beta x + ln(k_{ET}^{0}) \tag{5.2}$$

$$f_{shell}(x) = 16.191 + \frac{-3.8042}{1+\exp\,(1.487+(3.264-x))} \tag{5.3}$$

$$f_{obs}(x) = f_{tunnel}(x) * \left(\frac{1}{1+\exp(k(x-X_h))}\right) + f_{shell}(x) * \left(\frac{1}{1+\exp(-k(x-X_h))}\right) \tag{5.4}$$

A decreasing sigmoid is used as the weighting function for the tunneling component (f_{tunnel}), because at small TiO_2 thicknesses, tunneling is the primary mechanism for BET, thus its contribution should start near unity and decrease with increased TiO_2 thickness. The complimentary sigmoid, which has a value close to zero for small TiO_2 thicknesses and a value close to unity at large TiO_2 thicknesses is used as the weighting function for the shell component (f_{shell}). The intersection of these sigmoidal weighting functions is defined by the parameter X_h, which is the TiO_2 thickness at which the dominant mechanism for BET switches (Figure 5.15).

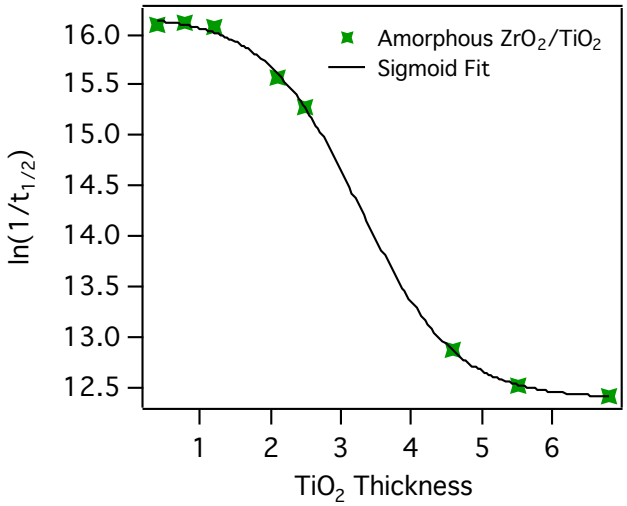

Figure 5.14: Plot of ln(1/ $\tau_{1/2}$) vs. TiO_2 thickness for amorphous ZrO_2/TiO_2. The fit empirically models the back electron transfer dynamics from localized shell recombination with a sigmoid function as follows: $f_{shell}(x) = 16.191 + \frac{-3.804}{1+\exp(1.487(3.264-x))}$

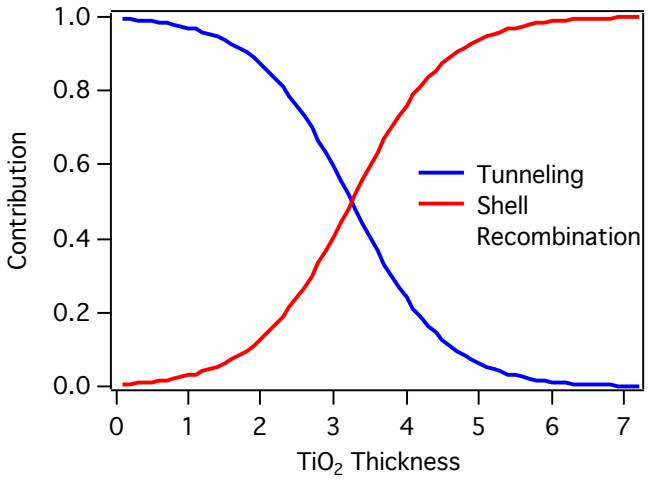

Figure 5.15: Sigmoidal weighting functions from the analysis of the equal injection yield data (β = 0.25 $Å^{-1}$ and X_h = 3.2 nm).

Fitting the data presented in Figure 5.12 to Equation 5.3, values of β = 0.25 $Å^{-1}$ and X_h = 3.2 nm were determined for the RuP sensitized SnO_2/TiO_2 core/shell series. This same analysis was applied to the equal pulse energy experiments and very similar β and X_h values were obtained (0.27 $Å^{-1}$ and 3.4 nm, respectively; Figure 5.13). Our value for β differs slightly from that previously reported for ITO/TiO_2 systems with amorphous shells (β = 0.4 $Å^{-1}$).[127] Since the value for β is proportional to the energy barrier for electron tunneling, this difference in β values likely reflects the different conduction band edge energies of the different core materials (SnO_2 compared to ITO) which influence the effective tunneling barrier.

Hupp and coworkers recently reported that very thin (<0.5 nm) TiO_2 layers on SnO_2 in DSSC devices led to a β value of 0.5 $Å^{-1}$ for electron tunneling to a redox mediator in solution.[126] Considering that a Ti−O bond is 2 Å for crystalline TiO_2, it could be possible that

tunneling proceeded through molecular Ti−O bridges as opposed to a TiO_2 lattice.[237] Moreover, in molecular systems, covalent bonding promotes charge tunneling and smaller β values. Therefore, in our system, where tunneling current flows into the ground state of a bound oxidized chromophore, our measured β value of 0.25 $Å^{-1}$ could result from reduced tunneling barriers for charge transport into and out of the TiO_2 film.[225,226,238–240]

5.4.2. Recombination Dynamics in Annealed Core/Shell Systems

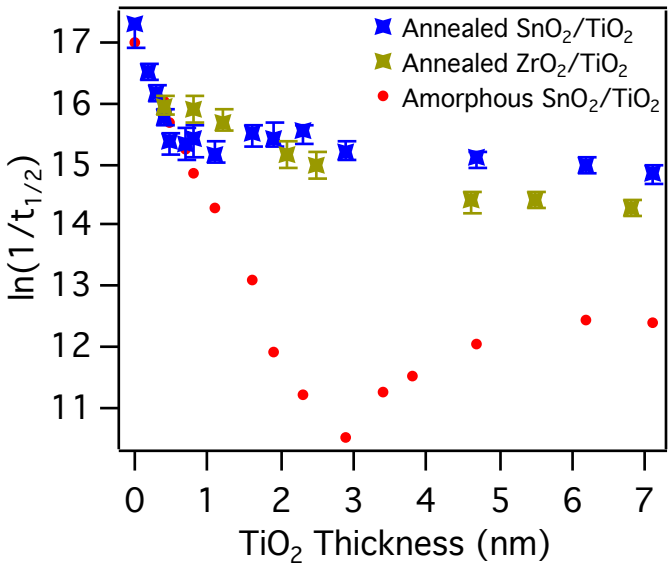

Figure 5.16: Plot of ln(1/ $\tau_{1/2}$) vs. TiO_2 thickness for annealed SnO_2/TiO_2 films (red) and annealed ZrO_2/TiO_2 films (green)

We also examined the effects of annealing on the BET dynamics in SnO_2/TiO_2–RuP systems. Figure 5.16 shows the dependence of $\tau_{1/2}$ on TiO_2 thickness, for both annealed SnO_2/TiO_2 and annealed ZrO_2/TiO_2 systems. For the annealed SnO_2/TiO_2 samples we see an initial decrease in the rate of BET with increased TiO_2 thickness up to 0.5 nm. With shells thicker than 0.5 nm, the BET rate is relatively independent of shell thickness. Additionally, upon annealing the ZrO_2/TiO_2 films, the rate of BET decreases slightly with increased TiO_2

thickness, then becomes relatively independent of shell thickness. The stark similarity between the dynamics of the annealed SnO_2/TiO_2 samples and annealed ZrO_2/TiO_2 control samples, along with the dramatic differences between the distance-dependent behavior of the annealed vs. amorphous samples, suggests that the injected electrons remain localized in the TiO_2 shell for TiO_2 thicknesses greater than 0.5 nm in the annealed samples.

Grätzel and coworkers have examined the effects of annealed TiO_2 deposited on FTO via ALD.[220] They found that annealing films at 500 °C led to delamination of the titania film from the FTO surface. If delamination of the TiO_2 shell from the SnO_2 core surface occurs in our system and is significant enough to sever the electronic communication between the two oxides, electrons would reside solely in TiO_2 shell, leading to nearly identical BET dynamics for the SnO_2/TiO_2 and ZrO_2/TiO_2 systems. This is consistent with the BET dynamics we observe.

The initial decrease in the BET rate for TiO_2 shells less than 0.5 nm thick may arise from the passivation of SnO_2 surface states, rather than electron tunneling from core-localized electrons.[47,196] Upon annealing these films, it is possible that pinhole defects in the TiO_2 shell form very thin TiO_2 shells, exposing some bare SnO_2 sites for chromophore binding. This would cause the observed back electron transfer to be a convolution of recombination between electrons injected directly into the SnO_2 cores and electrons injected to the TiO_2 shells. As the TiO_2 thickness increases, pinholes are less likely to form in the annealed samples and chromophores will bind solely to the TiO_2 shell surface. Upon excitation, injected electrons localize in the TiO_2 shells, and due to delamination between the core and shell material at their interface, electrons remain localized in the TiO_2 shell, as discussed above.

5.5. Conclusions

Interfacial charge recombination dynamics were investigated using transient absorption spectroscopy for amorphous and annealed SnO_2/TiO_2 core/shell systems in order to elucidate the effect of shell thickness on BET dynamics. Charge recombination in SnO_2/TiO_2 films with amorphous shells proceeds via two competitive mechanisms that depend on the shell thickness. For shell thicknesses between 0 and 3.4 nm, BET proceeds predominantly by a tunneling mechanism, with β=0.25 $Å^{-1}$. For shell thicknesses greater than 3.4 nm, the primary recombination mechanism involves electrons localized the TiO_2 shell. After annealing, the SnO_2/TiO_2 films display very different BET dynamics than their amorphous counterparts. The BET rate for the annealed films decreases with increasing shell thickness for TiO_2 thicknesses up to 0.5 nm. This decrease is attributed to the elimination of pinhole defects as the TiO_2 thickness increases. With TiO_2 shells thicker than 0.5 nm, the rate of BET in the annealed films is independent of TiO_2 thickness and identical to the ZrO_2/TiO_2 core/shell samples, suggesting that the core/shell interface is perturbed in the annealing process. Together, these results indicate that there is an ideal shell thickness to suppress BET in sensitized core/shell films and show that electron transfer dynamics in these materials are sensitive to the core/shell interface. Consideration of these factors will help advance these emerging materials for DSSC and DSPEC applications.

REFERENCES

(1) Administration, U. S. E. I. Annual Energy Outlook 2015. *US Dep. Energy* **2015**.

(2) Nocera, D. G.; Nash, M. P. Powering the Planet: Chemical Challenges in Solar Energy Utilization. *Proc. Natl. Acad. Sci. U. S. A.* **2007**, *104* (42), 20142.

(3) Tsao, J.; Lewis, N.; Crabtree, G. Solar FAQs. *US Dep. Energy* **2006**, 1–24.

(4) Norby, R. J.; Luo, Y. Evaluating Ecosystem Responses to Rising Atmospheric CO2 and Global Warming in a Multi-Factor World. *New Phytol.* **2004**, *162* (2), 281–293.

(5) Doney, S. C.; Fabry, V. J.; Feely, R. a; Kleypas, J. a. Ocean Acidification: The Other CO 2Problem. *Ann. Rev. Mar. Sci.* **2009**, *1* (1), 169–192.

(6) Cox, P. M.; Betts, R. a; Jones, C. D.; Spall, S. a; Totterdell, I. J. Acceleration of Global Warming due to Carbon-Cycle Feedbacks in a Coupled Climate Model. *Nature* **2000**, *408* (6809), 184–187.

(7) Lüthi, D.; Le Floch, M.; Bereiter, B.; Blunier, T.; Barnola, J.-M.; Siegenthaler, U.; Raynaud, D.; Jouzel, J.; Fischer, H.; Kawamura, K.; et al. High-Resolution Carbon Dioxide Concentration Record 650,000-800,000 Years before Present. *Nature* **2008**, *453* (7193), 379–382.

(8) France, R. M.; Geisz, J. F.; Garcia, I.; Steiner, M. a.; McMahon, W. E.; Friedman, D. J.; Moriarty, T. E.; Osterwald, C.; Scott Ward, J.; Duda, A.; et al. Quadruple-Junction Inverted Metamorphic Concentrator Devices. *IEEE J. Photovoltaics* **2015**, *5* (1), 432–437.

(9) Blankenship, R. E.; Tiede, D. M.; Barber, J.; Brudvig, G. W.; Fleming, G.; Ghirardi, M.; Gunner, M. R.; Junge, W.; Kramer, D. M.; Melis, A.; et al. Comparing Photosynthetic and Photovoltaic Efficiencies and Recognizing the Potential for Improvement. *Science* **2011**, *332* (6031), 805–809.

(10) Song, W.; Chen, Z.; Brennaman, M. K.; Concepcion, J. J.; Patrocinio, A. O. T.; Murakami Iha, N. Y.; Meyer, T. J. Making Solar Fuels by Artificial Photosynthesis. *Pure Appl. Chem.* **2011**, *83* (4), 749–768.

(11) Zhu, X. G.; Long, S. P.; Ort, D. R. Improving Photosynthetic Efficiency for Greater Yield. *Annu Rev Plant Biol* **2010**, *61*, 235–261.

(12) Wijffels, R. H.; Barbosa, M. J. An Outlook on Microalgal Biofuels. *Science* **2010**, *329* (5993), 796–799.

(13) Umena, Y.; Kawakami, K.; Shen, J.-R.; Kamiya, N. Crystal Structure of Oxygen-Evolving Photosystem II at a Resolution of 1.9 Å. *Nature* **2011**, *473* (7345), 55–60.

(14) Ferreira, K. N.; Iverson, T. M.; Maghlaoui, K.; Barber, J. Architecture of the Photosynthetic Oxygen-Evolving Center. *Science (80-.).* **2004**, *303*, 1831–1839.

(15) Green, M. A. The Path to 25% Silicon Solar Cell Efficiency: History of Silicon Cell Evolution. *Prog. Photovolt Res. Appl.* **2009**, *17*, 183–189.

(16) Feldman, D.; Barbose, G.; James, T.; Weaver, S.; Fu, R.; Davidson, C. Photovoltaic System Pricing Trends 2014 Edition. *US Dep. Energy* **2014**, 1–32.

(17) Kaelin, M.; Rudmann, D.; Tiwari, a. N. Low Cost Processing of CIGS Thin Film Solar Cells. *Sol. Energy* **2004**, *77* (6), 749–756.

(18) Kalowekamo, J.; Baker, E. Estimating the Manufacturing Cost of Purely Organic Solar Cells. *Sol. Energy* **2009**, *83* (8), 1224–1231.

(19) National Renewable Energy Labratory. Best Reseach-Cell Efficiencies. *US Dep. Energy* **2016**.

(20) Grätzel, M. Dye-Sensitized Solar Cells. *Journal of Photochemistry and Photobiology C: Photochemistry Reviews*. 2003, pp 145–153.

(21) Hagfeldt, A.; Boschloo, G.; Sun, L.; Kloo, L.; Pettersson, H. Dye-Sensitized Solar Cells. *Chem. Rev.* **2010**, *110*, 6595–6663.

(22) Rho, W.; Jeon, H.; Kim, H.; Chung, W.; Suh, S.; Jun, B. Recent Progress in Dye-Sensitized Solar Cells (DSSC) for Improving Efficiency : TiO 2 Nanotube Arrays in Active Layer. *J. Nanomater.* **2015**, *2015*.

(23) Durrant, J. R.; Haque, S. a.; Palomares, E. Towards Optimisation of Electron Transfer Processes in Dye Sensitised Solar Cells. *Coord. Chem. Rev.* **2004**, *248* (13-14), 1247–1257.

(24) Listorti, A.; Regan, B. O.; Durrant, J. R. Electron Transfer Dynamics in Dye-Sensitized Solar Cells. *Chem. Mater.* **2011**, 3381–3399.

(25) Ning, Z.; Fu, Y.; Tian, H. Improvement of Dye-Sensitized Solar Cells: What We Know and What We Need to Know. *Energy & Environmental Science*. 2010, p 1170.

(26) Bisquert, J.; Cahen, D.; Hodes, G.; Ru, S.; Zaban, A.; Gan, R. Physical Chemical Principles of Photovoltaic Conversion with Nanoparticulate, Mesoporous Dye-Sensitized Solar Cells. *J. Phys. Chem. B* **2004**, *108* (24), 8106–8118.

(27) Hagfeldtt, A.; Gratzel, M. Light-Induced Redox Reactions in Nanocrystalline Systems. *Chem. Rev.* **1995**, *95* (1), 49–68.

(28) Nayak, A.; Knauf, R. R.; Hanson, K.; Alibabaei, L.; Concepcion, J. J.; Ashford, D. L.; Dempsey, J. L.; Meyer, T. J. Synthesis and Photophysical Characterization of Porphyrin and porphyrin–Ru(ii) Polypyridyl Chromophore–catalyst Assemblies on Mesoporous Metal Oxides. *Chem. Sci.* **2014**, *5* (8), 3115.

(29) Milot, R. L.; Moore, G. F.; Crabtree, R. H.; Brudvig, G. W.; Schmuttenmaer, C. a. Electron Injection Dynamics from Photoexcited Porphyrin Dyes into SnO 2 and TiO2 Nanoparticles. *J. Phys. Chem. C* **2013**, *117* (42), 21662–21670.

(30) Imahori, H.; Umeyama, T. Donor-Acceptor Nanoarchitecture on Semiconducting Electrodes for Solar Energy Conversion. *J. Phys. Chem. C* **2009**, *113* (21), 9029–9039.

(31) Hu, K.; Robson, K. C. D.; Berlinguette, C. P.; Meyer, G. J. Donor-??-Acceptor Organic Hybrid TiO2 Interfaces for Solar Energy Conversion. In *Thin Solid Films*; 2014; Vol. 560, pp 49–54.

(32) Tachibana, Y.; Haque, S. a.; Mercer, I. P.; Durrant, J. R.; Klug, D. R. Electron Injection and Recombination in Dye Sensitized Nanocrystalline Titanium Dioxide Films: A Comparison of Ruthenium Bipyridyl and Porphyrin Sensitizer Dyes. *J. Phys. Chem. B* **2000**, *104* (6), 1198–1205.

(33) Kamat, P. V. Quantum Dot Solar Cells. The next Big Thing in Photovoltaics. *J. Phys. Chem. Lett.* **2013**, *4* (6), 908–918.

(34) Carey, G. H.; Abdelhady, A. L.; Ning, Z.; Thon, S. M.; Bakr, O. M.; Sargent, E. H. Colloidal Quantum Dot Solar Cells. *Chem. Rev.* **2015**, *115* (23), 12732–12763.

(35) Bera, D.; Qian, L.; Tseng, T. K.; Holloway, P. H. Quantum Dots and Their Multimodal Applications: A Review. *Materials (Basel).* **2010**, *3* (4), 2260–2345.

(36) Lana-villarreal, T.; Lutz, T.; Haque, S. A. Sensitization of TiO 2 with PbSe Quantum Dots by SILAR: How Mercaptophenol Improves Charge Separation. *J. Phys. Chem. Lett.* **2012**, *3*, 3367–3372.

(37) Amelia, M.; Avellini, T.; Monaco, S.; Impellizzeri, S.; Yildiz, I.; Raymo, F. M.; Credi, A. Redox Properties of CdSe and CdSe–ZnS Quantum Dots in Solution. *Pure Appl. Chem.* **2010**, *83* (1), 1–8.

(38) Evans, C. M.; Cass, L. C.; Knowles, K. E.; Tice, D. B.; Chang, R. P. H.; Weiss, E. a. Review of the Synthesis and Properties of Colloidal Quantum Dots: The Evolving Role of Coordinating Surface Ligands. *J. Coord. Chem.* **2012**, *65* (13), 2391–2414.

(39) Jasieniak, J.; Smith, L.; Embden, J. Van; Mulvaney, P.; Califano, M. Re-Examination of the Size Dependent Absorption Properties of CdSe Quantum Dots. *J. Phys. Chem. C* **2009**, *113*, 19468–19474.

(40) Yu, W. W.; Qu, L.; Guo, W.; Peng, X. Experimental Determination of the Extinction Coefficient of CdTe , CdSe , and CdS Nanocrystals Experimental Determination of the Extinction Coefficient of CdTe , CdSe , and CdS Nanocrystals. *Chem. Mater.* **2003**, *125* (17), 2854–2860.

(41) Rossetti, R.; Nakahara, S.; Brus, L. Quantum Size Effects in the Redox Potentials, Resonance Raman Spectra, and Electronic Spectra of CdS Crystallites in Aqueous Solution. *J. Chem. Phys.* **1983**, *79* (1983), 1086–1088.

(42) Leatherdale, C. a.; Woo, W.-K.; Mikulec, F. V.; Bawendi, M. G. On the Absorption Cross Section of CdSe Nanocrystal Quantum Dots. *J. Phys. Chem. B* **2002**, *106* (31), 7619–7622.

(43) Karel Čapek, R.; Moreels, I.; Lambert, K.; De Muynck, D.; Zhao, Q.; Van Tomme, A.; Vanhaecke, F.; Hens, Z. Optical Properties of Zincblende Cadmium Selenide Quantum Dots. *J. Phys. Chem. C* **2010**, *114* (14), 6371–6376.

(44) Jovanovski, V.; González-Pedro, V.; Giménez, S.; Azaceta, E.; Cabañero, G.; Grande, H.; Tena-Zaera, R.; Mora-Seró, I.; Bisquert, J. A Sulfide/polysulfide-Based Ionic Liquid Electrolyte for Quantum Dot-Sensitized Solar Cells. *J. Am. Chem. Soc.* **2011**, *133* (50), 20156–20159.

(45) Ardo, S.; Meyer, G. J. Photodriven Heterogeneous Charge Transfer with Transition-Metal Compounds Anchored to TiO2 Semiconductor Surfaces. *Chem. Soc. Rev.* **2009**, *38* (1), 115–164.

(46) Norris, M. R.; Concepcion, J. J.; Glasson, C. R. K.; Fang, Z.; Lapides, A. M.; Ashford, D. L.; Templeton, J. L.; Meyer, T. J. Synthesis of Phosphonic Acid-Derivatized Bipyridine Ligands and Their Ruthenium Complexes. *Inorg. Chem.* **2013**, *52*, 12492–12501.

(47) Prasittichai, C.; Hupp, J. T. Surface Modification of SnO 2 Photoelectrodes in Dye-Sensitized Solar Cells: Significant Improvements in Photovoltage via Al 2 O 3 Atomic Layer Deposition. *J. Phys. Chem. Lett.* **2010**, *1* (10), 1611–1615.

(48) Koumura, N.; Wang, Z. S.; Mori, S.; Miyashita, M.; Suzuki, E.; Hara, K. Alkyl-Functionalized Organic Dyes for Efficient Molecular Photovoltaics. *J. Am. Chem. Soc.* **2006**, *128* (44), 14256–14257.

(49) Becker, M. A.; Radich, J. G.; Bunker, B. A.; Kamat, P. V. How Does a SILAR CdSe Film Grow? Tuning the Deposition Steps to Suppress Interfacial Charge Recombination in Solar Cells. *J. Phys. Chem. Lett.* **2014**, *5* (9), 1575–1582.

(50) Talapin, D. V.; Lee, J. S.; Kovalenko, M. V.; Shevchenko, E. V. Prospects of Colloidal Nanocrystals for Electronic and Optoelectronic Applications. *Chem. Rev.* **2010**, *110* (1), 389–458.

(51) Kairdolf, B. A.; Smith, A. M.; Stokes, T. H.; Wang, M. D.; Young, A. N.; Nie, S. Semiconductor Quantum Dots for Bioimaging and Biodiagnostic Applications. *Annu. Rev. Anal. Chem.* **2013**, *6*, 143–162.

(52) Zabet-khosousi, A.; Dhirani, A. Charge Transport in Nanoparticle Assemblies. *Chem. Rev.* **2008**, *108*, 4072–4124.

(53) Kamat, P. V. Meeting the Clean Energy Demand : Nanostructure Architectures for Solar Energy. *J. Phys. Chem. C* **2007**, *111*, 2834–2860.

(54) Morris-Cohen, A. J.; Malicki, M.; Peterson, M. D.; Slavin, J. W. J.; Weiss, E. a. Chemical, Structural, and Quantitative Analysis of the Ligand Shells of Colloidal Quantum Dots. *Chem. Mater.* **2013**, *25* (8), 1155–1165.

(55) Green, M. The Nature of Quantum Dot Capping Ligands. *J. Mater. Chem.* **2010**, *20* (28), 5797–5809.

(56) Evans, C. M.; Cass, L. C.; Knowles, K. E.; Tice, D. B.; Chang, R. P. H.; Weiss, E. a. Review of the Synthesis and Properties of Colloidal Quantum Dots: The Evolving Role of Coordinating Surface Ligands. *J. Coord. Chem.* **2012**, *65* (13), 2391–2414.

(57) Lemon, C. M.; Curtin, P. N.; Somers, R. C.; Greytak, A. B.; Lanning, R. M.; Jain, R. K.; Bawendi, M. G.; Nocera, D. G. Metabolic Tumor Profiling with pH, Oxygen, and Glucose Chemosensors on a Quantum Dot Scaffold. *Inorg. Chem.* **2014**, *53* (4), 1900–1915.

(58) Somers, R. C.; Bawendi, M. G.; Nocera, D. G.; Bawendi, P. M. G. CdSe Nanocrystal Based Chem- / Bio- Sensors. *Chem. Soc. Rev.* **2007**, No. September 2006, 579–591.

(59) Somers, R. C.; Snee, P. T.; Bawendi, M. G.; Nocera, D. G. Energy Transfer of CdSe/ZnS Nanocrystals Encapsulated with Rhodamine-Dye Functionalized Poly(acrylic Acid). *J. Photochem. Photobiol. A Chem.* **2012**, *248*, 24–29.

(60) Liu, W.; Greytak, A. B.; Lee, J.; Wong, C. R.; Park, J.; Marshall, L. F.; Jiang, W.; Curtin, P. N.; Ting, A. Y.; Nocera, D. G.; et al. Compact Biocompatible Quantum Dots via RAFT-Mediated Synthesis of Imidazole-Based Random Copolymer Ligand. *J. Am. Chem. Soc.* **2010**, *132* (2), 472–483.

(61) McLaurin, E. J.; Greytak, A. B.; Bawendi, M. G.; Nocera, D. G. Two-Photon Absorbing Nanocrystal Sensors for Ratiometric Detection of Oxygen. *J. Am. Chem. Soc.* **2009**, *131* (36), 12994–13001.

(62) Tseng, H.-W.; Wilker, M. B.; Damrauer, N. H.; Dukovic, G. Charge Transfer Dynamics between Photoexcited CdS Nanorods and Mononuclear Ru Water-Oxidation Catalysts. *J. Am. Chem. Soc.* **2013**, *135* (9), 3383–3386.

(63) Wilker, M. B.; Shinopoulos, K. E.; Brown, K. A.; Mulder, D. W.; King, P. W.; Dukovic, G. Electron Transfer Kinetics in CdS Nanorod–[FeFe]-Hydrogenase Complexes and Implications for Photochemical H 2 Generation. *J. Am. Chem. Soc.* **2014**, *136* (11), 4316–4324.

(64) Weinberg, D. J.; Khademi, Z.; Malicki, M.; Marder, S. R.; Weiss, E. a. Microsecond Charge Recombination Lifetimes in Complexes of CdS Quantum Dots and Organic Hole Acceptors Enabled by Hole-Hopping within the Ligand Shell. *J. Am. Chem. Soc.* **2014**, *136*, 14513–14518.

(65) Frederick, M. T.; Weiss, E. a. Relaxation of Exciton Confinement in CdSe Quantum Dots by Modification with a Conjugated Dithiocarbamate Ligand. *ACS Nano* **2010**, *4* (6), 3195–3200.

(66) Tagliazucchi, M.; Tice, D. B.; Sweeney, C. M.; Morris-Cohen, A. J.; Weiss, E. A. Ligand-Controlled Rates of Photoinduced Electron Transfer in Hybrid CdSe Nanocrystal/Poly(viologen) Films. *ACS Nano* **2011**, *5* (12), 9907–9917.

(67) Morris-Cohen, A. J.; Aruda, K. O.; Rasmussen, A. M.; Canzi, G.; Seideman, T.; Kubiak, C. P.; Weiss, E. A. Controlling the Rate of Electron Transfer between a Quantum Dot and a Tri-Ruthenium Molecular Cluster by Tuning the Chemistry of the Interface. *Phys. Chem. Chem. Phys.* **2012**, *14* (40), 13794–13801.

(68) Malicki, M.; Knowles, K. E.; Weiss, E. A. Gating of Hole Transfer from Photoexcited PbS Quantum Dots to Aminoferrocene by the Ligand Shell of the Dots. *Chem. Commun. (Camb).* **2013**, *49* (39), 4400–4402.

(69) Knowles, K. E.; Malicki, M.; Weiss, E. A. Dual-Time Scale Photoinduced Electron Transfer from PbS Quantum Dots to a Molecular Acceptor. *J. Am. Chem. Soc.* **2012**, *134* (30), 12470–12473.

(70) Weiss, E. A. Organic Molecules as Tools to Control the Growth, Surface Structure, and Redox Activity of Colloidal Quantum Dots. *Acc. Chem. Res.* **2013**, *46* (11), 2607–2615.

(71) Mann, J. R.; Watson, D. F. Adsorption of CdSe Nanoparticles to Thiolated TiO 2 Surfaces: Influence of Intralayer Disulfide Formation on CdSe Surface Coverage. *Langmuir* **2007**, *23* (22), 10924–10928.

(72) Dibbell, R. S.; Soja, G. R.; Hoth, R. M.; Watson, D. F. Photocatalytic Patterning of Monolayers for the Site-Selective Deposition of Quantum Dots onto TiO2 Surfaces. *Langmuir* **2007**, *23* (6), 3432–3439.

(73) Robel, I.; Subramanian, V.; Kuno, M.; Kamat, P. V. Quantum Dot Solar Cells. Harvesting Light Energy with CdSe Nanocrystals Molecularly Linked to Mesoscopic TiO2 Films. *J. Am. Chem. Soc.* **2006**, No. 19, 2385–2393.

(74) Kern, M. E.; Watson, D. F. Linker-Assisted Attachment of Cdse Quantum Dots to TiO2: Time- and Concentration-Dependent Adsorption, Agglomeration, and Sensitized Photocurrent. *Langmuir* **2014**, *30* (44), 13293–13300.

(75) Kern, M. E.; Watson, D. F. Influence of Solvation and the Persistence of Adsorbed Linkers on the Attachment of CdSe Quantum Dots to TiO 2 via Linker-Assisted Assembly. *Langmuir* **2012**, *28* (44), 15598–15605.

(76) Dibbell, R. S.; Youker, D. G.; Watson, D. F. Excited-State Electron Transfer from CdS Quantum Dots to TiO2 Nanoparticles via Molecular Linkers with Phenylene Bridges. *J. Phys. Chem. C* **2009**, *113* (43), 18643–18651.

(77) Dibbell, R. S.; Watson, D. F. Distance-Dependent Electron Transfer in Tethered Assemblies of CdS Quantum Dots and TiO2 Nanoparticles. *J. Phys. Chem. C* **2009**, *113* (22), 13511–13519.

(78) Choi, H.; Santra, P. K.; Kamat, P. V. Synchronized Energy and Electron Transfer Processes in Covalently Linked CdSe-Squaraine Dye-TiO2 Light Harvesting Assembly. *ACS Nano* **2012**, *6* (6), 5718–5726.

(79) Owen, J. The Coordination Chemistry of Nanocrystal Surfaces. *Science (80-.).* **2015**, *347* (6222), 615–616.

(80) Song, W.; Luo, H.; Hanson, K.; Concepcion, J. J.; Brennaman, M. K.; Meyer, T. J. Visualization of Cation Diffusion at the TiO2 Interface in Dye Sensitized Photoelectrosynthesis Cells (DSPEC). *Energy Environ. Sci.* **2013**.

(81) Song, W.; Chen, Z.; Glasson, C. R. K.; Hanson, K.; Luo, H.; Norris, M. R.; Ashford, D. L.; Concepcion, J. J.; Brennaman, M. K.; Meyer, T. J. Interfacial Dynamics and Solar Fuel Formation in Dye-Sensitized Photoelectrosynthesis Cells. *Chemphyschem* **2012**, *13* (12), 2882–2890.

(82) Song, W.; Ito, A.; Binstead, R. a.; Hanson, K.; Luo, H.; Brennaman, M. K.; Concepcion, J. J.; Meyer, T. J. Accumulation of Multiple Oxidative Equivalents at a Single Site by Cross-Surface Electron Transfer on TiO2. *J. Am. Chem. Soc.* **2013**, *135* (31), 11587–11594.

(83) Gratzel, M. Photoelectrochemical Cells. *Nature* **2001**, *414* (November), 338.

(84) Alibabaei, L.; Brennaman, M. K.; Norris, M. R.; Kalanyan, B.; Song, W.; Losego, M. D.; Concepcion, J. J.; Binstead, R. a; Parsons, G. N.; Meyer, T. J. Solar Water

Splitting in a Molecular Photoelectrochemical Cell. *Proc. Natl. Acad. Sci. U. S. A.* **2013**, *110* (50), 20008–20013.

(85) Bedja, I.; Hotchandani, S.; Kamat, P. Preparation and Photoelectrochemical Characterization of Thin. *J. Phys. Chem.* **1994**, *98*, 4133–4140.

(86) Alibabaei, L.; Sherman, B. D.; Norris, M. R.; Brennaman, M. K.; Meyer, T. J. Visible Photoelectrochemical Water Splitting into H 2 and O 2 in a Dye-Sensitized Photoelectrosynthesis Cell. *Proc. Natl. Acad. Sci.* **2015**, *3* (23), 201506111.

(87) Yamamoto, M.; Wang, L.; Li, F.; Fukushima, T.; Tanaka, K.; Sun, L.; Imahori, H. Visible Light-Driven Water Oxidation Using a Covalently-Linked Molecular Catalyst–sensitizer Dyad Assembled on a TiO_2 Electrode. *Chem. Sci.* **2016**, *00*, 1–10.

(88) Li, F.; Fan, K.; Xu, B.; Gabrielsson, E.; Daniel, Q.; Li, L.; Sun, L. An Organic Dye-Sensitized Tandem Photoelectrochemical Cell for Light Driven Water Splitting. *J. Am. Chem. Soc.* **2015**, No. i, 150701170924000.

(89) Yu, Z.; Li, F.; Sun, L. Recent Advances in Dye-Sensitized Photoelectrochemical Cells for Solar Hydrogen Production Based on Molecular Components. *Energy Environ. Sci.* **2015**, *8* (3), 760–775.

(90) Zhao, Y.; Swierk, J. R.; Megiatto, J. D.; Sherman, B.; Youngblood, W. J.; Qin, D. Improving the Efficiency of Water Splitting in Dye-Sensitized Solar Cells by Using a Biomimetic Electron Transfer Mediator. *Proc. Natl. Acad. Sci.* **2012**, *109* (39), 15612–15616.

(91) Gratzel, M. Dye-Sensitized Solar Cells. *J. Photochem. Photobiol. C Photochem. Rev.* **2003**, *4* (2), 145–153.

(92) Marcus, R. a. On the Theory of Oxidation-Reduction Reactions Involving Electron Transfer. I. *J. Chem. Phys.* **1956**, *24* (5), 966.

(93) Lyon, L. A.; Hupp, J. T. Energetics of the Nanocrystalline Titanium Dioxide / Aqueous Solution Interface : Approximate Conduction Band Edge Variations between H 0) -10 and H -) + 26. *J. Phys. Chem. B* **1999**, *103*, 4623–4628.

(94) Hasselmann, G. M.; Meyer, G. J. Diffusion-Limited Interfacial Electron Transfer with Large Apparent Driving Forces. *J. Phys. Chem. B* **1999**, *103* (36), 7671–7675.

(95) Kelly, C. A.; Farzad, F.; Thompson, D. W.; Stipkala, J. M.; Meyer, G. J. Cation-Controlled Interfacial Charge Injection in Sensitized Nanocrystalline TiO 2. *Langmuir* **1999**, *15* (7), 7047–7054.

(96) Haque, S. a.; Tachibana, Y.; Klug, D. R.; Durrant, J. R. Charge Recombination Kinetics in Dye-Sensitized Nanocrystalline Titanium Dioxide Films under Externally Applied Bias. *J. Phys. Chem. B* **1998**, *102* (10), 1745–1749.

(97) Kuciauskas, D.; Freund, M. S.; Gray, H. B.; Winkler, J. R.; Lewis, N. S. Electron Transfer Dynamics in Nanocrystalline Titanium Dioxide Solar Cells Sensitized with Ruthenium or Osmium Polypyridyl Complexes. *J. Phys. Chem. B* **2001**, *105*, 392–403.

(98) O'Regan, B.; Moser, J.; Anderson, M.; Graetzel, M. Vectorial Electron Injection into Transparent Semiconductor Membranes and Electric Field Effects on the Dynamics of Light-Induced Charge Separation. *J. Phys. Chem.* **1990**, *94* (24), 8720–8726.

(99) Yan, S. G.; Hupp, J. T. Semiconductor-Based Interfacial Electron-Transfer Reactivity: Decoupling Kinetics from pH-Dependent Band Energetics in a Dye-Sensitized Titanium Dioxide/Aqueous Solution System. *J. Phys. Chem.* **1996**, *100* (17), 6867–6870.

(100) Green, A. N. M.; Palomares, E.; Haque, S. a; Kroon, J. M.; Durrant, J. R. Charge Transport versus Recombination in Dye-Sensitized Solar Cells Employing Nanocrystalline TiO2 and SnO2 Films. *J. Phys. Chem. B* **2005**, *109* (25), 12525–12533.

(101) Dang, X.; Hupp, J. T. Interfacial Charge-Transfer Pathways : Evidence for Marcus-Type Inverted Electron Transfer in Metal Oxide Semiconductor / Inorganic Dye Systems. *J. Am. Chem. Soc.* **1999**, *121* (12), 8399–8400.

(102) Clifford, J.; Palomares, E.; Nazeeruddin, M.; Graetzel, M.; Nelson, J.; Li, X.; Long, N.; Durrant, J. R. Molecular Control of Recombination Dynamics in Dye-Sensitized Nanocrystalline TiO2 Films: Free Energy vs Distance Dependence. *J. Am. Chem. Soc.* **2004**, *126* (16), 5225–5233.

(103) Brigham, E. C.; Meyer, G. J. Ostwald Isolation to Determine the Reaction Order for TiO 2(e-)|S+↔ TiO2|S Charge Recombination at Sensitized TiO2 Interfaces. *J. Phys. Chem. C* **2014**, *118* (15), 7886–7893.

(104) Tiwana, P.; Docampo, P.; Johnston, M. B.; Snaith, H. J.; Herz, L. M. Electron Mobility and Injection Dynamics in Mesoporous ZnO SnO2, and TiO2 Films Used in Dye-Sensitized Solar Cells. *ACS Nano* **2011**, No. 6, 5158–5166.

(105) Hendry, E.; Koeberg, M.; Regan, B. O.; Bonn, M. Local Field Effects on Electron Transport in Nanostructured TiO 2 Revealed by Terahertz Spectroscopy. *Nano Lett.* **2006**, *6*, 755–759.

(106) Ishiguro, K.; Sasaki, T.; Arai, T.; Imai, I. Optical and Electrical Properties of Tin Oxide Films. *J. Phys. Soc. Jpn.* **1958**, *13*, 296–304.

(107) Asbury, J. B.; Hao, E.; Wang, Y.; Ghosh, H. N.; Lian, T. Ultrafast Electron Transfer Dynamics from Molecular Adsorbates to Semiconductor. *J. Phys. Chem. B* **2001**, *105*, 4545–4557.

(108) Bauer, C.; Boschloo, G.; Mukhtar, E.; Hagfeldt, A. Ultrafast Studies of Electron Injection in Ru Dye Sensitized SnO 2 Nanocrystalline Thin Film. *Int. J. Photoenergy* **2002**, *4*, 2–5.

(109) Ashford, D. L.; Stewart, D. J.; Glasson, C. R.; Binstead, R. a.; Harrison, D. P.; Norris, M. R.; Concepcion, J. J.; Fang, Z.; Templeton, J. L.; Meyer, T. J. An Amide-Linked Chromophore-Catalyst Assembly for Water Oxidation. *Inorg. Chem.* **2012**, *51* (12), 6428–6430.

(110) Song, W.; Glasson, C. R. K.; Luo, H.; Hanson, K.; Brennaman, M. K.; Concepcion, J. J.; Meyer, T. J. Photoinduced Stepwise Oxidative Activation of a ChromophoreCatalyst Assembly on TiO2. *J. Phys. Chem. Lett.* **2011**, 1808–1813.

(111) Wang, L.; Ashford, D. L.; Thompson, D. W.; Meyer, T. J.; Papanikolas, J. M. Watching Photoactivation in a Ru(II) Chromophore-Catalyst Assembly on TiO2 by Ultrafast Spectroscopy. *J. Phys. Chem. C* **2013**, *117* (46), 24250–24258.

(112) Ma, D.; Bettis, S. E.; Hanson, K.; Minakova, M.; Alibabaei, L.; Fondrie, W.; Ryan, D. M.; Papoian, G. a.; Meyer, T. J.; Waters, M. L.; et al. Interfacial Energy Conversion in RuII Polypyridyl-Derivatized Oligoproline Assemblies on TiO2. *J. Am. Chem. Soc.* **2013**, *135* (14), 5250–5253.

(113) Bettis, S. E.; Hanson, K.; Wang, L.; Gish, M. K.; Concepcion, J. J.; Fang, Z.; Meyer, T. J.; Papanikolas, J. M. Photophysical Characterization of a Chromophore/water Oxidation Catalyst Containing a Layer-by-Layer Assembly on Nanocrystalline TiO2 Using Ultrafast Spectroscopy. *J. Phys. Chem. A* **2014**, *118* (45), 10301–10308.

(114) Leem, G.; Morseth, Z. a; Puodziukynaite, E.; Jiang, J.; Fang, Z. Light-Harvesting and Charge Separation in a π -Conjugated Antenna Polymer Bound to TiO2. *J. Phys. Chem. C* **2014**, *118*, 28535–28541.

(115) Ning, Z.; Zhang, Q.; Pei, H.; Luan, J.; Lu, C.; Cui, Y.; Tian, H. Photovoltage Improvement for Dye-Sensitized Solar Cells via Cone-Shaped Structural Design. *J. Phys. Chem. C* **2009**, *113* (23), 10307–10313.

(116) Yum, J. H.; Hagberg, D. P.; Moon, S. J.; Karlsson, K. M.; Marinado, T.; Sun, L.; Hagfeldt, A.; Nazeeruddin, M. K.; Grätzel, M. A Light-Resistant Organic Sensitizer for Solar-Cell Applications. *Angew. Chemie - Int. Ed.* **2009**, *48* (9), 1576–1580.

(117) Dimitrov, S. D.; Durrant, J. R. Materials Design Considerations for Charge Generation in Organic Solar Cells. *Chemistry of Materials*. **2014**, pp 616–630.

(118) Edvinsson, T.; Li, C.; Pschirer, N.; Schöneboom, J.; Eickemeyer, F.; Sens, R.; Boschloo, G.; Herrmann, A.; Müllen, K.; Hagfeldt, A. Intramolecular Charge-Transfer Tuning of Perylenes: Spectroscopic Features and Performance in Dye-Sensitized Solar Cells. *J. Phys. Chem. C* **2007**, *111* (42), 15137–15140.

(119) Wang, Z. S.; Koumura, N.; Cui, Y.; Takahashi, M.; Sekiguchi, H.; Mori, A.; Kubo, T.; Furube, A.; Hara, K. Hexylthiophene-Functionalized Carbazole Dyes for Efficient Molecular Photovoltaics: Tuning of Solar-Cell Performance by Structural Modification. *Chem. Mater.* **2008**, *20* (12), 3993–4003.

(120) Karlsson, M.; Jogi, I.; Eriksson, S. K.; Rensmo, H.; Boman, M.; Boschloo, G.; Hagfeldt, A. Dye-Sensitized Solar Cells Employing a SnO2-TiO2 Core-Shell Structure Made by Atomic Layer Deposition. *Chimia (Aarau).* **2013**, *67*, 142–148.

(121) Alibabaei, L.; Farnum, B. H.; Kalanyan, B.; Brennaman, M. K.; Losego, M. D.; Parsons, G. N.; Meyer, T. J. Atomic Layer Deposition of TiO 2 on Mesoporous nanoITO: Conductive Core − Shell Photoanodes for Dye-Sensitized Solar Cells. *Nano Lett.* **2014**, *14*, 3255–3261.

(122) Chappel, S.; Chen, S. G.; Zaban, A. TiO2-Coated Nanoporous SnO2 Electrodes for Dye-Sensitized Solar Cells. *Langmuir* **2002**, *18* (8), 3336–3342.

(123) Yang, Z.; Gao, S.; Li, T.; Liu, F. Q.; Ren, Y.; Xu, T. Enhanced Electron Extraction from Template-Free 3D Nanoparticulate Transparent Conducting Oxide (TCO) Electrodes for Dye-Sensitized Solar Cells. *ACS Appl. Mater. Interfaces* **2012**, *4* (8), 4419–4427.

(124) Chandiran, A. K.; Yella, A.; Stefik, M.; Heiniger, L.-P.; Comte, P.; Nazeeruddin, M. K.; Grätzel, M. Low-Temperature Crystalline Titanium Dioxide by Atomic Layer Deposition for Dye-Sensitized Solar Cells. *ACS Appl. Mater. Interfaces* **2013**, *5* (8), 3487–3493.

(125) Kim, D. H.; Woodroof, M.; Lee, K.; Parsons, G. N. Atomic Layer Deposition of High Performance Ultrathin TiO2 Blocking Layers for Dye-Sensitized Solar Cells. *ChemSusChem* **2013**, *6* (6), 1014–1020.

(126) Prasittichai, C.; Avila, J. R.; Farha, O. K.; Hupp, J. T. Systematic Modulation of Quantum (electron) Tunneling Behavior by Atomic Layer Deposition on Nanoparticulate SnO2 and TiO2 Photoanodes. *J. Am. Chem. Soc.* **2013**, *135* (44), 16328–16331.

(127) Alibabaei, L.; Farnum, B. H.; Kalanyan, B.; Brennaman, M. K.; Losego, M. D.; Parsons, G. N.; Meyer, T. J. Atomic Layer Deposition of TiO2 on Mesoporous nanoITO: Conductive Core-Shell Photoanodes for Dye-Sensitized Solar Cells. *Nano Lett.* **2014**, *14* (6), 3255–3261.

(128) Li, L.; Pandey, A.; Werder, D. J.; Khanal, B. P.; Pietryga, J. M.; Klimov, V. I. Efficient Synthesis of Highly Luminescent Copper Indium Sulfide-Based Core/shell Nanocrystals with Surprisingly Long-Lived Emission. *J. Am. Chem. Soc.* **2011**, *133* (5), 1176–1179.

(129) Aldana, J.; Wang, Y. a.; Peng, X. Photochemical Instability of CdSe Nanocrystals Coated by Hydrophilic Thiols. *J. Am. Chem. Soc.* **2001**, *123* (36), 8844–8850.

(130) Majetich, S. a.; Carter, A. C.; Belot, J.; McCullough, R. D. 1H NMR Characterization of the CdSe Nanocrystallite Surface. *J. Phys. Chem.* **1994**, *98* (51), 13705–13710.

(131) Hassinen, A.; Moreels, I.; De, M. D. C.; Martins, J. C.; Hens, Z. Nuclear Magnetic Resonance Spectroscopy Demonstrating Dynamic Stabilization of CdSe Quantum Dots by Alkylamines. *J. Phys. Chem. Lett.* **2010**, *1* (Copyright (C) 2013 American Chemical Society (ACS). All Rights Reserved.), 2577–2581.

(132) Gomes, R.; Hassinen, A.; Szczygiel, A.; Zhao, Q.; Vantomme, A.; Martins, J. C.; Hens, Z. Binding of Phosphonic Acids to CdSe Quantum Dots: A Solution NMR Study. *J. Phys. Chem. Lett.* **2011**, *2* (3), 145–152.

(133) Hens, Z.; Martins, J. C. A Solution NMR Toolbox for Characterizing the Surface Chemistry of Colloidal Nanocrystals. *Chem. Mater.* **2013**, *25* (8), 1211–1221.

(134) Fritzinger, B.; Capek, R. K.; Lambert, K.; Martins, J. C.; Hens, Z. Utilizing Self-Exchange to Address the Binding of Carboxylic Acid Ligands to CdSe Quantum Dots. *J. Am. Chem. Soc.* **2010**, *132* (29), 10195–10201.

(135) Donakowski, M. D.; Godbe, J. M.; Sknepnek, R.; Knowles, K. E.; Olvera de la Cruz, M.; Weiss, E. a. A Quantitative Description of the Binding Equilibria of Para-Substituted Aniline Ligands and CdSe Quantum Dots. *J. Phys. Chem. C* **2010**, *114* (51), 22526–22534.

(136) Anderson, N. C.; Hendricks, M. P.; Choi, J. J.; Owen, J. S. Ligand Exchange and the Stoichiometry of Metal Chalcogenide Nanocrystals: Spectroscopic Observation of Facile Metal-Carboxylate Displacement and Binding. *J. Am. Chem. Soc.* **2013**, *135* (49), 18536–18548.

(137) Chambrier, I.; Banerjee, C.; Remiro-buenaman, S.; Chao, Y.; Cammidge, A. N.; Bochmann, M. Synthesis of Porphyrin − CdSe Quantum Dot Assemblies: Controlling Ligand Binding by Substituent E Ff Ects. *Inorg. Chem.* **2015**, *54*, 7368–7380.

(138) Owen, J. S.; Park, J.; Trudeau, P. E.; Alivisatos, a. P. Reaction Chemistry and Ligand Exchange at Cadmium-Selenide Nanocrystal Surfaces. *J. Am. Chem. Soc.* **2008**, *130* (37), 12279–12281.

(139) Ji, X.; Copenhaver, D.; Sichmeller, C.; Peng, X. Ligand Bonding and Dynamics on Colloidal Nanocrystals at Room Temperature: The Case of Alkylamines on CdSe Nanocrystals. *J. Am. Chem. Soc.* **2008**, *130* (17), 5726–5735.

(140) Bullen, C.; Mulvaney, P. The Effects of Chemisorption on the Luminescence of CdSe Quantum Dots. *Langmuir* **2006**, *22* (7), 3007–3013.

(141) Munro, A. M.; Plante, I. J.; Ng, M. S.; Ginger, D. S. Quantitative Study of the Effects of Surface Ligand Concentration on CdSe Nanocrystal Photoluminescence. *J. Phys. Chem.* **2007**, *33*, 6220–6227.

(142) Morris-Cohen, A. J.; Vasilenko, V.; Amin, V. a.; Reuter, M. G.; Weiss, E. a. Model for Adsorption of Ligands to Colloidal Quantum Dots with Concentration-Dependent Surface Structure. *ACS Nano* **2012**, *6* (1), 557–565.

(143) Valdez, C. N.; Schimpf, A. M.; Gamelin, D. R.; Mayer, J. M. Low Capping Group Surface Density on Zinc Oxide Nanocrystals. *ACS Nano* **2014**, No. 9, 9463–9470.

(144) Morris-Cohen, A. J.; Donakowski, M. D.; Knowles, K. E.; Weiss, E. a. The Effect of a Common Purification Procedure on the Chemical Composition of the Surfaces of Cdse Quantum Dots Synthesized with Trioctylphosphine Oxide. *J. Phys. Chem. C* **2010**, *114* (2), 897–906.

(145) Fulmer, G. R.; Miller, A. J. M.; Sherden, N. H.; Gottlieb, H. E.; Nudelman, A.; Stoltz, B. M.; Bercaw, J. E.; Goldberg, K. I. NMR Chemical Shifts of Trace Impurities: Common Laboratory Solvents, Organics, and Gases in Deuterated Solvents Relevant to the Organometallic Chemist. *Organometallics* **2010**, *29* (9), 2176–2179.

(146) Jasieniak, J.; Smith, L.; Embden, J. Van; Mulvaney, P.; Califano, M. Re-Examination of the Size-Dependent Absorption Properties of CdSe Quantum Dots. *J. Phys. Chem. C* **2009**, *113* (45), 19468–19474.

(147) Segall, Y.; Quistad, G. B.; Casida, J. E. Cannabinoid CB1 Receptor Chemical Affinity Probes: Methods Suitable for Preparation of Isopropyl [11,12- 3 H]Dodecylfluorophosphonate and [11,12- 3 H]Dodecanesulfonyl Fluoride. *Synth. Commun.* **2003**, *33* (12), 2151–2159.

(148) Ruiterkamp, G. J.; Hempenius, M. a.; Wormeester, H.; Vancso, G. J. Surface Functionalization of Titanium Dioxide Nanoparticles with Alkanephosphonic Acids for Transparent Nanocomposites. *J. Nanoparticle Res.* **2011**, *13* (7), 2779–2790.

(149) McGovern, M. E.; Thompson, M. Thiol Functionalization of Surfaces for Biosensor Development. *Can. J. Chem. Can. Chim.* **1999**, *77* (10), 1678–1689.

(150) Minozzi, M.; Nanni, D.; Walton, J. C. Alkenylthioimidoyl Radicals: Competition between B-Scission and Cyclization to Dihydrothiophen-2-Ylidene-Amines. *Org. Lett.* **2003**, *5* (6), 901–904.

(151) Goodwin, E. D.; Diroll, B. T.; Oh, S. J.; Paik, T.; Murray, C. B.; Kagan, C. R. E Ff Ects of Post-Synthesis Processing on CdSe Nanocrystals and Their Solids : Correlation between Surface Chemistry and Optoelectronic Properties. **2014**.

(152) Shakeri, B.; Meulenberg, R. W. A Closer Look into the Traditional Purification Process of CdSe Semiconductor Quantum Dots. *Langmuir* **2015**, *31* (49), 13433–13440.

(153) Shen, Y.; Tan, R.; Gee, M. Y.; Greytak, A. B. Quantum Yield Regeneration: Influence of Neutral Ligand Binding on Photophysical Properties in Colloidal Core/Shell Quantum Dots. *ACS Nano* **2015**, *9* (3), 3345–3359.

(154) Hassinen, Antti; Moreels, Iwan; Nolf, Kim De; Smet, Philippe F.; Martins, Jose C.; Hens, Z. Short-Chain Alcohols Strip X-Type Ligands and Quench the Luminescence of PbSe and CdSe Quantum Dots, Acetonitrile Does Not. *J. Am. Chem. Soc.* **2012**, *134*, 20705–20712.

(155) Shen, Y.; Gee, M. Y.; Tan, R.; Pellechia, P. J.; Greytak, A. B. Purification of Quantum Dots by Gel Permeation Chromatography and the Effect of Excess Ligands on Shell Growth and Ligand Exchange. *Chem. Mater.* **2013**, *25* (14), 2838–2848.

(156) Peterson, M. D.; Cass, L. C.; Harris, R. D.; Edme, K.; Sung, K.; Weiss, E. A. The Role of Ligands in Determining the Exciton Relaxation Dynamics in Semiconductor Quantum Dots. *Annu. Rev. Phys. Chem.* **2014**, *65* (1), 317–339.

(157) Busby, E.; Anderson, N. C.; Owen, J. S.; Sfeir, M. Y. Effect of Surface Stoichiometry on Blinking and Hole Trapping Dynamics in CdSe Nanocrystals. *J. Phys. Chem. C* **2015**, *119* (49), 27797–27803.

(158) Lin, W.; Walter, J.; Burger, A.; Maid, H.; Hirsch, A.; Peukert, W.; Segets, D. A General Approach To Study the Thermodynamics of Ligand Adsorption to Colloidal Surfaces Demonstrated by Means of Catechols Binding to Zinc Oxide Quantum Dots. *Chem. Mater.* **2015**, *27* (1), 358–369.

(159) Meek, S. J.; Pitman, C. L.; Miller, A. J. M. Deducing Reaction Mechanism: A Guide for Students, Researchers, and Instructors. *J. Chem. Educ.* **2016**, acs.jchemed.5b00160.

(160) McLaurin, E. J.; Vlaskin, V. a.; Gamelin, D. R. Water-Soluble Dual-Emitting Nanocrystals for Ratiometric Optical Thermometry. *J. Am. Chem. Soc.* **2011**, *133* (38), 14978–14980.

(161) Gary, D. C.; Flowers, S. E.; Kaminsky, W.; Petrone, A.; Li, X.; Cossairt, B. M. Single-Crystal and Electronic Structure of a 1.3 Nm Indium Phosphide Nanocluster. *J. Am. Chem. Soc.* **2016**, jacs.5b13214.

(162) Frederick, M. T.; Amin, V. a; Cass, L. C.; Weiss, E. a. A Molecule to Detect and Perturb the Confinement of Charge Carriers in Quantum Dots. *Nano Lett.* **2011**, *11* (12), 5455–5460.

(163) Dollefeld, H.; Hoppe, K.; Kolny, J.; Schilling, K.; Weller, H.; Eychm??ller, A. Investigations on the Stability of Thiol Stabilized Semiconductor Nanoparticles. *Phys. Chem. Chem. Phys.* **2002**, *4*, 4747–4753.

(164) Berrettini, M. G.; Braun, G.; Hu, J. G.; Strouse, G. F. NMR Analysis of Surfaces and Interfaces in 2 Nm CdSe. *J. Am. Chem. Soc.* **2004**, *126* (22), 7063–7070.

(165) Munro, A. M.; Ginger, D. S. Photoluminescence Quenching of Single CdSe Nanocrystals by Ligand Adsorption. *Nano Lett.* **2008**, *8* (8), 2585–2590.

(166) Katoh, R.; Furube, A.; Yoshihara, T.; Hara, K.; Fujihashi, G.; Takano, S.; Murata, S.; Arakawa, H.; Tachiya, M. Efficiencies of Electron Injection from Excited N3 Dye into Nanocrystalline Semiconductor Films. *J. Phys. Chem. B* **2004**, No. 108, 4818–4822.

(167) Kamat, P. V. Rate Constants for Charge Injection from Excited Sensitizer into SnO2, ZnO, and Ti02 Semiconductor Nanocrystallites. *J. Phys. Chem.* **1995**, *2*, 12902–12906.

(168) Hanson, K.; Brennaman, M. K.; Ito, A.; Luo, H.; Song, W.; Parker, K. A.; Ghosh, R.; Norris, M. R.; Glasson, C. R. K.; Concepcion, J. J.; et al. Structure–Property Relationships in Phosphonate-Derivatized, RuII Polypyridyl Dyes on Metal Oxide Surfaces in an Aqueous Environment. *J. Phys. Chem. C* **2012**, *116* (28), 14837–14847.

(169) Ito, S.; Zakeeruddin, S. M.; Humphry-Baker, R.; Liska, P.; Charvet, R.; Comte, P.; Nazeeruddin, M. K.; Péchy, P.; Takata, M.; Miura, H.; et al. High-Efficiency Organic-Dye- Sensitized Solar Cells Controlled by Nanocrystalline-TiO2 Electrode Thickness. *Adv. Mater.* **2006**, *18* (9), 1202–1205.

(170) Brennaman, M. K.; Patrocinio, A. O. T.; Song, W.; Jurss, J. W.; Concepcion, J. J.; Hoertz, P. G.; Traub, M. C.; Iha, N. Y. M.; Meyer, T. J. Interfacial Electron Transfer Dynamics Following Laser Flash Photolysis of [Ru(bpy)2((4,4'-PO3H2)2bpy)]2+ in TiO2 Nanoparticle Films in Aqueous Environments. *ChemSusChem* **2011**, *4* (2), 216–227.

(171) Jurss, J. W. PhD Thesis, UNC Chapel Hill, 2010.

(172) O'Regan, B.; Gratzel, M.; Fitzmaurice, D. Optical Electrochemistry I : Steady-State Spectroscopy of Conduction-Band Electrons in a Metal Oxide Semiconductor Electrode. *Chem. Phys. Lett.* **1991**, *183* (I), 89–93.

(173) Willis, R. L.; Olson, C.; Regan, B. O.; Lutz, T.; Nelson, J.; Durrant, J. R. Electron Dynamics in Nanocrystalline ZnO and TiO 2 Films Probed by Potential Step Chronoamperometry and Transient Absorption Spectroscopy. *J. Phys. Chem. B* **2002**, *106*, 7605–7613.

(174) Ondersma, J. W.; Hamann, T. W. Conduction Band Energy Determination by Variable Temperature Spectroelectrochemistry. *Energy Environ. Sci.* **2012**, *5* (11), 9476.

(175) Van de Krol, R.; Goossens, A.; Meulenkamp, E. a. Electrical and Optical Properties of TiO[sub 2] in Accumulation and of Lithium Titanate Li[sub 0.5]TiO[sub 2]. *J. Appl. Phys.* **2001**, *90* (5), 2235.

(176) Gillaizeau-Gauthier, I.; Odobel, F.; Alebbi, M.; Argazzi, R.; Costa, E.; Bignozzi, C. a; Qu, P.; Meyer, G. J. Phosphonate-Based Bipyridine Dyes for Stable Photovoltaic Devices. *Inorg. Chem.* **2001**, *40* (23), 6073–6079.

(177) Bergeron, B. V; Marton, A.; Oskam, G.; Meyer, G. J. Dye-Sensitized SnO2 Electrodes with Iodide and Pseudohalide Redox Mediators. *J. Phys. Chem. B* **2005**, *109* (2), 937–943.

(178) Durrant, J. R. Modulating Interfacial Electron Transfer Dynamics in Dye Sensitised Nanocrystalline Metal Oxide Films. *J. Photochem. Photobiol. A Chem.* **2002**, *148* (1-3), 5–10.

(179) Walker, A. B.; Peter, L. M.; Martínez, D.; Lobato, K. Cells, Transient Photocurrents in Dye-Sensitized Nanocrystalline Solar. *Chimia (Aarau).* **2007**, *61* (12), 792–795.

(180) Nelson, J.; Chandler, R. E. Random Walk Models of Charge Transfer and Transport in Dye Sensitized Systems. *Coord. Chem. Rev.* **2004**, *248* (13-14), 1181–1194.

(181) Knorr, F. J.; Mchale, J. L. Spectroelectrochemical Photoluminescence of Trap States of Nanocrystalline TiO 2 in Aqueous Media. *J. Phys. Chem. C* **2013**, *117*, 13654–13662.

(182) Fabregat-santiago, F.; Mora-sero, I.; Bisquert, J. Cyclic Voltammetry Studies of Nanoporous Semiconductors . Capacitive and Reactive Properties of Nanocrystalline TiO 2 Electrodes in Aqueous Electrolyte. *J. Phys. Chem. B* **2003**, *107*, 758–768.

(183) Bisquert, J.; Fabregat-Santiago, F.; Mora-Seró, I.; Garcia-Belmonte, G.; Barea, E. M.; Palomares, E. A Review of Recent Results on Electrochemical Determination of the Density of Electronic States of Nanostructured Metal-Oxide Semiconductors and Organic Hole Conductors. *Inorganica Chim. Acta* **2008**, *361* (3), 684–698.

(184) Jankulovska, M.; Berger, T.; Wong, S. S.; Gómez, R.; Lana-Villarreal, T. Trap States in TiO2 Films Made of Nanowires, Nanotubes or Nanoparticles: An Electrochemical Study. *Chemphyschem* **2012**, *13* (12), 3008–3017.

(185) Hagfeldt, A.; Grätzel, M. Light-Induced Redox Reactions in Nanocrystalline Systems. *Chem. Rev.* **1995**, *95*, 49–68.

(186) Bedja, I.; Hotchandani, S.; Kamat, P. V. Preparation and Photoelectrochemical Characterization of Thin SnO2 Nanocrystalline Semiconductor Films and Their Sensitization with Bis(2,2'-bipyridine)(2,2'-Bipyridine-4,4'-Dicarboxylic acid)ruthenium(II) Complex. *J. Phys. Chem.* **1994**, *98*, 4133–4140.

(187) Ai, X.; Anderson, N. a; Guo, J.; Lian, T. Electron Injection Dynamics of Ru Polypyridyl Complexes on SnO2 Nanocrystalline Thin Films. *J. Phys. Chem. B* **2005**, *109* (15), 7088–7094.

(188) Anderson, N. a; Lian, T. Ultrafast Electron Transfer at the Molecule-Semiconductor Nanoparticle Interface. *Annu. Rev. Phys. Chem.* **2005**, *56* (78), 491–519.

(189) Anderson, S.; Constable, E. C.; Dare-Edwards, M.; Goodenough, J. B.; Hamnett, A.; Seddon, K. R.; Wright, R. D. Chemical Modification of a Titanium (IV) Oxide Electrode to Give Stable Dye Sensitisation Without a Upersensitiser. *Nature* **1979**, *280*, 571–573.

(190) Berger, T.; Monllor-Satoca, D.; Jankulovska, M.; Lana-Villarreal, T.; Gómez, R. The Electrochemistry of Nanostructured Titanium Dioxide Electrodes. *Chemphyschem* **2012**, *13* (12), 2824–2875.

(191) Boschloo, G.; Fitzmaurice, D. Spectroelectrochemical Investigation of Surface States in Nanostructured TiO 2 Electrodes. *J. Phys. Chem. B* **1999**, *103*, 2228–2231.

(192) Wang, H.; He, J.; Boschloo, G.; Lindstro, H.; Hagfeldt, A.; Lindquist, S. Electrochemical Investigation of Traps in a Nanostructured TiO 2 Film. *J. Phys. Chem. B* **2001**, *105*, 2529–2533.

(193) Berger, T.; Anta, J. A.; Morales-flo, V.; Físicos, D. D. S.; Naturales, Q.; Física, A. D. Q.; Olavide, U. P. De; Utrera, C.; Sevilla, E.-. Electrons in the Band Gap : Spectroscopic Characterization of Anatase TiO 2 Nanocrystal Electrodes under Fermi Level Control. *J. Phys. Chem. C* **2012**, *116*, 11444–11455.

(194) Agrell, H. G.; Boschloo, G.; Hagfeldt, A. Conductivity Studies of Nanostructured TiO 2 Films Permeated with Electrolyte. *J. Phys. Chem. B* **2004**, *108*, 12388–12396.

(195) Moser, J. E.; Grätzel, M. Observation of Temperature Independent Heterogeneous Electron Transfer Reactions in the Inverted Marcus Region. *Chem. Phys.* **1993**, *176* (2-3), 493–500.

(196) Huang, Q.; Li, F.; Gong, Y.; Luo, J.; Yang, S.; Luo, Y.; Li, D.; Bai, X.; Meng, Q. Recombination in SnO 2 -Based Quantum Dots Sensitized Solar Cells: The Role of Surface States. *J. Phys. Chem. C* **2013**, *117* (21), 10965–10973.

(197) Jarzebski, Z. M.; Marton, J. P. Physical Properties of SnO2 Materials: II . Electrical Properties. *J. Electrochem. Soc.* **1976**, *123* (299c-310c).

(198) Haque, S. A.; Tachibana, Y.; Willis, R. L.; Moser, J. E.; Gra, M.; Klug, D. R.; Durrant, J. R.; Polytechnique, Ä. Parameters Influencing Charge Recombination Kinetics in Dye-Sensitized Nanocrystalline Titanium Dioxide Films. *J. Phys. Chem. B* **2000**, *104*, 538–547.

(199) Zhang, J. Z. Ultrafast Studies of Electron Dynamics in Semiconductor and Metal Colloidal Nanoparticles: Effects of Size and Surface. *Acc. Chem. Res.* **1997**, *30* (10), 423–429.

(200) Katoh, R.; Furube, A. Tunneling-Type Charge Recombination in Nanocrystalline TiO 2 Films at Low Temperature. *J. Phys. Chem. Lett.* **2011**, *2*, 1888–1891.

(201) Johansson, P. G.; Kopecky, A.; Galoppini, E.; Meyer, G. J. Distance Dependent Electron Transfer at TiO2 Interfaces Sensitized with Phenylene Ethynylene Bridged Ru(II)-Isothiocyanate Compounds. *J. Am. Chem. Soc.* **2013**, *135*, 8331–8341.

(202) Gaal, D. a.; Hupp, J. T. Thermally Activated, Inverted Interfacial Electron Transfer Kinetics: High Driving Force Reactions between Tin Oxide Nanoparticles and Electrostatically-Bound Molecular Reactants. *J. Am. Chem. Soc.* **2000**, *122* (44), 10956–10963.

(203) She, C.; Anderson, N. a; Guo, J.; Liu, F.; Goh, W.-H.; Chen, D.-T.; Mohler, D. L.; Tian, Z.-Q.; Hupp, J. T.; Lian, T. pH-Dependent Electron Transfer from Re-Bipyridyl Complexes to Metal Oxide Nanocrystalline Thin Films. *J. Phys. Chem. B* **2005**, *109* (41), 19345–19355.

(204) Weng, Y.; Wang, Y.; Asbury, J. B.; Ghosh, H. N.; Lian, T. Back Electron Transfer from TiO 2 Nanoparticles to Fe III (CN) 63- : Origin of Non-Single-Exponential and Particle Size Independent Dynamics. *J. Phys. Chem. B* **2000**, *104*, 93–104.

(205) Concepcion, J. J.; House, R. L.; Papanikolas, J. M.; Meyer, T. J. Chemical Approaches to Artificial Photosynthesis. *Proc. Natl. Acad. Sci. U. S. A.* **2012**, *109* (39), 15560–15564.

(206) *The Porphyrin Handbook*; Academic Press: New York, 2000.

(207) Imahori, H.; Hayashi, S.; Hayashi, H.; Oguro, A.; Eu, S.; Umeyama, T.; Matano, Y. Effects of Porphyrin Substituents and Adsorption Conditions on Photovoltaic

Properties of Porphyrin-Sensitized TiO2 Cells. *J. Phys. Chem. C* **2009**, *113*, 18406–18413.

(208) Martinez-Diaz, M. V.; Torrea, G. de la; Torres, T. Lighting Porphyrins and Phthalocyanines for Molecular Photovoltaics. *Chem. Commun.* **2010**, *46*, 7090–7108.

(209) Walter, M. G.; Rudine, A. B.; Wamser, C. C. Porphyrins and Phthalocyanines in Solar Photovoltaic Cells. *J. Porphyrins Phthalocyanines* **2010**, *14*, 759–792.

(210) Martini, L. A.; Moore, G. F.; Milot, R. L.; Cai, L. Z.; Sheehan, S. W.; Schmuttenmaer, C. A.; Brudvig, G. W.; Crabtree, R. H. Modular Assembly of High-Potential Zinc Porphyrin Photosensitizers Attached to TiO2 with a Series of Anchoring Groups. *J. Phys. Chem. C* **2013**, *117*, 14526–14533.

(211) Megiatto, J. D.; Antoniuk-Pablant, A.; Sherman, B. D.; Kodis, G.; Gervaldo, M.; Moore, T. A.; Moore, A. L.; Gust, D. Mimicking the Electron Transfer Chain in Photosystem II with a Molecular Triad Thermodynamically Capable of Water Oxidation. *Proc. Natl. Acad. Sci. U. S. A.* **2012**, *109*, 15578–15583.

(212) Moore, G. F.; Blakemore, J. D.; Milot, R. L.; Hull, J. F.; Song, H. -e.; Cai, L.; Schmuttenmaer, C. A.; Crabtree, R. H.; Brudvig, G. W. A Visible Light Water-Splitting Cell with a Photoanode Formed by Codeposition of a High-Potential Porphyrin and an Iridium Water-Oxidation Catalyst. *Energy Environ. Sci.* **2011**, *4*, 2389–2392.

(213) Moore, G. F.; Konezny, S. J.; Song, H. -e.; Milot, R. L.; Blakemore, J. D.; Lee, M. L.; Batista, V. S.; Schmuttenmaer, C. A.; Crabtree, R. H.; Brudvig, G. W. Bioinspired High-Potential Porphyrin Photoanodes. *J. Phys. Chem. C* **2012**, *116*, 4892−4902.

(214) Sherman, B. D.; Pillai, S.; Kodis, G.; Bergkamp, J.; Mallouk, T. E.; Gust, D.; Moore, T. A.; Moore, A. L. A Porphyrin-Stabilized Iridium Oxide Water Oxidation Catalyst. *Can. J. Chem.* **2011**, *89*, 152–157.

(215) Ishida, T.; Terada, K.; Hasegawa, K.; Kuwahata, H.; Kusama, K.; Sato, R.; Nakano, M.; Naitoh, Y.; Haga, M. Self-Assembled Monolayer and Multilayer Formation Using Redox-Active Ru Complex with Phosphonic Acids on Silicon Oxide Surface. *Appl. Surf. Sci.* **2009**, *255*, 8824–8830.

(216) Terada, K.; Kobayashi, K.; Hikita, J.; Haga, M. Electric Conduction Properties of Self-Assembled Monolayer Films of Ru Complexes with Disulfide/Phosphonate Anchors in a Au–(Molecular Ensemble)–(Au Nanoparticle) Junction. *Chem. Lett.* **2009**, *38*, 416–417.

(217) Hanson, K.; Torelli, D. A.; Vannucci, A. K.; Brennaman, M. K.; Luo, H. L.; Alibabaei, L.; Song, W. J.; Ashford, D. L.; Norris, M. R.; Glasson, C. R. K.; et al. Self-Assembled Bilayer Films of Ruthenium(II)/Polypyridyl Complexes through

Layer-by-Layer Deposition on Nanostructured Metal Oxides. *Angew. Chem. Int. Ed.* **2012**, *51*, 12782–12785.

(218) Concepcion, J. J.; Jurss, J. W.; Norris, M. R.; Chen, Z.; Templeton, J. L.; Meyer, T. J. Catalytic Water Oxidation by Single-Site Ruthenium Catalysts. *Inorg. Chem.* **2010**, *49* (4), 1277–1279.

(219) Lapides, A. M.; Ashford, D. L.; Hanson, K.; Torelli, D. A.; Templeton, J. L.; Meyer, T. J. Stabilization of a Ruthenium(II) Polypyridyl Dye on Nanocrystalline TiO2 by an Electropolymerized Overlayer. *J. Am. Chem. Soc.* **2013**, *135*, 15450–15458.

(220) Kavan, L.; Tétreault, N.; Moehl, T.; Grätzel, M. Electrochemical Characterization of TiO2 Blocking Layers for Dye-Sensitized Solar Cells. *J. Phys. Chem. C* **2014**, *118* (30), 16408–16418.

(221) Grätzel, M. Photoelectrochemical Cells. *Nature* **2001**, *414*, 338–344.

(222) Knauf, R. R.; Brennaman, M. K.; Alibabaei, L.; Norris, M. R.; Dempsey, J. L. Revealing the Relationship between Semiconductor Electronic Structure and Electron Transfer Dynamics at Metal Oxide-Chromophore Interfaces. *J. Phys. Chem. C* **2013**, *117* (48), 25259–25268.

(223) Concepcion, J. J.; Jurss, J. W.; Norris, M. R.; Chen, Z.; Templeton, J. L.; Meyer, T. J. Catalytic Water Oxidation by Single-Site Ruthenium Catalysts. *Inorg. Chem.* **2010**, *49*, 1277–1279.

(224) Assembly, C. R.; Norris, M. R.; Concepcion, J. J.; Fang, Z.; Templeton, J. L.; Meyer, T. J. Low-Overpotential Water Oxidation by a Surface-Bound Ruthenium-. *Angew. Chem. Int. Ed. Engl.* **2013**, *52* (51), 13580–13583.

(225) McConnell, H. M. Intramolecular Charge Transfer in Aromatic Free Radicals. *J. Chem. Phys.* **1961**, *35* (2), 508–515.

(226) Gray, H. B.; Winkler, J. R. Long-Range Electron Transfer. *Proc. Natl. Acad. Sci. U. S. A.* **2005**, *102* (10), 3534–3539.

(227) McClure, C. D.; Oldham, C. J.; Walls, H. J.; Parsons, G. N. Large Effect of Titanium Precursor on Surface Reactivity and Mechanical Strength of Electrospun Nanofibers Coated with TiO2 by Atomic Layer Deposition. *J. Vac. Sci. Technol. A* **2013**, *31* (6), 061506.

(228) Dandley, E. C.; Needham, C. D.; Williams, P. S.; Brozena, A. H.; Oldham, C. J.; Parsons, G. N. Temperature-Dependent Reaction between Trimethylaluminum and Poly(methyl Methacrylate) during Sequential Vapor Infiltration: Experimental and Ab Initio Analysis. *J. Mater. Chem. C* **2014**, *2* (44), 9416–9424.

(229) Lee, W.-J. Space-Limited Crystal Growth Mechanism of TiO2 Films by Atomic Layer Deposition. *J. Phys. Chem. C* **2010**, *114*, 6917–6921.

(230) Aarik, J.; Aidla, A.; Uustare, T.; Sammelselg, V. Morphology and Structure of TiO2 Thin Films Grown by Atomic Layer Deposition. *Journal of Crystal Growth*. 1995, pp 268–275.

(231) Liu, Y.; Zheng, C.; Wang, W.; Yin, C.; Wang, G. Synthesis and Characterization of Rutile SnO2 Nanorods. *Adv. Mater.* **2001**, *13* (24), 1883–1887.

(232) Cheng, H.-M.; Hsieh, W.-F. High-Efficiency Metal-Free Organic-Dye-Sensitized Solar Cells with Hierarchical ZnO Photoelectrode. *Energy Environ. Sci.* **2010**, *3* (4), 442.

(233) Nelson, J.; Haque, S.; Klug, D.; Durrant, J. Trap-Limited Recombination in Dye-Sensitized Nanocrystalline Metal Oxide Electrodes. *Phys. Rev. B* **2001**, *63* (20), 205321.

(234) Miettunen, K.; Halme, J.; Vahermaa, P.; Saukkonen, T.; Toivola, M.; Lund, P. Dye Solar Cells on ITO-PET Substrate with TiO[sub 2] Recombination Blocking Layers. *J. Electrochem. Soc.* **2009**, *156* (8), B876.

(235) Wenger, O. S. Photoinduced Electron and Energy Transfer in Phenylene Oligomers. *Chem. Soc. Rev.* **2011**, *40*, 3538–3550.

(236) Closs, G. L.; Miller, J. R. Intramolecular Long-Distance Electron Transfer in Organic Molecules. *Science* **1988**, *240*, 440–447.

(237) Prasai, B.; Cai, B.; Underwood, M. K.; Lewis, J. P.; Drabold, D. a. Properties of Amorphous and Crystalline Titanium Dioxide from First Principles. *J. Mater. Sci.* **2012**, *47* (21), 7515–7521.

(238) Chu, C.; Na, J. S.; Parsons, G. N. Conductivity in Alkylamine/gold and Alkanethiol/gold Molecular Junctions Measured in Molecule/nanoparticle/molecule Bridges and Conducting Probe Structures. *J. Am. Chem. Soc.* **2007**, *129* (8), 2287–2296.

(239) Selzer, Y.; Salomon, A.; Cahen, D. The Importance of Chemical Bonding to the Contact for Tunneling through Alkyl Chains. *J. Phys. Chem. B* **2002**, *106* (40), 10432–10439.

(240) Engelkes, V. B.; Beebe, J. M.; Frisbie, C. D. Length-Dependent Transport in Molecular Junctions Based on SAMs of Alkanethiols and Alkanedithiols: Effect of Metal Work Function and Applied Bias on Tunneling Efficiency and Contact Resistance. *J. Am. Chem. Soc.* **2004**, *126* (43), 14287–14296.